Photoluminescence Properties of Nanocrystals

Guest Editors: L. S. Cavalcante, J. C. Sczancoski, J. A. Varela, E. Longo, J. Andrés, and S. K. Rout

Editorial

Photoluminescence Properties of Nanocrystals

L. S. Cavalcante,[1, 2] J. C. Sczancoski,[2] J. A. Varela,[3] E. Longo,[3] J. Andrés,[3] and S. K. Rout[4]

[1] *Departamento de Química, Universidade Federal de São Carlos, P.O. Box 676, 13565-905 São Carlos, SP, Brazil*

[2] *LIEC-IQ, Universidade Estadual Paulista, P.O. Box 355, 14801-907 Araraquara, SP, Brazil*

[3] *Departamento de Química Física y Analítica, Universitat Jaume I, 12071 Castello, Spain*

[4] *Department of Applied Physics, Birla Institute of Technology, Mesra, Ranchi 835215, India*

Correspondence should be addressed to L. S. Cavalcante, laeciosc@bol.com.br

Photoluminescence (PL) is an optical phenomenon exhibited by some semiconductor materials when excited by an electromagnetic radiation source. After the excitation and recombination processes, these kinds of materials are able to emit photons with less energy than those employed during the electronic excitation. Initially, the researches on the PL properties focused on crystalline materials under cryogenic conditions. However, from the technological viewpoint, the discovery of new materials with visible PL emissions at room temperature has become more interesting for the improvement or development of electrooptic devices. Currently, functional and practical applications of this physical phenomenon in our daily life can be found in light-emitting diodes, lasers, lamps, sensors, scintillators, electronic displays, and so on. In this special issue, the reader will find 10 selected papers briefly summarized below.

PL properties of silicon (Si) nanocrystals (NCs) were reported by S. Kim et al. These authors studied the continuous-wave/time-resolved PL, cathodoluminescence, and electroluminescence of silicon Si NCs produced by ion beam sputtering deposition of SiOx single layer or SiOx/SiO$_2$ multilayers and subsequent annealing.

L. F. da Silva et al. investigated the difference of the PL properties in SrTiO$_3$ micro- and nanocrystals prepared by microwave-assisted hydrothermal method, using two different titanium precursors. In addition, the SrTiO$_3$ nanocrystals were characterized by means of X-ray diffraction, field emission scanning electron microscopy, high-resolution transmission electron microscopy, and X-ray absorption near edge structure spectroscopy.

The concentration effect of polyvinylpyrrolidone (PVP) as polymer surfactant on the PL properties of pure and Ni-doped zinc sulfide (ZnS) nanocrystalline thin films as explained by T. M. Thi et al. These authors investigated the PL excitation, time-resolved PL spectra, and PL decay time of these thin films, which were synthesized by the wet chemical method and spincoating.

H. W. Park and D.-H. Kim verified the effect of different solvents (water, hexane, and toluene) on the surface passivation of CdSe NCs in order to improve its visible luminescence. The results found in this research indicated that the water molecules promote an enhanced ligand passivation on the CdSe NCs and lead to a high PL emission with quantum yield ($\approx 85\%$) of these core CdSe quantum dots.

The PL properties of doped-N,S and Mg and pure ZnO nanocrystalline thin films prepared by the radio frequency magnetron sputtering method were reported by H. Che et al. In this work, these authors studied several factors (structural defects, dopants, and intermediary levels) that act on the optical properties of transparent ZnO thin films. Moreover, there was a relation of PL properties with the presence of deep excitonic energy level in the direct band gaps of these films.

S. Wu et al. reported the effect of different ratio solvents (water/ethanol), use of tetraethylenepentamine as a new chelating ligand, rare earth (Yb^{3+}/Er^{3+}) concentration and reaction time on the morphology and improvement of the PL properties of NaYF$_4$ nanoparticles synthesized by the hydrothermal method.

Two interesting papers on zinc oxide (ZnO) nanostructures were presented by J. Z. Marinho et al. and S. L. Wang et al. In the first one, irregular ZnO microcrystals and spheres-like ZnO nanocrystals were prepared by the conventional water bath heating and microwave-assisted hydrothermal method, respectively. The effect of a different synthesis method using urea as partial reactant with the (C–NH$_2$) groups promoted the formation of ZnO crystals with different structural defects. This factor acted directly on the PL behavior of ZnO micro- and nanocrystals. In the second one, the authors prepared propeller-like ZnO nanostructures by the chemical vapor deposition method and investigated its PL and photocatalytic properties. The results obtained in this work indicated that the propeller-like ZnO nanostructures have superior PL emission in the ultraviolet (UV) region when compared to the flower-shaped ZnO nanostructures prepared by the same method. Moreover, after 3 h of UV-light illumination, the propeller-like nanostructures showed a higher photocatalytic activity for the degradation of rhodamine B.

S.-Y. Ting et al. explained the improvement in the PL properties of ZnO nanocrystalline thin films, employing different buffer layers on sapphire substrates. In this work, these authors described that the effect of different GaN and MgO buffer layers promotes modifications in the local structure, formation of pores on the film surface, and appearance of deep levels at 550 nm in the PL emission spectra.

Finally, T. D. Hoanh et al. synthesized a new light-emissive material, called bis(3H-1,2,3-triazolo-[4,5-b]pyridine-3-ol)zinc (Zn(TAP)$_2$), by the chemical method. This new complex has excellent PL and electroluminescent properties, that is, interesting blue light emission and high luminance of 2,800 cd/m^2 at 12 V. The obtained results in this work by the electrical measurements suggest that this complex can be a good candidate for the development of organic light emitting diodes.

As guest editors for this special issue, we are pleased with diverse and intense research activities in this area. We expect the special issue will be wellreceived by the reader as a small sample of the current research on the PL properties of nanocrystals and nanocrystalline thin films.

Acknowledgments

L. S. Cavalcante
J. C. Sczancoski
J. A. Varela
E. Longo
J. Andrés
S. K. Rout

Research Article

The Effect of Polyvinylpyrrolidone on the Optical Properties of the Ni-Doped ZnS Nanocrystalline Thin Films Synthesized by Chemical Method

Tran Minh Thi,[1] **Le Van Tinh,**[1] **Bui Hong Van,**[2] **Pham Van Ben,**[2] **and Vu Quoc Trung**[3]

[1] *Faculty of Physics, Hanoi National University of Education, 136 Xuan Thuy Road, Cau Giay District, Hanoi, Vietnam*
[2] *Faculty of Physics, College of Science, Hanoi National University, 334 Nguyen Trai Road, Thanh Xuan District, Hanoi, Vietnam*
[3] *Faculty of Chemistry, Hanoi National University of Education, 136 Xuan Thuy Road, Cau Giay District, Hanoi, Vietnam*

Correspondence should be addressed to Tran Minh Thi, tranminhthi@hnue.edu.vn

We report the optical properties of polyvinyl-pyrrolidone (PVP) and the influence of PVP concentration on the photoluminescence spectra of the PVP (PL) coated ZnS : Ni nanocrystalline thin films synthesized by the wet chemical method and spin-coating. PL spectra of samples were clearly showed that the 520 nm luminescence peak position of samples remains unchanged, but their peak intensity changes with PVP concentration. The PVP polymer is emissive with peak maximum at 394 nm with the exciting wavelength of 325 nm. The photoluminescence exciting (PLE) spectrum of PVP recorded at 394 nm emission shows peak maximum at 332 nm. This excitation band is attributed to the electronic transitions in PVP molecular orbitals. The absorption edges of the PVP-coated ZnS : Ni0.3% samples that were shifted towards shorter wavelength with increasing of PVP concentration can be explained by the absorption of PVP in range of 350 nm to 400 nm. While the PVP coating does not affect the microstructure of ZnS : Ni nanomaterial, the analyzed results of the PL, PLE, and time-resolved PL spectra and luminescence decay curves of the PVP and PVP-coated ZnS : Ni samples allow to explain the energy transition process from surface PVP molecules to the Ni^{2+} centers that occurs via hot ZnS.

1. Introduction

Despite intensive research on conductivity, local domain orientation, and molecular order in organic semiconductor thin films [1], the relationship between morphology, chain structure and conductivity of the polymer is still poorly understood. Recently, researchers all over the world have worked on the improvement of electrical conductivity investigated the charge transport and the energy band of a variety of polymers (polyazomethine, aliphatic-aromatic copolyimides). All determined parameters of the electrical conductivity and the energy band have been found to be related to the influence of the polymer chain structure [2–4].

During the last few years there have been extensive experimental and theoretical studies of luminescence, nonlinear optical and electrical properties of a variety of polymers (novel conducting copolymer based on dithienylpyrrole, azobenzene, and EDOT units) in the direction of material science as electronic devices and displays [2, 3, 5–8]. New progress has been made in the area of thermoelectric (TE) applications of conducting polymers and related organic-inorganic composites [9, 10]. Other research efforts aimed to identify the role of additives in optimizing the morphology of organic solar cells and discussed the role of bimolecular recombination in limiting the efficiency of solar cells based on a small optical gap polymer [11, 12].

Recently, methods have been developed to cap the surfaces of the nanoparticles with organic or inorganic groups so that the nanoparticles are stable against agglomeration. Among the inorganic semiconductor nanoparticles, zinc sulfide ZnS is an important II-VI semiconductor, which has been studied extensively because of its broad spectrum of

potential applications, such as in catalysis and electronic and optoelectronic nanodevices. Furthermore, luminescent properties of ZnS can be controlled using various dopants such as Ni, Fe, Mn, and Cu [13–19]. They not only give luminescence in various spectral regions but also enhance the excellent properties of ZnS. In order to cap the ZnS nanoparticles, some particular passivators of ZnS have been used, such as polyvinyl alcohol (PVA) [20] and polyvinyl-pyrrolidone (PVP) [21–25]. Understanding the effect of capping on nanoparticles is one of the most important topics nowadays. The influence of surface passivation on luminescence quantum efficiency of $ZnS:Mn^{2+}$ and $ZnS:Cu^{2+}$ nanoparticles has been discussed when using sodium hexametaphosphate (SHMP), PVP and PVA as coating agents [26–28]. However, till now, there are only a few papers focused on investigation of the optical properties of PVP-coated ZnS nanocomposite materials and the process of energy transfer from organic surface adsorbate of PVP to the dopant ions (Cu^{2+}, Mn^{2+}). Furthermore, there are not any papers completely investigating the optical properties of PVP-coated $ZnS:Ni$ nanocomposite materials.

Thus, in this paper we report the optical properties of PVP (polyvinyl-pyrrolidone) and the influence of PVP concentration on the PL spectra of the PVP-coated $ZnS:Ni$ nanocrystalline thin films synthesized by the wet chemical method and spin-coating. Further, the influences of PVP concentration on the general features of the PL spectra and the process of energy transfer from the PVP to the Ni^{2+} luminescent centers in doped ZnS as well as the optical band gap variation are also discussed.

2. Experiments

2.1. Preparation of ZnS:Ni Nanopowders. The polymer polyvinyl-pyrrolidone and initial chemical substances with high purity (99.9%) (Merck chemicals) were prepared as follows:

   Solution I: 0.1 M $Zn(CH_3COO)_2$ in water,
   Solution II: 0.1 M $NiSO_4$ in water,
   Solution III: 0.1 M Na_2S in water,
   Solution IV: $CH_3OH:H_2O$ (1:1).

Firstly, ZnS:Ni nanoparticles were synthesized by the wet chemical method. Solutions I, II, and III were mixed at an optimal pH = 4.5 and in an appropriate ratio in order to create Ni-doped ZnS powder materials with different molar ratios of Ni^{2+} and Zn^{2+} as follows: 0.0%, 0.2%, 0.3%, 0.6%, and 1%. The precipitated ZnS nad NiS nanoparticles were formed by stirring of the mixed solutions at 80°C for 30 minutes following the chemical reactions

$$Zn(CH_3COO)_2 + Na_2S \longrightarrow ZnS + 2CH_3COONa$$
$$NiSO_4 + Na_2S \longrightarrow NiS + Na_2SO_4 \tag{1}$$
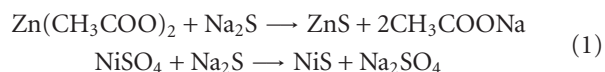
These precipitated ZnS and NiS nanoparticles were filtered by filtering system and then washed in distilled water and ethanol several times. Finally, they were dried under nitrogen gas for 6 h at 60°C. These powder samples were named ZnS, ZnS:Ni0.2%, ZnS:Ni0.3%, ZnS:Ni0.6%, and ZnS:Ni1%, corresponding to different molar ratios of 0.0%, 0.2%, 0.3%, 0.6%, and 1% of Ni^{2+} and Zn^{2+}.

2.2. Preparation of Thin Films and Powders from PVP-Capped ZnS:Ni Nanocrystals. In order to study the role and the effect of PVP on the optical properties of ZnS:Ni, the PVP coated ZnS:Ni nanoparticles were synthesized by keeping a constant nominal Ni concentration of 0.3%, but variation of polymer concentrations.

2.2.1. Preparation of Thin Films from PVP Capped ZnS:Ni Nanocrystals. After washing, 0.1 g formed ZnS:Ni0.3% precipitates were dispersed into 10 mL of $CH_3OH:H_2O$ (1:1) solvent. This mixture was called solution IV. Similarly, 0.1 g of PVP was dissolved in 10 mL of $CH_3OH:H_2O$ (1:1) solvent and was called solution V. After that these two solutions IV and V were mixed with each other at various volume ratios of (5:0), (5:1), (5:2), (5:3), (5:4), and (5:7) under continuous stirring for 1 h at speed of 3000 rpm.

The thin films M-PVP(5:0), M-PVP(5:1), M-PVP(5:2), M-PVP(5:3), and M-PVP(5:4) were produced by the spin-coating method on glass substrate using the rotation speed of 1500 rpm with the same drop-by-drop method and dried at 60°C for all samples.

2.2.2. Preparation of Powders from PVP-Capped ZnS:Ni Nanocrystals. In order to receive the PVP coated ZnS:Ni0.3% nanopowders with different PVP concentrations, the mixed solutions of IV and V were centrifuged at speed 3000 rpm. Then, the received PVP-coated ZnS:Ni0.3% nanoparticles were dried at 80°C. These PVP coated ZnS:Ni0.3% nanopowders are named B(5:0), B(5:1), B(5:2), B(5:3), B(5:4) and B(5:7).

2.3. Research Methods. The microstructure of these samples was investigated by X-ray diffraction (XRD) using XD8 Advance Bruker Diffractometer with CuK_α radiation of $\lambda = 1.5406$ Å and high-resolution transmission electron microscope (HR-TEM). Photoluminescence (PL) spectra, photoluminescence exciting (PLE) spectra, and the absorption spectra of these samples at room temperature were recorded by Fluorolog FL3-22, HP340-LP370 Fluorescence Spectrophotometer with an excitation wavelength of 325 nm, 337 nm, xenon lamp XFOR-450, and JASCO-V670 spectrophotometer, respectively. The time-resoled PL spectra of samples were measured by GDM-100 spectrophotometer using Boxca technique.

3. Results and Discussion

3.1. Analysis of Microstructure by XRD Patterns, Atomic Absorption Spectroscopy, and TEM. Figure 1 shows X-ray diffraction spectra of the pure ZnS nanopowders (inset), ZnS:Ni0.3% with different PVP concentration, B(5:0), B(5:1), B(5:4), corresponding to curves a, b, and c. The analyzed results show that all samples have a sphalerite structure. The three diffraction peaks of $2\theta = 28.8°$, $48.1°$, and $56.5°$ with strong intensity correspond to the (111), (220), and (311) planes. It is shown that the PVP polymer does not affect the microstructure of ZnS:Ni nanomaterials. Thus, one can point out that the PVP coating on the surface
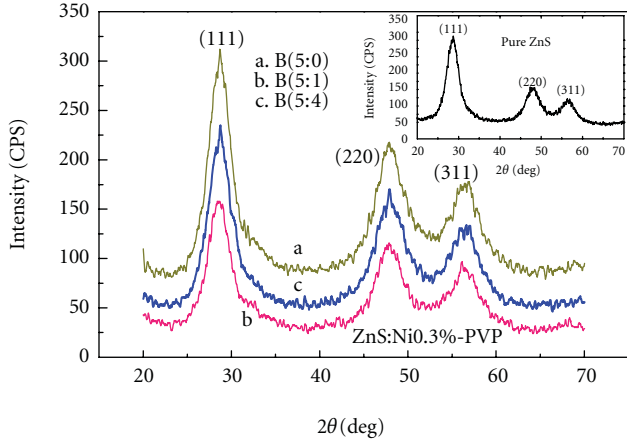
FIGURE 1: The X-ray diffraction spectra of samples B(5:0); B(5:1); B(5:4)—curves a, b, c, and respectively—and pure ZnS nanopowders (inset).

TABLE 1: The band gap of PVP, B(5:0), B(5:1), B(5:2), B(5:3), B(5:4), and B(5:7) samples with different PVP concentrations.

No.	Sample	E_g (eV)	Grain size (nm)
1	B(5:0)	3.11	2,4
2	B(5:1)	3.19	2,4
3	B(5:2)	3.24	
4	B(5:3)	3.28	
5	B(5:4)	3.29	2,5
6	B(5:7)	3.43	
7	PVP	4.19	

of ZnS : Ni nanoparticles possesses the same structure as the amorphous shells (in Figure 2(a)). From the diffraction peaks of 2θ and the standard Bragg relation, the interplanar distance d = 3.12 Å and then the lattice constant a = 5.4 Å for the cubic phase were calculated by the following equations:

$$2d \sin \theta = n\lambda, \quad \frac{1}{d^2} = \frac{h^2 + k^2 + l^2}{a^2}, \quad (2)$$

where d is the interplanar distance and h, k, and l denote the lattice planes.

The average size of the Ni-doped ZnS grains is about 2-3 nm, was calculated by which the Scherrer formula (in Table 1).

Figure 2(b) gives the molecular structure and formula of polyvinyl-pyrrolidone (PVP) with both N and C=O groups. In PVP, nitrogen is conjugated with adjacent carbonyl groups. Thus, the role of PVP consists of (a) forming passivating layers around the ZnS : Ni core due to coordination bond formation between the nitrogen atom of PVP and Zn^{2+} and (b) preventing agglomeration of the particles by the repulsive force acting among the polyvinyl groups [23].

Figure 3(a) presents the HR-TEM image of B(5:3) sample. Figure 3(b) demonstrates the distributions of the adjacent interplanar distances of (111) planes corresponding

to Figure 3(a) (inset). From Figure 3(b) the adjacent interplanar distance of (111) planes is about 3.13 Å. This result is suitable for the XRD patterns and proves that the crystalline is obtained in the as-synthesized samples ZnS : Ni-PVP.

3.2. Photoluminescence Spectra Measurements. Figure 4 shows the photoluminescence PL spectra with the exciting wavelength of 325 nm of the ZnS : Ni0.2%, ZnS : Ni0.3% ZnS : Ni0.6%, ZnS : Ni1.0%, and ZnS powder samples, corresponding to curves a, b, c, d, and e. The peak maximum of ZnS is about 450 nm, meanwhile the PL spectra of ZnS : Ni0.2%, ZnS : Ni0.3% ZnS : Ni0.6%, and ZnS : Ni1.0% samples show peak maximum at 520 nm. In order to study the influence of Ni concentration on photoluminescence of samples, all measured parameters (such as temperature, sample volume, and exciting wavelength intensity) were kept constant for every measurement of samples. This clearly shows that the luminescence peak maximum positions of ZnS : Ni samples are unchanged, but their intensities change rather strongly with increasing of PVP concentration. One of these samples with the large luminescence intensity is ZnS : Ni0.3% sample. The relative luminescence intensity of this sample is also about double of that of the pure ZnS sample. In comparison with other results, this result also agrees with previous works [13, 15], in which the samples were synthesized from initial chemicals: $Zn(CH_3COO)_2 \cdot 2H_2O$, $NiSO_4$, and TAA (C_2H_5NS). The blue emission band of pure ZnS sample is attributable to the intrinsic emission of defects, vacancy, and an incorporation of trapped electron by defects at donor level under conduction range when the dopant-Ni was added into the hot ZnS semiconductor. Moreover, due to the energy levels of $Ni^{2+}(d^8)$ in ZnS semiconductor materials, the lowest multiplex term ^3F of the free Ni^{2+} ion is split into $^3T_1$, $^3T_2$, and $^3A_2$ through the anisotropic hybridization [13, 15]. Thus, the green luminescence of about 520 nm is attributed to the d-d optical transitions of Ni^{2+}, and the luminescent center of Ni^{2+} is formed in ZnS.

In order to observe the influence of PVP concentration on optical properties of samples, the M-PVP(5:0), M-PVP(5:1), M-PVP(5:2), M-PVP(5:3), and M-PVP(5:4) thin films were measured by the photoluminescence PL spectra using the exciting wavelength of 325 nm (in Figure 5). It is clearly shown that these luminescence peak positions of samples remain unchanged but their peak intensities increase with increasing of PVP concentration from (5:0) to (5:4).

These results show that PVP does not affect the microstructure of ZnS : Ni but plays an important role to improve the optical properties of ZnS : Ni nanoparticles.

3.3. Absorption Spectra and Photoluminescence Excitation (PLE) Spectra. The absorption spectra of PVP sample and the B(5:0), B(5:1), B(5:2), B(5:3), B(5:4), and B(5:7) samples (PVP-coated ZnS : Ni0.3% samples with different PVP concentrations) are shown in Figure 6.

It is known that the light transition through the environment can be demonstrated by the Beer-Lambert law:

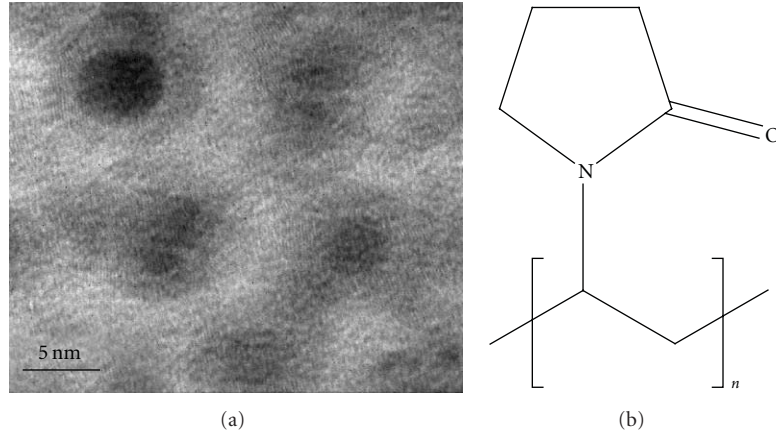$$I(\nu) = I_0(\nu) \cdot e^{-\alpha(\nu)d}, \quad (3)$$

(a)

(b)

FIGURE 2: (a) HR-TEM image of B(5:3) sample. (b) The structure and formula of polyvinyl-pyrrolidone $(C_6H_9NO)_n$.
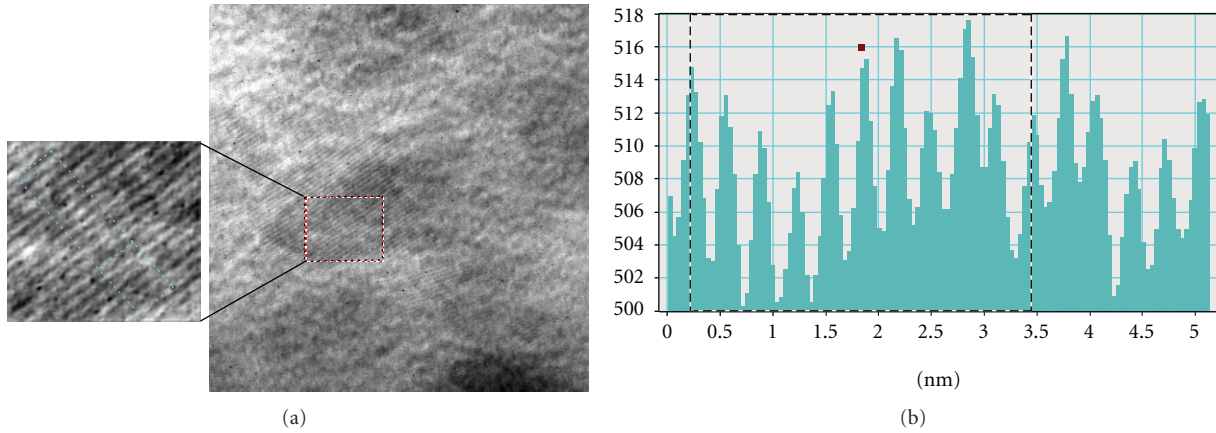

(a)

(nm)

(b)

FIGURE 3: (a) HR-TEM image of B(5:3) sample. (b) The interplanar distances of (111) planes.

where $I_0(\nu)$ and $I(\nu)$ are intensities of light in front of and behind the environment, $\alpha(\nu)$ is absorption coefficient of this environment relative to photon with energy $h\nu$, and d is the thickness of the film.

Formula (3) can be rewritten in logarithmic form:

$$\alpha(\nu) \cdot d = \ln \frac{I_0(\nu)}{I(\nu)} = \ln 10 \cdot \lg \frac{I_0(\nu)}{I(\nu)} = 2.3 \cdot A \quad \text{or} \quad \alpha = \frac{2.3A}{d}, \tag{4}$$

with $A = \lg(I_0(\nu)/I(\nu))$ being the absorption.

The relation between absorption coefficient α and energy of photon was represented by the following equation [22]:

$$\alpha = \frac{K(h\nu - E_g)^{n/2}}{h\nu}, \tag{5}$$

where K is a constant, E_g is the band gap of material, the exponent n is dependent on the type of transition (here, $n = 1$ for the direct transition of ZnS:Ni semiconductor).

From (4) and (5), it can be written as

$$(Ah\nu)^2 = B(h\nu - E_g), \quad \text{where } B \text{ is constant.} \tag{6}$$

By (6), the absorption spectra of samples are converted into the plots of $(Ah\nu)^2$ versus $h\nu$ (Figure 6 inset). The values of the band gap E_g were determined by extrapolating the straight line portion of the $(Ah\nu)^2$ versus $h\nu$ graphs to the $h\nu$-axis (Figure 6 inset). Table 1 gives the band gap values of PVP and the B(5:0), B(5:1), B(5:2), B(5:3), B(5:4), and B(5:7) samples, calculated from these absorption spectra. It is clear that the band gap of the B(5:0) sample (ZnS:Ni0.3% sample) is smaller in comparison with that of pure ZnS (3.68 eV). This decreasing is possibly attributed to the band-edge tail constitution of state density in band gap, by the s-d exchange interaction between $3d^8$ electrons of Ni^{2+} and s conduction electrons in ZnS crystal [29, 30]. On the contrary to this issue of ZnS:Ni (in comparison with that of pure ZnS), the band gap of the PVP-coated ZnS:Ni samples increases from 3.11 eV to 3.43 eV with the increasing of PVP concentration (the absorption spectra shifted toward shorter wavelength).

Because ZnS:Ni nanoparticles were formed in preparation process before they dispersed into PVP matrix, therefore, PVP do not effect to size of nanoparticles. However, the PVP play an important role as the protective layer, against agglomeration ZnS:Ni nanoparticles and contribute to
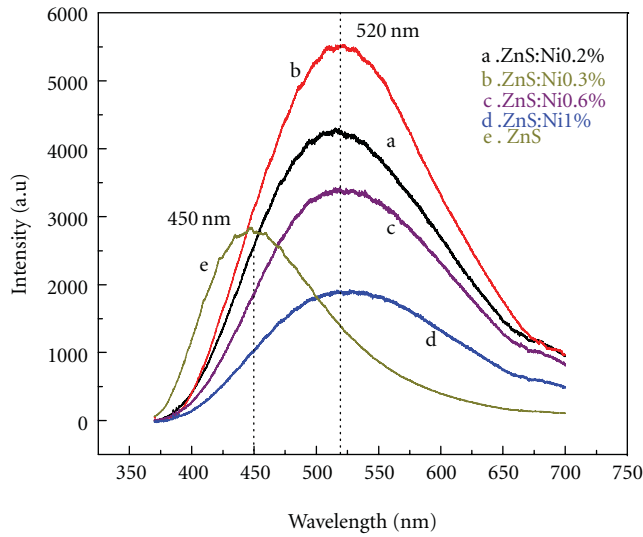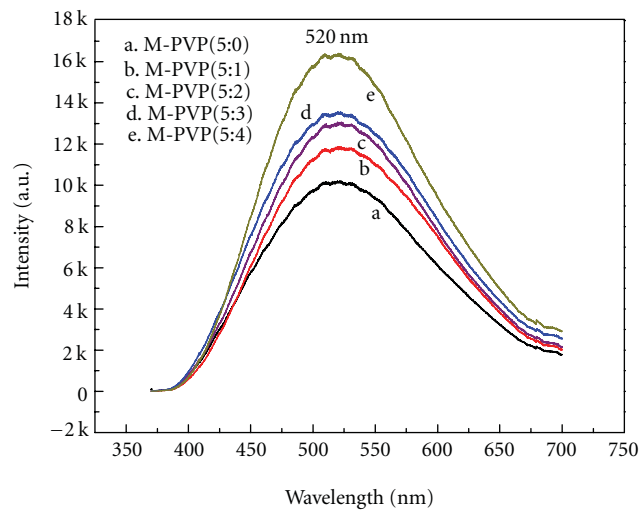
Figure 4: PL spectra of powder samples.
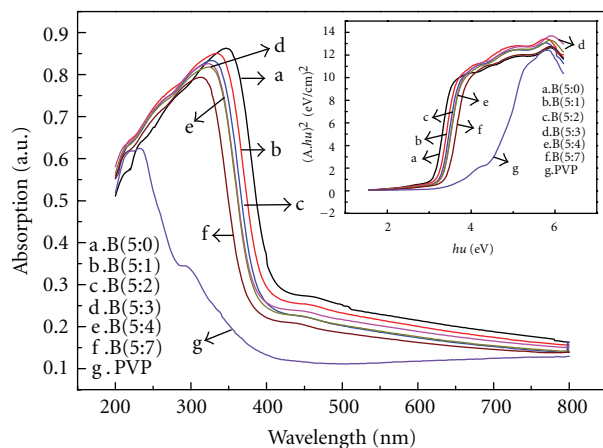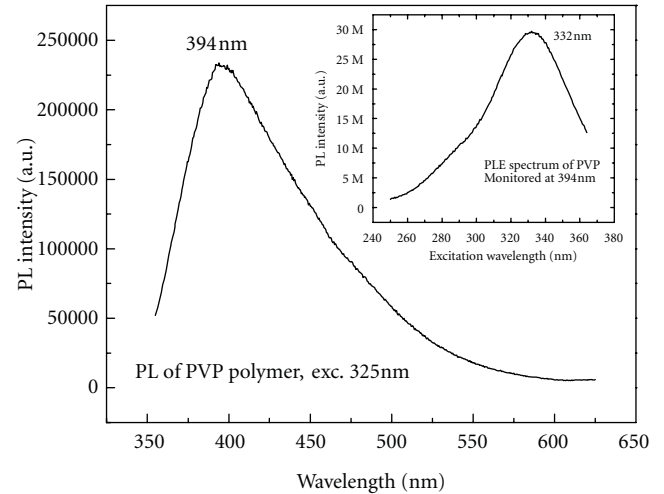

Figure 5: PL spectra of thin films.

Figure 6: The absorption spectra of PVP, B(5 : 0), B(5 : 1), B(5 : 2), B(5 : 3), B(5 : 4), and B(5 : 7) samples. The plots of $(Ah\nu)^2$ versus $h\nu$ (inset).

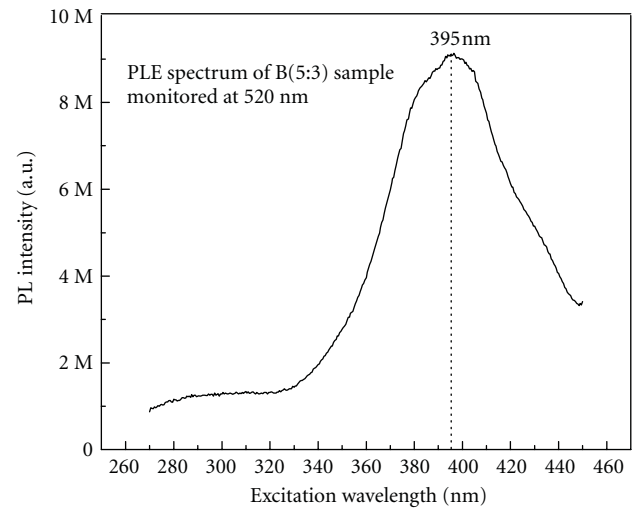Figure 7: PL spectra and PL excitation (PLE) spectra of PVP (inset).

Figure 8: The PLE band of B(5 : 3) monitored at 520 nm.

increase optical properties of ZnS : Ni nanoparticles. The absorption edge and right shoulder of PVP in the range from 230 nm to 400 nm and the absorption edges and right shoulders of PVP-coated ZnS : Ni0.3% samples in range from 350 nm to 400 nm showed clearly the shift toward to short wavelength with increasing of PVP concentration. Due to the PVP absorption the photons in wavelength range from 230 nm to 400 nm, and thus the blue shift of the absorption edge in the range from 350 nm to 400 nm can be explained by increasing of PVP concentration of the PVP-coated ZnS : Ni0.3% samples.

In order to examine the process of energy transfer in the PVP-coated ZnS : Ni nanoparticles, the PVP and B(5 : 3) samples were measured by the PL, the PLE spectra as in Figures 7 and 8, respectively. It is interesting to see that the PVP is emissive with peak maximum at 394 nm with the exciting wavelength of 325 nm. Simultaneously, the PLE spectrum recorded at 394 nm emission of PVP shows peak maximum at 332 nm in Figure 7 (inset). This excitation
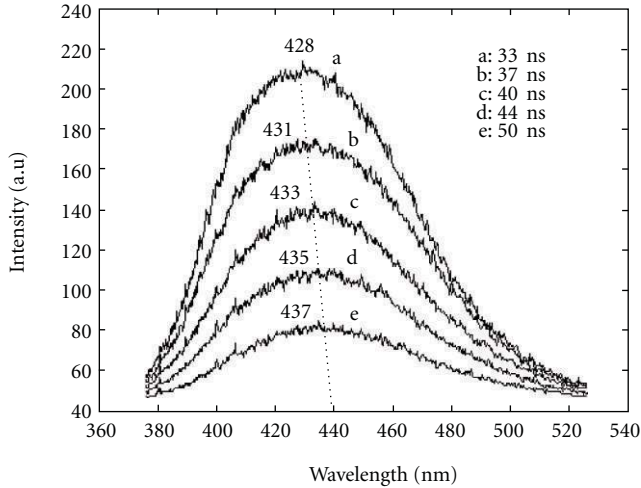
FIGURE 9: The time-resolved PL spectra of PVP at 300 K excited by pulse N_2 laser with 337 nm wavelength, pulse width of 7 ns, and frequency of 10 Hz. The delay times after the excitation pulse are 33 ns, 37 ns, 40 ns, 44 ns, and 50 ns, respectively.

FIGURE 10: The PL decay curve of PVP.

band is attributed to the electronic transitions in PVP molecular orbitals. Alternatively, the blue emission band of PVP at 394 nm is attributed to the radiative relaxation of electrons from the lowest energy unoccupied molecular orbital (LUMO) to the highest energy occupied molecular orbital (HOMO) levels in PVP [31]. As seen in Figure 7 (inset), the PLE band of PVP monitored at 394 nm has a peak maximum at 332 nm, while the PLE band of B(5 : 3) monitored at 520 nm (Figure 8) shows a peak maximum at 395 nm. These results show that the PL peak of 394 nm of PVP sample coincided exactly with the PLE peak of B(5 : 3) sample. Thus, the exciting wavelength of 325 nm is becoming the luminescent emission at 520 nm of the PVP-coated ZnS : Ni samples. From above analysed results of PLE spectra of PVP, B(5 : 3) samples and the PL spectra of the sample systems (Figures 4 and 5) with the exciting wavelength of 325 nm, it is reasonable to suppose that (i) the high energy band in the PLE spectrum of ZnS : Ni-PVP arises from the surface PVP molecules, (ii) the energy transfer occurs between the energy levels of surface PVP molecular orbitals and the luminescence centers of ZnS : Ni, and (iii) the energy transition from surface PVP molecules to the Ni^{2+} centers occurs via hot ZnS.

3.4. Time-Resolved PL Spectra and Luminescence Decay Curves. The investigation of the kinetic decay process of electrons in energy bands is very important to the study of luminescence. It can provide a scientific basis for the improvement of the luminescence efficiency of optical materials. Figure 8 shows the time-resolved PL spectra of PVP at 300 K excited by pulse N_2 laser with 337 nm wavelength, pulse width of 7 ns, and frequency of 10 Hz. These peaks of these spectra are shifted toward longer wavelength from 428 nm to 437 nm with increasing of the delay time from 33 ns to 50 ns. It shows clearly that these peaks belong to the right shoulder in range of 390–470 nm of PL spectrum
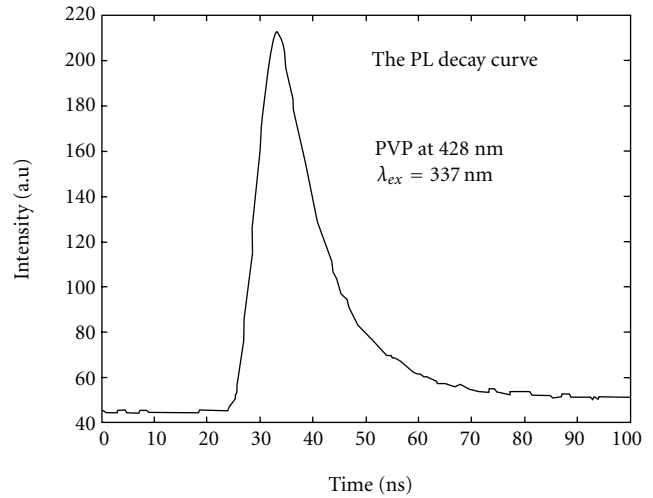
of PVP excited by laser wavelength of 325 nm (in Figure 7). Beside that, Figure 9 also shows that the PL peak intensity decreases while the spectral width of the PL band (full-width at half-maximum) decrease with increasing of the delay time. These PL properties are attributed to electron transition from LUMO to HOMO levels in PVP molecules.

Figure 10 shows the PL decay curve of PVP at 428 nm when using exciting wavelengths 337 nm. The decay curve shows that the number of free photoelectrons in exciting energy bands (corresponding to 428 nm wavelength) is decreased by exponential attenuation and is given by $n \propto e^{-t/\tau}$, where τ is the lifetime of electrons in exciting energy band. From this PL decay curve, the lifetime of free photoelectrons is calculated as $\tau = 15.5$ ns for PVP at 428 nm. The lifetime τ is shorter than that in ZnS : Mn, Cu samples sintered at high temperatures [32]. On the other hand, the lifetime τ is very short, thus it is characteristic of the radiative relaxation of electrons from the lowest energy unoccupied molecular orbital (LUMO) to the highest energy occupied molecular orbital (HOMO) levels in PVP. From the above analyzed results of PVP, the blue luminescence of PVP may be attributed to the radiative relaxation of electrons from LUMO to HOMO levels as in Figure 12.

3.5. On the Energy Transfer from Surface PVP Molecules to the Ni^{2+} Centers. The PVP is a conjugated polymer with both N and C=O groups. So with the ZnS : Ni-PVP samples, it is believed that the bond between metal ions and PVP can give rise to overlapping of molecular orbitals of PVP with atomic orbitals of metal ions in surface regions [23, 31]. Thus, from the above results, we believe that the PVP passivating layers around the ZnS : Ni core described in Figure 11 are formed by coordination bond between the nitrogen atom of PVP and Zn^{2+} [31]. Figure 11 shows the incomplete coverage with low concentration of PVP (Figure 11(a)) and the complete coverage with higher concentration of PVP (Figure 11(b)).
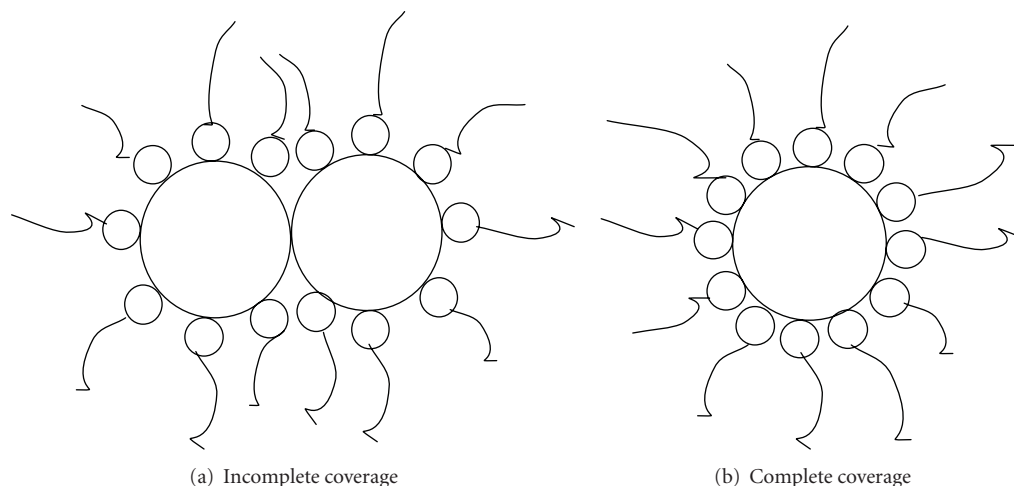
(a) Incomplete coverage   (b) Complete coverage

Figure 11: The PVP coverage of ZnS : Ni grains.

(a) Blue emitssion by electronic transitions from LUMO to HOMO
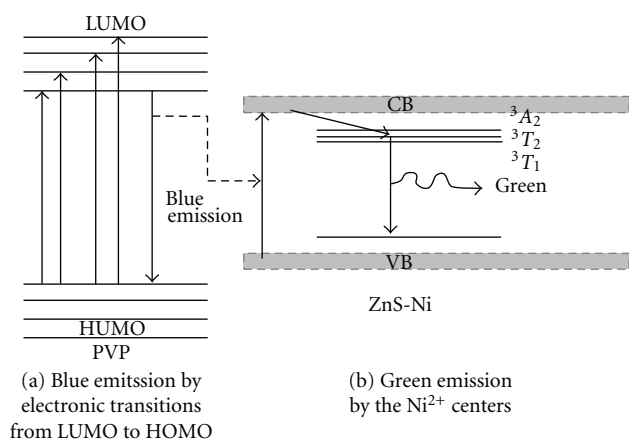
(b) Green emission by the Ni^{2+} centers

Figure 12: Schematic illustration of various electronic transition and energy transfer processes in ZnS : Ni-PVP.

It is clear from these above analyzed results of the PL spectra, PLE spectra, time-resolved PL spectra, and luminescence decay curves of PVP and PVP-coated ZnS : Ni samples that the energy transition process from surface PVP molecules to the Ni^{2+} centers occurs via hot ZnS illustrated as in Figures 12(a) and 12(b).

4. Conlusion

From the above experimental results, the influence of surface passivation on the luminescence intensity of ZnS : Ni nanoparticles has been observed due to efficient energy transfer from the surface PVP molecules to the Ni^{2+} centers in ZnS : Ni nanoparticles. With increasing the PVP concentration, the absorption edge of the PVP-coated ZnS : Ni nanoparticles shows the blue shift, which is explained due to the influence of PVP concentration on the shift of the absorption spectra.

References

[1] C. R. McNeill, "Imaging the domain structure of organic semiconductor films," *Journal of Polymer Science B*, vol. 49, no. 13, pp. 909–919, 2011.

[2] B. Jarzabek, J. Weszka, M. Domański, J. Jurusik, and J. Cisowski, "Optical studies of aromatic polyazomethine thin films," *Journal of Non-Crystalline Solids*, vol. 354, no. 10-11, pp. 856–862, 2008.

[3] B. Jarzabek, J. Weszka, M. Domanski, J. Jurusik, and J. Cisowski, "Optical properties of amorphous polyazomethine thin films," *Journal of Non-Crystalline Solids*, vol. 352, no. 9–20, pp. 1660–1662, 2006.

[4] B. Jarzabek, E. Schab-Balcerzak, T. Chamenko, D. Sek, J. Cisowski, and A. Volozhin, "Optical properties of new aliphatic-aromatic co-polyimides," *Journal of Non-Crystalline Solids*, vol. 299–302, no. 2, pp. 1057–1061, 2002.

[5] B. Hajduk, J. Weszka, V. Cozan, B. Kaczmarczyk, B. Jarzabek, and M. Domanski, "Optical properties of polyazomethine with oxygen atom in the backbon," *Archives of Materials Science and Engineering*, vol. 32, no. 2, pp. 85–88, 2008.

[6] R. H. Friend, "Conjugated polymers. New materials for optoelectronic devices," *Pure and Applied Chemistry*, vol. 73, no. 3, pp. 425–430, 2001.

[7] D. Sek, A. Iwan, B. Jarzabek et al., "Characterization and optical properties of oligoazomethines with triphenylamine moieties exhibiting blue, blue-green and green light," *Spectrochimica Acta A*, vol. 72, no. 1, pp. 1–10, 2009.

[8] A. Cihaner and F. Algi, "Electrochemical and optical properties of an azo dye based conducting copolymer," *Turkish Journal of Chemistry*, vol. 33, no. 6, pp. 759–767, 2009.

[9] N. Dubey and M. Leclerc, "Conducting polymers: efficient thermoelectric materials," *Journal of Polymer Science B*, vol. 49, no. 7, pp. 467–475, 2011.

[10] A. C. Sparavigna, L. Florio, J. Avloni, and A. Henn, "Polypyrrole coated PET fabrics for thermal applications," *Materials Sciences and Applications*, vol. 1, pp. 253–259, 2011.

[11] T. Agostinelli, T. A. M. Ferenczi, E. Pires et al., "The role of alkane dithiols in controlling polymer crystallization in small band gap polymer: fullerene solar sells," *Journal of Polymer Science B*, vol. 49, no. 10, pp. 717–724, 2011.

[12] N. C. Miller, R. Gysel, C. E. Miller et al., "The phase behavior of a polymer-fullerene bulk heterojunction system that contains bimolecular crystals," *Journal of Polymer Science B*, vol. 49, no. 7, pp. 499–503, 2011.

[13] P. Yang, M. Lü, D. Xü et al., "Strong green luminescence of Ni^{2+}-doped ZnS nanocrystals," *Applied Physics A*, vol. 74, no. 2, pp. 257–259, 2002.

[14] Y. Hattori, T. Isobe, H. Takahashi, and S. Itoh, "Luminescent properties of $ZnS:Mn^{2+}$ nanocrystals/SiO_2 hybrid phosphor synthesized by in situ surface modification co-precipitation," *Journal of Luminescence*, vol. 113, no. 1-2, pp. 69–78, 2005.

[15] P. Yang, M. Lü, D. Xu et al., "Luminescence characteristics of ZnS nanoparticles co-doped with Ni^{2+} and Mn^{2+}," *Optical Materials*, vol. 24, no. 3, pp. 497–502, 2003.

[16] H. Soni, M. Chawda, and D. Bodas, "Electrical and optical characteristics of Ni doped ZnS clusters," *Materials Letters*, vol. 63, no. 9-10, pp. 767–769, 2009.

[17] R. Sharma, H. S. Bhatti, and K. Kyhm, "Enhanced oscillator strengths and optical parameters of doped ZnS bulk and nanophosphors," *Applied Physics B*, vol. 97, no. 1, pp. 145–155, 2009.

[18] C. M. Huang, L. C. Chen, G. T. Pan, T. C. K. Yang, W. S. Chang, and K. W. Cheng, "Effect of Ni on the growth and photoelectrochemical properties of ZnS thin films," *Materials Chemistry and Physics*, vol. 117, no. 1, pp. 156–162, 2009.

[19] H. R. Pouretedal, A. Norozi, M. H. Keshavarz, and A. Semnani, "Nanoparticles of zinc sulfide doped with manganese, nickel and copper as nanophotocatalyst in the degradation of organic dyes," *Journal of Hazardous Materials*, vol. 162, no. 2-3, pp. 674–681, 2009.

[20] N. S. A. Sharif, N. S. Ridhuan, Z. A. Ahmad, and S. D. Hutagalung, "Structural analysis of zinc sulphide nanopartiles synthesized via wet chemical route," *Solid State Science and Technology*, vol. 18, no. 1, pp. 91–95, 2010.

[21] L. Wang, X. T. Tao, J. X. Yang, Y. Ren, Z. Liu, and M. H. Jiang, "Preparation and characterization of the ZnS nanospheres with narrow size distribution," *Optical Materials*, vol. 28, no. 8-9, pp. 1080–1083, 2006.

[22] R. Maity, U. N. Maiti, M. K. Mitra, and K. K. Chattopadhyay, "Synthesis and optical characterization of polymer-capped nanocrystalline ZnS thin films by chemical process," *Physica E*, vol. 33, no. 1, pp. 104–109, 2006.

[23] G. Ghosh, M. Kanti Naskar, A. Patra, and M. Chatterjee, "Synthesis and characterization of PVP-encapsulated ZnS nanoparticles," *Optical Materials*, vol. 28, no. 8-9, pp. 1047–1053, 2006.

[24] S. K. Panda, A. Datta, and S. Chaudhuri, "Nearly monodispersed ZnS nanospheres: synthesis and optical properties," *Chemical Physics Letters*, vol. 440, no. 4–6, pp. 235–238, 2007.

[25] M. Pattabi, B. Saraswathi Amma, K. Manzoor, and Ganesh Sanjeev, "Effect of 8 MeV electron irradiation on the optical properties of PVP capped CdS nanoparticles in PVA matrix," *Solar Energy Materials and Solar Cells*, vol. 91, no. 15-16, pp. 1403–1407, 2007.

[26] G. Murugadoss, "Synthesis and optical characterization of PVP and SHMP-encapsulated Mn^{2+} ZnS nanocrystals," *Journal of Luminescence*, vol. 130, no. 11, pp. 2207–2214, 2010.

[27] K. Manzoor, S. R. Vadera, N. Kumar, and T. R. N. Kutty, "Synthesis and photoluminescent properties of ZnS nanocrystals doped with copper and halogen," *Materials Chemistry and Physics*, vol. 82, no. 3, pp. 718–725, 2003.

[28] G. Murugadoss, B. Rajamannan, and V. Ramasamy, "Synthesis and photoluminescence study of PVA-capped $ZnS:Mn^{2+}$ nanoparticles," *Digest Journal of Nanomaterials and Biostructures*, vol. 5, no. 2, pp. 339–345, 2010.

[29] L. Levy, J. F. Hochepied, and M. P. Pileni, "Control of the size and composition of three dimensionally diluted magnetic semiconductor clusters," *Journal of Physical Chemistry*, vol. 100, no. 47, pp. 18322–18326, 1996.

[30] A. Twardowski, T. Dietl, and M. Demianiuk, "The study of the s-d type exchange interaction in Zn1-xMnxSe mixed crystals," *Solid State Communications*, vol. 48, no. 10, pp. 845–848, 1983.

[31] K. Manzoor, S. R. Vadera, N. Kumar, and T. R. N. Kutty, "Energy transfer from organic surface adsorbate-polyvinyl pyrrolidone molecules to luminescent centers in ZnS nanocrystals," *Solid State Communications*, vol. 129, no. 7, pp. 469–473, 2004.

[32] G. Dong, X. Li, Z. Wei, S. Yang, and G. Fu, "Measurement of the time-resolved spectrum of photoelectrons from ZnS:Mn, Cu luminescent material," *Journal of Physics Condensed Matter*, vol. 15, no. 9, pp. 1495–1503, 2003.

Research Article

Relationship between Crystal Shape, Photoluminescence, and Local Structure in SrTiO₃ Synthesized by Microwave-Assisted Hydrothermal Method

Luís F. da Silva,[1] Waldir Avansi,[2] Mário L. Moreira,[2] Alexandre Mesquita,[3] Lauro J. Q. Maia,[4] Juan Andrés,[5] Elson Longo,[2] and Valmor R. Mastelaro[1]

[1] *Instituto de Física de São Carlos, Universidade de São Paulo, 13560-970 São Carlos, SP, Brazil*
[2] *Instituto de Química, Universidade Estadual Paulista, 14800-900 Araraquara, SP, Brazil*
[3] *Departamento de Física, Universidade Federal de São Carlos, 13565-905 São Carlos, SP, Brazil*
[4] *Instituto de Física, Universidade Federal Goiás, 74001-970 Goiânia, GO, Brazil*
[5] *Departamento de Química Física y Analítica, Universitat Jaume I 12071 Castelló, Spain*

Correspondence should be addressed to Luís F. da Silva, lfsilva@ursa.ifsc.usp.br

Received 30 November 2011; Revised 1 February 2012; Accepted 15 March 2012

Academic Editor: J. C. Sczancoski

This paper describes the effect of using different titanium precursors on the synthesis and physical properties of SrTiO₃ powders obtained by microwave-assisted hydrothermal method. X-ray diffraction measurements, X-ray absorption near-edge structure (XANES) spectroscopy, field emission scanning electron microscopy (FE-SEM), and high-resolution transmission electron microscopy (HRTEM) were carried out to investigate the structural and optical properties of the SrTiO₃ spherical and cubelike-shaped particles. The appropriate choice of the titanium precursor allowed the control of morphological and photoluminescence (PL) properties of SrTiO₃ compound. The PL emission was more intense in SrTiO₃ samples composed of spherelike particles. This behavior was attributed to the existence of a lower amount of defects due to the uniformity of the spherical particles.

1. Introduction

Perovskite-type oxides are some of the most fascinating materials in condensed-matter research. Strontium titanate, SrTiO₃ (STO), is a representative member of this family; it displays a cubic structure and is an important n-type semiconductor with a band gap of approximately 3.2 eV [1].

STO has been widely studied and applied in catalyses [2], resistive oxygen gas sensors [3], solar cells [4], and random access memory [5]. Several papers have reported that its potential for technological applications is strongly related to the crystalline structure, particle size, and morphology [6–8]. Different studies have shown that the route, the precursors, and/or the parameters of synthesis appear as a key factor to control the ability to engineer crystal morphologies with desirable properties [9–12]. For example, it is well known that morphology and grain size are directly related to dielectric properties, ferroelectric polarization, and related

materials [13]. Additionally, the photoluminescence (PL) properties of different perovskite oxide compounds are dependent on morphological features [7, 14–18].

The interest in compounds with perovskite-type structure that show PL properties has increased. The PL properties of disordered ATiO₃ compounds, synthesized by polymeric precursor method, have been extensively studied in our research group [19–25]. The origin of PL properties in these materials has been investigated by several experimental techniques and related to local order-disorder effects around Ti atoms, that is, the local disorder around the network former atom [19–23, 25].

X-ray absorption near-edge structure (XANES) spectroscopy has been employed to investigate the local structure around the titanium atoms [19–23, 25–28]. The main advantage of XANES technique is the possibility to characterize compounds without a long-order periodic structure,

specially amorphous solids. Previous studies on the Ti K-edge XANES spectra of STO amorphous samples have showed the existence of two types of Ti symmetries, fivefold (TiO_5) and sixfold (TiO_6) coordination [22]. Moreover, in the case of STO prepared by polymeric precursor method, it was observed that the reduction in the amount of TiO_5 units led to a reduction in the PL intensity [22].

Recently, PL properties have been observed in crystalline $ATiO_3$ prepared by the microwave-assisted hydrothermal (MAH) method [26, 27]. This method provides kinetic enhancement, low reaction temperature, and time reduction and generates compounds with controlled morphology and size [11, 28]. In this case, the observation of the PL property has been attributed to a tilt in the TiO_6 octahedron caused by the presence of OH^- groups and vacancies in A-site [26, 27].

The influence of synthesis parameters on the physical properties of STO samples prepared by the hydrothermal method has been widely investigated [2, 12, 29–34]. However, to the best of our knowledge, this is the first study that analyses the effect of titanium precursor on crystal-shape, photoluminescent, and structural properties of STO powders synthesized by MAH method.

Motivated by this consideration, this paper reports on the effect of using two different titanium precursors, titanium chloride and titanium oxysulfate, on the short-order local structure and optical and morphological properties of $SrTiO_3$ (STO) powders prepared by the MAH method. The STO samples were characterized by X-ray diffraction measurements, field emission scanning electron microscopy (FE-SEM), high-resolution transmission electron microscopy (HR-TEM), Ti K-edge XANES spectroscopy, and photoluminescence spectroscopy.

2. Experimental

In order to study the effect of titanium precursor, two different solutions of $SrTiO_3$ samples, denoted as SAM1 and SAM2, were prepared.

Sample 1 (SAM1) was prepared by slowly adding 0.01 mol of $TiCl_4$ (99.95%, Sigma-Aldrich) to 50 mL of cold deionized water under stirring to obtain a homogeneous solution. 0.01 mol of $SrCl_2 \cdot 2H_2O$ (99.9%, Sigma-Aldrich) was dissolved into the solution under constant stirring and purged with nitrogen gas (12 $cm^3 \cdot min^{-1}$) at 60°C. Then, 50 mL of 6 M KOH (P.A, Sigma-Aldrich) solution was added to the precursor solution under constant stirring and nitrogen flux.

For Sample 2 (SAM2) the solution was prepared adding 0.01 mol of $TiOSO_4 \cdot xH_2SO_4 \cdot xH_2O$ (99.9%, Sigma-Aldrich) to 50 mL of warm deionized water at 60°C under continuous stirring and nitrogen flux (12 $cm^3 \cdot min^{-1}$). In the sequence, 0.01 mol of $SrCl_2$ was dissolved into the solution and a 50 mL of 6 M KOH solution was added to the solution under stirring and nitrogen flux.

After the addition of KOH solution, each precursor solution was transferred separately in a 110 mL Teflon autoclave, sealed, and inserted in the microwave hydrothermal equipment, using a frequency of 2.45 GHz with maximum
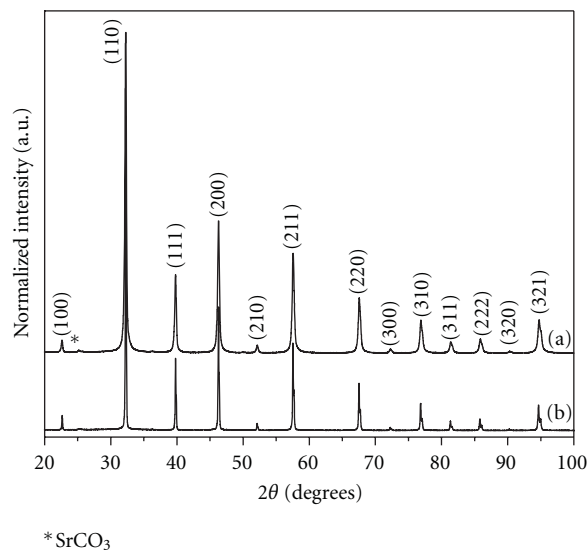

FIGURE 1: XRD patterns of $SrTiO_3$ powders obtained using different titanium precursors: (a) SAM1, and (b) SAM2 samples.

power of 800 W. The precursor solutions were heat-treated at 140°C for 10 minutes with a heating rate of 140°C·min^{-1} and under constant pressure of 3 bar. After the synthesis, the autoclave was naturally cooled to room temperature. Then, each precipitated white powder was washed with warm deionized water for several times until attaining a neutral pH. The powder samples were dried at 80°C for 12 hours in a hot plate.

X-ray diffraction (XRD) measurements were taken in a Rigaku Rotaflex RU200B diffractometer, using Cu$K\alpha$ radiation. The data were collected in a 2θ range from 20 to 100° using a fixed-time mode with a 0.02° step and 5 s/point. The morphological characterization was performed by field emission scanning electron microscopy (FE-SEM, Zeiss SUPRA35) and in a transmission electron microscope (TEM, JEOL JEM 2010 URP) operating, respectively, at 5 and 200 kV. Photoluminescence (PL) spectra were collected by emission spectra obtained in a Fluorolog FL-322 Horiba/Jobin-Yvon spectrofluorimeter, with a 450 W xenon lamp for steady-state luminescence spectra and a Hamamatsu photomultiplier. The emission was corrected for the spectral response of the monochromators and by the detector using a typical correction spectrum provided by the manufacturer. STO samples were excited by 410 nm wavelength.

The titanium K-edge X-ray absorption spectra were collected at the LNLS (Brazilian Synchrotron Light Laboratory) facility using the D04B-XAS1 beamline. The LNLS storage ring was operated at 1.36 GeV and 100–160 mA. XAS spectra of grounded samples were collected at the Ti K-edge (4966 eV) in transmission mode at room temperature using Si(111) channel-cut monochromator. XANES spectra at the Ti K-edge were recorded for each sample between 4910 and 5200 eV using energy steps of 0.3 eV. Moreover, for comparison among the samples, all spectra were background
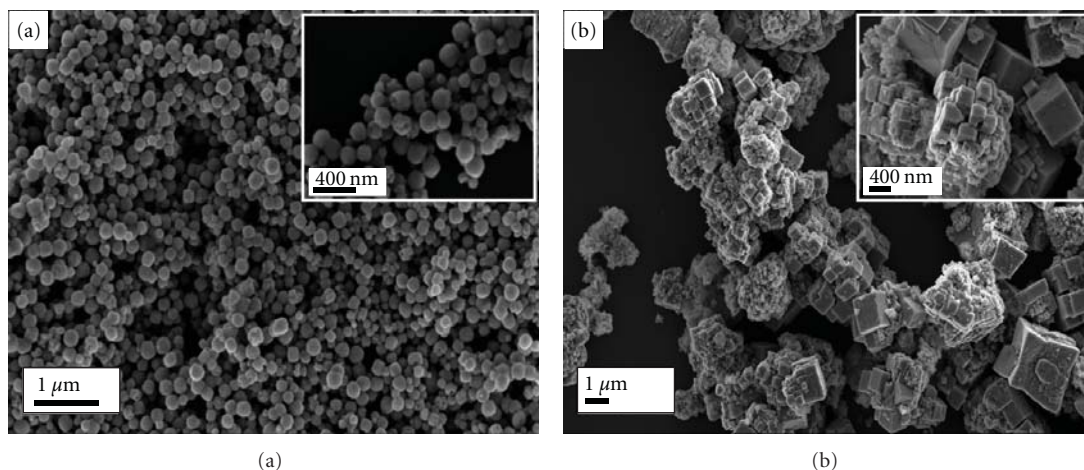
FIGURE 2: FE-SEM images of SrTiO₃ powders obtained with different precursors: (a) SAM1 and (b) SAM2 samples.
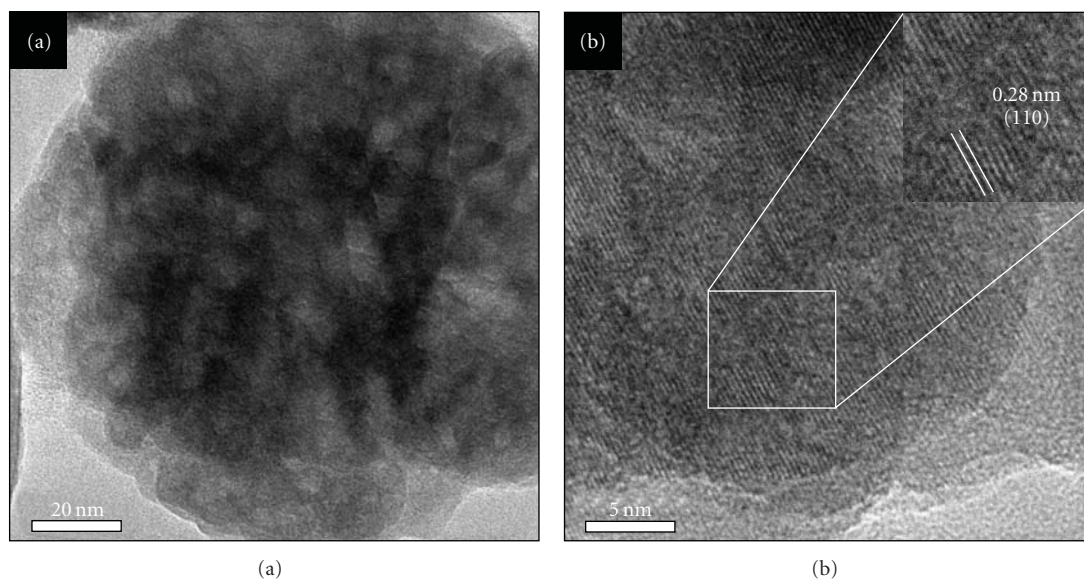

FIGURE 3: (a) TEM and (b) HR-TEM images of the SAM1 sample.

removed and normalized using the first EXAFS (Extended X-ray Absorption Fine Structure) oscillation, as unity. XANES spectra were processed by the Multiplatform Applications for XAFS code (MAX) [35].

3. Results and Discussions

XRD patterns of STO samples prepared using different titanium precursors are presented in Figure 1. From the analysis of this figure, it is clear that all diffraction peaks are related to a cubic perovskite structure with lattice constant $a = 3.90\,\text{Å}$ and $Pm3m$ (221) space group (JCPDS card no: 35-0734). For SAM1 sample, a lower intensity peak related to $SrCO_3$ phase (JCPDS card no: 05-0418) was observed at $25.3°$.

In order to check the morphology of STO samples synthesized with different titanium precursors, FE-SEM images were obtained. As shown in Figure 2(a), the morphology of SAM1 sample consists of STO spherical particles of ca. 150 nm, whereas the morphology of SAM2 sample consists of agglomerated particles in superstructures ($\sim1.5\,\mu$m), exhibiting a cubelike shape. Figure 3 shows the TEM images of SAM1 sample. Although the apparent morphology of this sample has a nanospherical-like shape at around 150 nm, the TEM and HR-TEM images presented in Figures 3(a) and 3(b) reveal that these nanoparticles consist of aggregates of small nanocrystals of ca. 25 nm. From the analysis of an expanded HR-TEM image in Figure 3(b), the nanocrystal interplanar distance was determined as 0.28 nm and related to the (110) crystallographic planes of STO perovskite cubic structure, which agrees with XRD results. It is also possible to observe that the nanospherical particles present a lower contrast between the crystallites, showing the existence of nanopores separating the primary particles, already observed
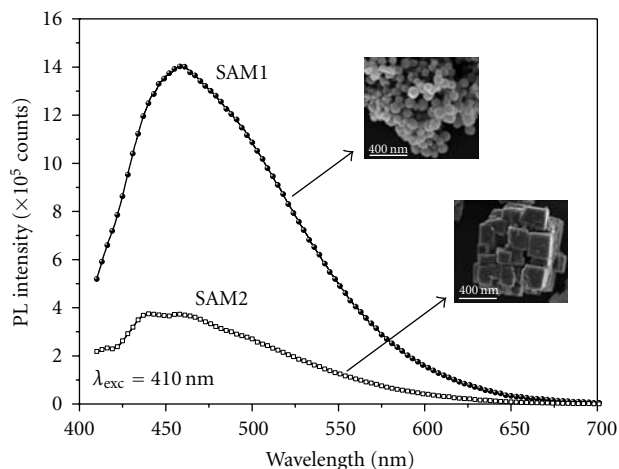
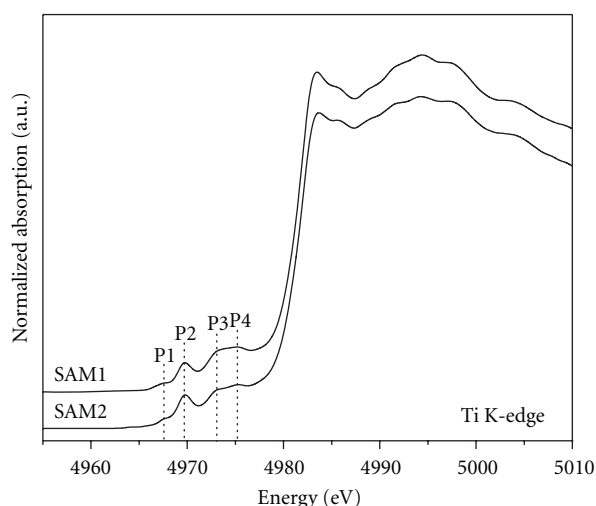Figure 4: Room temperature photoluminescence spectra of SrTiO₃ samples with different shapes.

Figure 5: Ti K-edge XANES spectra of SrTiO₃ samples.

during the process of STO nanostructures growth [36, 37]. Calderone and co-workers studied the synthesis of STO nanostructures by coprecipitation method and proposed that the aggregates were composed of small nanocrystals originated from an oriented attachment assisted by the self-assembly process of small primary nanocrystals [32]. As seen in the TEM images of SAM1 sample, the aggregation of these small particles is irreversible and occurs in a highly oriented manner, leading to the elimination of the interface of adjacent crystals. This growth mechanism has been also observed in several compounds synthesized by hydrothermal method [10, 38–40].

Figure 4 shows the photoluminescence (PL) emission spectra at room temperature of SAM1 (spherelike) and SAM2 (cubelike) samples. The PL spectra exhibit a broad blue emission centered at 460 nm for SAM1 sample and between 440 and 460 nm for SAM2 sample. Comparing both samples, it is clear that the SAM1 sample shows a higher emission intensity compared to SAM2. This behavior

has been observed in samples with particles that exhibit a spherical geometry and higher emission intensity than particles with other morphologies [7, 15, 17]. According to these studies, the intrinsic geometry of the spherical particles minimizes the scattering of light from the particle surfaces in comparison to a cube-shaped particle [7, 15, 17]. Besides, the enhancement of the PL emission can also be attributed to a reduction in the surface defects and the higher uniformity in shape of the superstructures [7, 14, 17].

Several papers have reported the relationship between the local order structure of titanium atoms and the photoluminescent properties of titanate compounds synthesized by polymeric precursor method [19, 20, 22, 23, 25]. According to Longo and co-workers, the reduction in the PL intensity in function of the annealing temperature of STO samples is due to a reduction in the local disorder around titanium atoms [22]. In order to check the dependence of the local order structure of the studied samples and the behavior of PL as a function of titanium precursor, Ti K-edge XANES spectra of STO samples were measured and are shown in Figure 5. These spectra present four pre-edge transitions labeled P1, P2, P3, and P4. Transition P1 is caused by a quadrupole excitation of $1s$ electron to t_{2g} orbitals of the TiO₆ octahedron [41], while transition P2 occurs due to the $1s$ electron transition to the unoccupied $3d$ level; this forbidden electronic transition can be allowed if there occurs a mixture of oxygen $2p$ states and empty titanium $3d$ states [27, 42]. The intensity of peak P2 has shown to be sensitive to the local structure around titanium atoms [19, 43]. Transitions P3 and P4 are assigned to the dipole excitation of the $1s$ electron into the t_{2g} and e_g orbitals of the neighboring TiO₆ octahedra [41, 44].

As observed in Figure 5, Ti K-edge XANES spectra of SAM1 and SAM2 samples are very similar, especially in the pre-edge region (4960 to 4980 eV), with a pre-edge typical of sixfold coordination (TiO₆) compounds [22, 45]. Moreover, after the edge, the oscillations observed in both samples are also quite similar, indicating the same neighborhood around the titanium atoms. Based on the analysis of the XANES spectra, it can be stated that the titanium atoms local symmetry, that is, the TiO₆ octahedra, and the medium-range order around titanium atoms are not affected by the use of different titanium precursors employed in the synthesis of STO powders. This result has confirmed that the variation observed in the PL emission is more related to the particle morphology of SAM1 and SAM2 samples.

4. Conclusion

This study has evidenced that an appropriate selection of titanium precursor allows a control of morphology and PL property of STO powders obtained by using the microwave-hydrothermal method. The use of titanium chloride as the precursor leads to the formation of STO samples of spherical morphology, whereas cubelike particles are formed by the spontaneous assembly of small primary nanocrystals when titanium oxysulfate is used as a precursor. The analysis of XANES spectra allowed observing that change in the crystal

morphology does not affect the local order symmetry of TiO_6 octahedra as well as the medium range order around titanium atoms. The PL emission was more intense in spherelike particles in comparison to cubelike particles. This behavior was attributed to the existence of a lower amount of defects due to the uniformity of the spherical particles.

Acknowledgments

References

[1] M. Cardona, "Optical properties and band structure of $SrTiO_3$ and $BaTiO_3$," *Physical Review*, vol. 140, no. 2A, pp. A651–A655, 1965.

[2] Z. K. Zheng, B. B. Huang, X. Y. Qin, X. Y. Zhang, and Y. Dai, "Facile synthesis of $SrTiO_3$ hollow microspheres built as assembly of nanocubes and their associated photocatalytic activity," *Journal of Colloid and Interface Science*, vol. 358, no. 1, pp. 68–72, 2011.

[3] F. Voigts, T. Damjanovic, G. Borchardt, C. Argirusis, and W. Maus-Friedrichs, "Synthesis and characterization of strontium titanate nanoparticles as potential high temperature oxygen sensor material," *Journal of Nanomaterials*, vol. 2006, Article ID 63154, pp. 1–6, 2006.

[4] S. Burnside, J. E. Moser, K. Brooks, M. Gratzel, and D. Cahen, "Nanocrystalline mesoporous strontium titanate as photo-electrode material for photosensitized solar devices: increasing photovoltage through flatband potential engineering," *Journal of Physical Chemistry B*, vol. 103, no. 43, pp. 9328–9332, 1999.

[5] R. Waser and M. Aono, "Nanoionics-based resistive switching memories," *Nature Materials*, vol. 6, no. 11, pp. 833–840, 2007.

[6] L. F. da Silva, L. J. Q. Maia, M. I. B. Bernardi, J. A. Andres, and V. R. Mastelaro, "An improved method for preparation of $SrTiO_3$ nanoparticles," *Materials Chemistry and Physics*, vol. 125, no. 1-2, pp. 168–173, 2011.

[7] H. J. Zhou, Y. B. Mao, and S. S. Wong, "Shape control and spectroscopy of crystalline $BaZrO_3$ perovskite particles," *Journal of Materials Chemistry*, vol. 17, pp. 1707–1713, 2007.

[8] Y. Hu, O. K. Tan, and W. G. Zhu, "Nanosized metal-oxide semiconducting $SrTi_{1\pm x}O_{3-\delta}$ oxygen gas sensors for low-temperature application," *IEEE Sensors Journal*, vol. 6, no. 6, pp. 1389–1394, 2006.

[9] M. Alfredsson, F. Cora, D. P. Dobson et al., "Dopant control over the crystal morphology of ceramic materials," *Surface Science*, vol. 601, no. 21, pp. 4793–4800, 2007.

[10] C. J. Dalmaschio, C. Ribeiro, and E. R. Leite, "Impact of the colloidal state on the oriented attachment growth mechanism," *Nanoscale*, vol. 2, no. 11, pp. 2336–2345, 2010.

[11] I. Bilecka and M. Niederberger, "Microwave chemistry for inorganic nanomaterials synthesis," *Nanoscale*, vol. 2, no. 8, pp. 1358–1374, 2010.

[12] W. Dong, B. Li, Y. Li et al., "General approach to well-defined perovskite $MTiO_3$ (M = Ba, Sr, Ca, and Mg) nanostructures," *Journal of Physical Chemistry C*, vol. 115, no. 10, pp. 3918–3925, 2011.

[13] S. Berger and Y. Drezner, "Nano-domains in thin $BaTiO_3$ films," *Ferroelectrics*, vol. 327, no. 1, pp. 85–89, 2005.

[14] C. Xu, D. B. Zou, H. Guo, F. Jie, and T. K. Ying, "Luminescence properties of hierarchical $CaMoO_4$ microspheres derived by ionic liquid-assisted process," *Journal of Luminescence*, vol. 129, no. 5, pp. 474–477, 2009.

[15] L. Xu, C. L. Lu, Z. H. Zhang, X. Y. Yang, and W. H. Hou, "Various self-assembled three-dimensional hierarchical architectures of $La_2(MoO_4)_3$: controlled synthesis, growth mechanisms, luminescence properties and adsorption activities," *Nanoscale*, vol. 2, no. 6, pp. 995–1005, 2010.

[16] W. S. Wang, Y. X. Hu, J. Goebl, Z. D. Lu, L. Zhen, and Y. D. Yin, "Shape-and size-controlled synthesis of calcium molybdate doughnut-shaped microstructures," *Journal of Physical Chemistry C*, vol. 113, no. 37, pp. 16414–16423, 2009.

[17] Z. G. Lu, Y. G. Tang, L. M. Chen, and Y. D. Li, "Shape-controlled synthesis and characterization of $BaZrO_3$ microcrystals," *Journal of Crystal Growth*, vol. 266, no. 4, pp. 539–544, 2004.

[18] A. Kar, S. Kundu, and A. Patra, "Surface defect-related luminescence properties of SnO_2 nanorods and nanoparticles," *Journal of Physical Chemistry C*, vol. 115, no. 1, pp. 118–124, 2011.

[19] S. de Lazaro, J. Milanez, A. T. de Figueiredo et al., "Relation between photoluminescence emission and local order-disorder in the $CaTiO_3$ lattice modifier," *Applied Physics Letters*, vol. 90, no. 11, Article ID 111904, 3 pages, 2007.

[20] A. T. de Figueiredo, V. M. Longo, S. de Lazaro et al., "Blue-green and red photoluminescence in $CaTiO_3$: Sm," *Journal of Luminescence*, vol. 126, no. 2, pp. 403–407, 2007.

[21] E. Longo, A. T. de Figueiredo, M. S. Silva et al., "Influence of structural disorder on the photoluminescence emission of PZT powder," *Journal of Physical Chemistry A*, vol. 112, no. 38, pp. 8953–8957, 2008.

[22] V. M. Longo, A. T. de Figueiredo, S. de Lazaro et al., "Structural conditions that leads to photoluminescence emission in $SrTiO_3$: an experimental and theoretical approach," *Journal of Applied Physics*, vol. 104, no. 2, Article ID 023515, 11 pages, 2008.

[23] F. M. Pontes, E. Longo, E. R. Leite et al., "Photoluminescence at room temperature in amorphous $SrTiO_3$ thin films obtained by chemical solution deposition," *Materials Chemistry and Physics*, vol. 77, no. 2, pp. 598–602, 2003.

[24] L. Gracia, J. Andres, V. M. Longo, J. A. Varela, and E. Longo, "A theoretical study on the photoluminescence of $SrTiO_3$," *Chemical Physics Letters*, vol. 493, no. 1–3, pp. 141–146, 2010.

[25] E. A. V. Ferri, J. C. Sczancoski, L. S. Cavalcante et al., "Photoluminescence behavior in $MgTiO_3$ powders with vacancy/distorted clusters and octahedral tilting," *Materials Chemistry and Physics*, vol. 117, no. 1, pp. 192–198, 2009.

[26] M. L. Moreira, G. P. Mambrini, D. P. Volanti et al., "Hydrothermal microwave: a new route to obtain photoluminescent crystalline $BaTiO_3$ nanoparticles," *Chemistry of Materials*, vol. 20, no. 16, pp. 5381–5387, 2008.

[27] M. L. Moreira, E. C. Paris, G. S. do Nascimento et al., "Structural and optical properties of $CaTiO_3$ perovskite-based materials obtained by microwave-assisted hydrothermal synthesis:

an experimental and theoretical insight," *Acta Materialia*, vol. 57, no. 17, pp. 5174–5185, 2009.

[28] M. L. Moreira, J. Andres, J. A. Varela, and E. Longo, "Synthesis of fine micro-sized BaZrO$_3$ powders based on a decaoctahedron shape by the microwave-assisted hydrothermal method," *Crystal Growth and Design*, vol. 9, no. 2, pp. 833–839, 2009.

[29] W. Dong, X. Li, J. Yu et al., "Porous SrTiO$_3$ spheres with enhanced photocatalytic performance," *Materials Letters*, vol. 67, no. 1, pp. 131–134, 2012.

[30] Y. M. Rangel-Hernandez, J. C. Rendon-Angeles, Z. Matamoros-Veloza, M. I. Pech-Canul, S. Diaz-de la Torre, and K. Yanagisawa, "One-step synthesis of fine SrTiO$_3$ particles using SrSO$_4$ ore under alkaline hydrothermal conditions," *Chemical Engineering Journal*, vol. 155, no. 1-2, pp. 483–492, 2009.

[31] Y. Li, X. P. Gao, G. L. Pan, G. R. Li, T. Y. Yan, and H. Y. Zhu, "Titanate nanofiber reactivity: fabrication of MTiO$_3$ (M = Ca, Sr, and Ba) perovskite oxides," *Journal of Physical Chemistry C*, vol. 113, no. 11, pp. 4386–4394, 2009.

[32] V. R. Calderone, A. Testino, M. T. Buscaglia et al., "Size and shape control of SrTiO$_3$ particles grown by epitaxial self-assembly," *Chemistry of Materials*, vol. 18, no. 6, pp. 1627–1633, 2006.

[33] H. Xu, S. Wei, H. Wang, M. Zhu, R. Yu, and H. Yan, "Preparation of shape controlled SrTiO$_3$ crystallites by sol-gel-hydrothermal method," *Journal of Crystal Growth*, vol. 292, no. 1, pp. 159–164, 2006.

[34] X. Wei, G. Xu, Z. Ren et al., "Single-crystal-like mesoporous SrTiO$_3$ spheres with enhanced photocatalytic performance," *Journal of the American Ceramic Society*, vol. 93, no. 5, pp. 1297–1305, 2010.

[35] A. Michalowicz, J. Moscovici, D. Muller-Bouvet, and K. Provost, "MAX: multiplatform applications for XAFS," in *Proceedings of the 14th International Conference on X-Ray Absorption Fine Structure*, A. DiCicco and A. Filipponi, Eds., Iop Publishing, Camerino, Italy, 2009.

[36] F. A. Rabuffetti, H. S. Kim, J. A. Enterkin et al., "Synthesis-dependent first-order Raman scattering in SrTiO$_3$ nanocubes at room temperature," *Chemistry of Materials*, vol. 20, no. 17, pp. 5628–5635, 2008.

[37] W. Avansi Jr., C. Ribeiro, E. R. Leite, and V. R. Mastelaro, "Growth kinetics of vanadium pentoxide nanostructures under hydrothermal conditions," *Journal of Crystal Growth*, vol. 312, no. 23, pp. 3555–3559, 2010.

[38] M. Niederberger and H. Colfen, "Oriented attachment and mesocrystals: non-classical crystallization mechanisms based on nanoparticle assembly," *Physical Chemistry Chemical Physics*, vol. 8, no. 28, pp. 3271–3287, 2006.

[39] M. L. Moreira, J. Andres, V. R. Mastelaro, J. A. Varela, and E. Longo, "On the reversed crystal growth of BaZrO$_3$ decaoctahedron: shape evolution and mechanism," *CrystEngComm*, vol. 13, no. 19, pp. 5818–5824, 2011.

[40] C. Ribeiro, C. Vila, D. B. Stroppa et al., "Anisotropic growth of oxide nanocrystals: Insights into the rutile TiO$_2$ phase," *Journal of Physical Chemistry C*, vol. 111, no. 16, pp. 5871–5875, 2007.

[41] P. P. Neves, A. C. Doriguetto, V. R. Mastelaro et al., "XAS and XRD structural characterization of lanthanum-modified PbTiO$_3$ ceramic materials," *Journal of Physical Chemistry B*, vol. 108, no. 39, pp. 14840–14849, 2004.

[42] F. Farges, G. E. Brown, and J. J. Rehr, "Ti K-edge XANES studies of Ti coordination and disorder in oxide compounds: comparison between theory and experiment," *Physical Review B*, vol. 56, no. 4, pp. 1809–1819, 1997.

[43] R. V. Vedrinskii, V. L. Kraizman, A. A. Novakovich, P. V. Demekhin, and S. V. Urazhdin, "Pre-edge fine structure of the 3d atom K X-ray absorption spectra and quantitative atomic structure determinations for ferroelectric perovskite structure crystals," *Journal of Physics Condensed Matter*, vol. 10, no. 42, pp. 9561–9580, 1998.

[44] T. Yamamoto, T. Mizoguchi, and I. Tanaka, "Core-hole effect on dipolar and quadrupolar transitions of SrTiO$_3$ and BaTiO$_3$ at Ti K edge," *Physical Review B*, vol. 71, no. 24, Article ID 245113, 4 pages, 2005.

[45] T. Yamamoto, "Assignment of pre-edge peaks in K-edge X-ray absorption spectra of 3D transition metal compounds: electric dipole or quadrupole?" *X-ray Spectrom*, vol. 37, pp. 572–584, 2008.

Research Article

Optical Properties of ZnO-Alloyed Nanocrystalline Films

Hui Che,[1] Jesse Huso,[1] John L. Morrison,[1] Dinesh Thapa,[1] Michelle Huso,[1] Wei Jiang Yeh,[1] M. C. Tarun,[2] M. D. McCluskey,[2] and Leah Bergman[1]

[1] *Department of Physics, University of Idaho, Moscow, ID 83844-0903, USA*
[2] *Department of Physics and Materials Science, Washington State University, Pullman, WA 99164-2814, USA*

Correspondence should be addressed to Leah Bergman, lbergman@uidaho.edu

Received 27 November 2011; Revised 28 February 2012; Accepted 8 March 2012

Academic Editor: J. C. Sczancoski

ZnO is emerging as one of the materials of choice for UV applications. It has a deep excitonic energy level and a direct bandgap of ~3.4 eV. Alloying ZnO with certain atomic constituents adds new optical and electronic functionalities to ZnO. This paper presents research on $Mg_xZn_{1-x}O$ and $ZnS_{1-x}O_x$ nanocrystalline flexible films, which enable tunable optical properties in the deep-UV and in the visible range. The ZnO and $Mg_{0.3}Zn_{0.7}O$ films were found to have bandgaps at 3.35 and 4.02 eV, respectively. The photoluminescence of the $Mg_{0.3}Zn_{0.7}O$ exhibited a bandedge emission at 3.95 eV, and at lower energy 3.38 eV due to the limited solubility inherent to these alloys. $ZnS_{0.76}O_{0.24}$ and $ZnS_{0.16}O_{0.84}$ were found to have bandgaps at 3.21 and 2.65 eV, respectively. The effect of nitrogen doping on $ZnS_{0.16}O_{0.84}$ is discussed in terms of the highly lattice mismatched nature of these alloys and the resulting valence-band modification.

1. Introduction: The $Mg_xZn_{1-x}O$ and $ZnS_{1-x}O_x$ Alloy Systems

Zinc oxide (ZnO) is a direct bandgap semiconductor with a bandgap of ~3.37 eV at room temperature and relatively deep excitonic binding energy of 60 meV, both attributes of which make ZnO an efficient UV optical material at and above room temperature [1–6]. Due to their environmentally friendly chemical nature, resistivity to harsh environments, and deep excitonic level, ZnO as well as $Mg_xZn_{1-x}O$ (where x is the composition) are emerging materials capable of high-efficiency luminescence in a wide range of the ultraviolet (UV) spectrum [6–8].

ZnO has the hexagonal wurtzite structure, while MgO has the NaCl cubic structure with a direct bandgap ~7.5 eV and excitonic binding energy ~140 meV [9, 10]. Alloying these two provides a family of materials with tunable optical and electronic properties. Although the atomic sizes of Mg and Zn are comparable, that is, $Mg_xZn_{1-x}O$ is considered to be a lattice-matched system, due to the two different crystal structures the two oxides do not show complete solid solubility. Despite this inherent property, $Mg_xZn_{1-x}O$ alloys with tunable optical properties over a large composition range

have been realized [7, 8, 11, 12]. The exact properties were found to be somewhat growth dependant; the general trend of the bandgap behavior indicates that at Mg composition up to ~35% the alloy is soluble and has mainly the wurtzite structure with bandgap spanning the range of ~3.4–4 eV. At the composition range of ~35%–60% (referred to as the transition range), the alloy is phase separated into the wurtzite and the cubic structures, and at Mg composition above ~60% it has the cubic structure and bandgaps tuned in the range ~5–7 eV. Figure 1 presents a general schematic of the bandgap behavior of the $Mg_xZn_{1-x}O$ alloy system.

Another alloy system that may be proven to be very useful is $ZnS_{1-x}O_x$ that potentially should allow tuneability into the visible range. To date, very little is known about its material, electronic and optical properties [13]. ZnS with the zincblende structure has a direct bandgap ~3.84 eV [14]. The substituting anions in the $ZnS_{1-x}O_x$ alloy have large differences in size and chemical properties: the covalent radii of sulfur and oxygen are 1.02 Å and 0.73 Å, respectively, and their electronegative values are 2.58 and 3.44. This alloy is considered to be a highly lattice mismatched system. As a consequence, the $ZnS_{1-x}O_x$ alloy system has been predicted to have unusual material properties that should add new
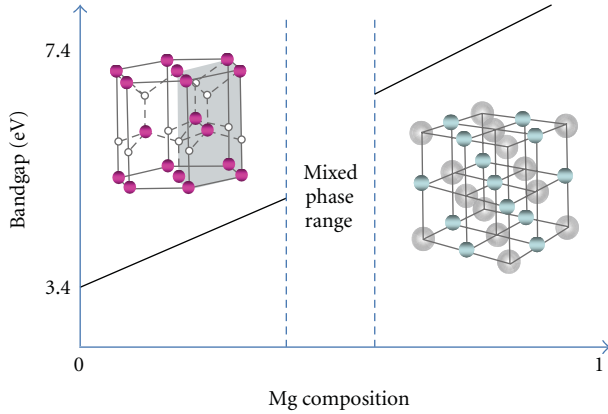
FIGURE 1: Diagram describing the behavior of the bandgap of $Mg_xZn_{1-x}O$ as a function of Mg composition.

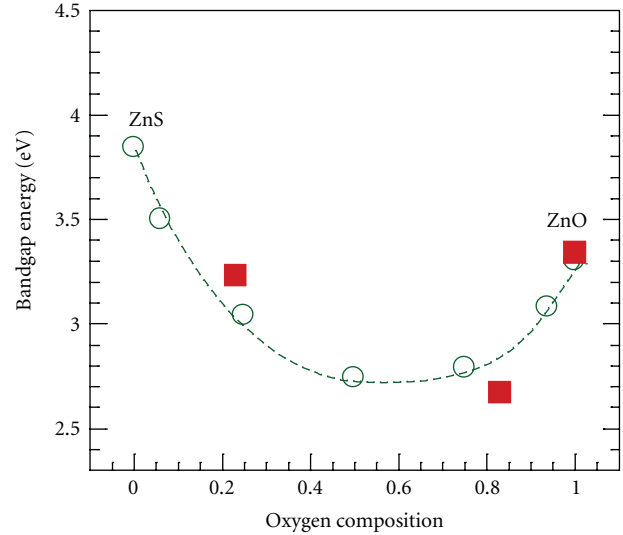
FIGURE 2: The bandgap energy of $ZnS_{1-x}O_x$ as a function of oxygen concentration. The theoretical prediction (circles) is from [14], and experimental results (squares) are from the research in this paper.

functionality to ZnO [14, 15]. First-principle plane-wave calculations by Moon et al. on highly mismatched II–VI alloys have predicted that these alloys possess huge bowing coefficients, that is, a significant deviation from linearity upon going from one end member of the alloy to the second [14]. Figure 2 presents the calculated bandgap of $ZnS_{1-x}O_x$ as a function of composition x [14]. In general terms, the cause of the large bowing parameter of these highly mismatched alloys has been attributed to hybridization and creation of resonance defect-like states at the gap edges. For example, at the low regime of sulfur concentration, the bowing into the visible is due to the raising of the valence band, while the conduction band is only slightly affected by the alloying [15]. Several groups reported similar unusual alloy properties of other highly mismatched systems such as $GaAs_xN_{1-x}$ and $GaN_{1-x}Bi_x$ [16–18]. In Figure 2, the square dots represent our experimental result that will be discussed in detail in the following sections. The advantages of having a highly lattice mismatched alloy is that for a relative small concentration of sulfur a significant modification of the bandgap can be attained that enables optical properties in the visible.

2. Experiment

The substrate used for the experiments is commercially available fluorinated ethylene propylene (FEP), also known as Teflon FEP, which is flexible and UV-transparent. The ZnO and the $Mg_{0.3}Zn_{0.7}O$ samples were grown at room temperature on prepared FEP substrates utilizing magnetron sputtering of Zn and Mg–Zn targets, respectively, under argon plasma. The samples were then oxidized for 2 hours under an atmosphere of 99.99% pure oxygen at a temperature of 275°C. The ZnS_xO_{1-x} films were grown by a reactive RF magnetron sputtering system, at 300°C, using a ceramic ZnS target and argon as the sputtering gas. In addition to the argon, controlled amounts of oxygen and nitrogen were introduced during the growth process so to achieve nitrogen-doped ZnS_xO_{1-x} films. The nitrogen pressure in the chamber was approximately 2.1×10^{-5} Torr. The films were sputtered

at 50 W for 1.5 hours. The nitrogen incorporation was verified by X-ray photoelectron spectroscopy (XPS). The compositions of the alloys were determined via energy dispersive spectroscopy (EDS).

The photoluminescence (PL) experiments utilized a JY-Horiba micro-Raman/PL system consisting of a high-resolution T-64000 triple monochromator and a UV confocal microscope capable of focusing to a spot size of ∼ $1 \mu m$ diameter. A CW-Kimmon laser with a wavelength of 325 nm (3.8 eV) and a Lexel Laser at 244 nm (5.1 eV) were used as the excitation source for the PL, and the cold temperature PL measurements were conducted in an INSTEC UV-compatible microcell. The subgap PL spectra were obtained, at room temperature, using a JY-Horiba FluoroLog-3 spectrofluorometer with a 450-W xenon lamp as the excitation source at 490 nm. The transmission spectra were acquired at room temperature using an Agilent Cary-300 system. The transmission data were acquired with a double-beam technique, and the data were normalized relative to the transparent region. Both procedures allow us to neglect equipment response as well as Fresnel reflections and scattering losses at the long wave length limit up to near the bandgap value.

3. Results and Discussion

Figures 3 and 4 present scanning electron microscope (SEM) images and photographs of the ZnO and $Mg_{0.3}Zn_{0.7}O$ flexible films [6], and Figure 5 presents those of the $ZnS_{0.16}O_{0.84}$. As is depicted in the figures, the morphology of the films is structured: in the nanoscale regime for ZnO and $Mg_{0.3}Zn_{0.7}O$ and at submicron regime for $ZnS_{0.16}O_{0.84}$. An extended discussion on the material properties of our flexible films can be found in [6]. In order to estimate the bandgaps of the alloys, transmission spectra were acquired at room
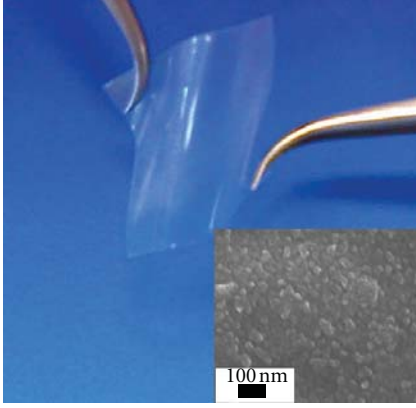
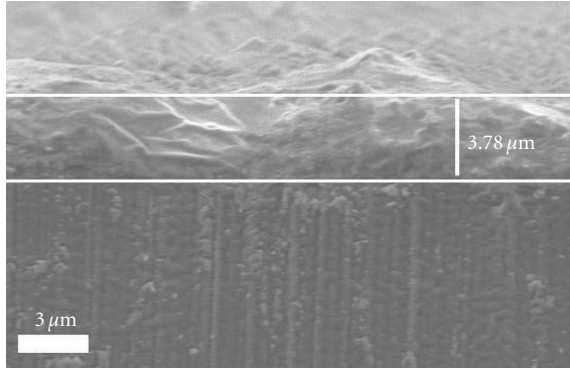FIGURE 3: A photograph and an SEM image (inset) of the ZnO nanocrystalline film.

FIGURE 4: A cross section SEM image of the $Mg_{0.3}Zn_{0.7}O$ films.

(a)

(b)

FIGURE 5: A photograph (a) and an SEM image (b) of the $ZnS_{0.16}O_{0.84}$ nanocrystalline film.

temperature and are presented in Figures 6(a) and 6(b). As can be seen in the figure, the alloys exhibit a rather broad absorption edge that is attributed to localized states due to the inherent alloy disorder and phase segregations. When the absorbance bandgap is not sharply defined, the usual method of extrapolation [20] may not render good results. To estimate the bandgap in such cases, transmission derivative procedures can be utilized, which were successfully used previously for the analysis of the bandgaps of $Mg_xZn_{1-x}O$ and $In_xGa_{1-x}N$ [6, 21–23]. In the following, we present the derivation of the method applicable to direct bandgap transitions.

The transmission through a film may be approximated as [20, 24]

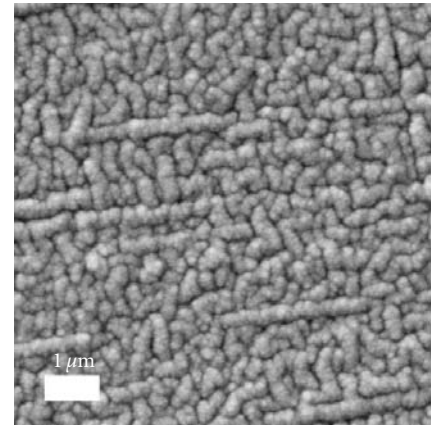$$T(E) \approx [1 - R(E)]^2 e^{-\alpha(E)t}, \tag{1}$$

where E is the energy of the incident light, R is the reflectance, and t is the thickness of the film. In (1), the absorption coefficient α may be written as [25]

$$\alpha(E) = \frac{C}{E\eta_r(E)}\sqrt{E - E_g}, \tag{2}$$

where $\eta_r(E)$ is the energy-dependent index of refraction and C is a constant. In obtaining the transmission derivative

one needs to consider the behavior of the reflectance near the bandgap energy. It can be shown that as $E \rightarrow E_g$, the quantities $1 - R(E)$ and $dR(E)/dE$ remain finite at energies in the vicinity of E_g due to the existence of a band tail which prevents a singularity-type behavior. Experimental results concerning ZnO thin film properties indeed found that the reflectance and its derivative are well-behaved quantities near the bandgap energy [26]. Consequently, for the purposes of our analysis we may write the transmission through a direct gap semiconductor as

$$T(E) = e^{-C^*(1/E\,\eta_r(E))\sqrt{E-E_g}}, \tag{3}$$

where $C^* = Ct$. The first derivative of $T(E)$ with respect to energy is then

$$\frac{dT}{dE} = -C^*\left[-\frac{1}{E^2\eta_r(E)}\sqrt{E - E_g} \right.$$

$$\left. -\frac{d\eta_r(E)}{dE}\frac{\sqrt{E - E_g}}{E(\eta_r(E))^2} + \frac{1}{2E\eta_r(E)\sqrt{E - E_g}} \right]$$

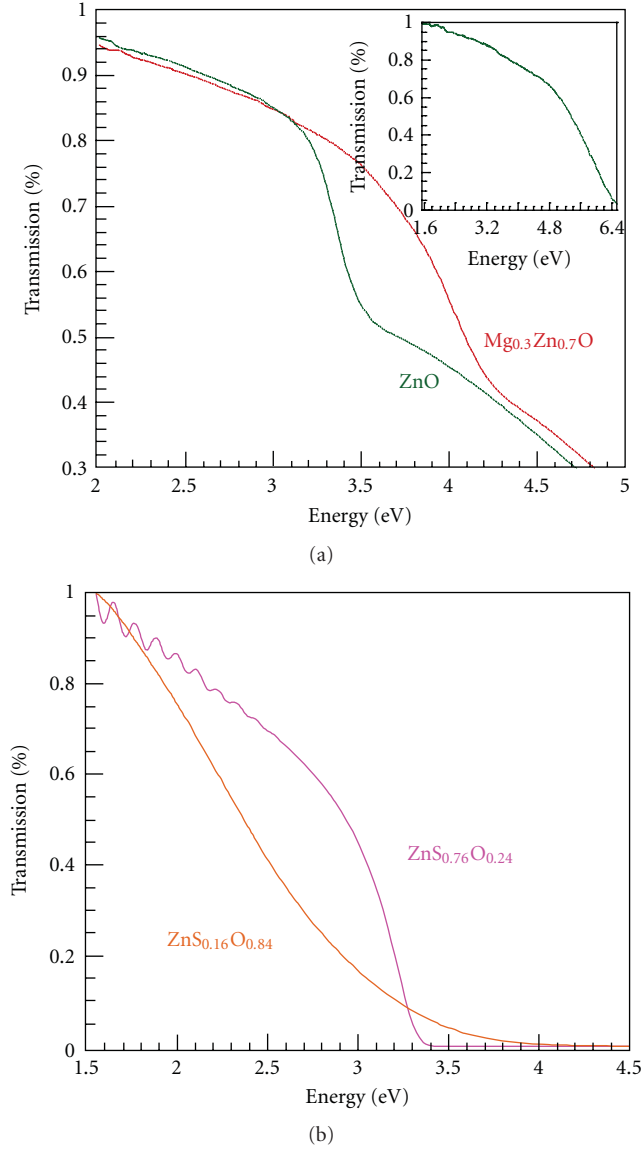$$\cdot \exp\left[-C^*\frac{1}{E\,\eta_r(E)}\sqrt{E - E_g} \right], \tag{4}$$

(a)

(b)

FIGURE 6: The transmission spectra of the ZnO and $Mg_{0.3}Zn_{0.7}O$ films (a) and those of the $ZnS_{0.76}O_{0.24}$ and $ZnS_{0.16}O_{0.84}$ (b). The inset in (a) is the transmission spectrum of the FEP substrate.

and at the limit $E \rightarrow E_g$, one gets

$$\lim_{E \rightarrow E_g} \frac{dT}{dE} = -1C^*\left(-0 - 0 + \frac{1}{0}\right) \longrightarrow -\infty, \quad (5)$$

which yields a spike towards negative infinity at $E = E_g$. It was assumed that $d\eta_r(E)/dE$ is continuous around E_g due to band tail states as was discussed in [27, 28]. Thus, a plot of dT/dE versus E will exhibit a strong singularity at the bandgap energy. In realistic cases, absorption tails exist, which soften the divergence and result in well-defined peaks around the gap energy, as also can be seen in Figure 7.

From Figure 7, the ZnO film has a bandgap of ~ 3.35 eV at room temperature, which is consistent with previous reports [29], while that of $Mg_{0.3}Zn_{0.7}O$ is at ~ 4.02 eV, a value similar to that previously observed for thin films grown
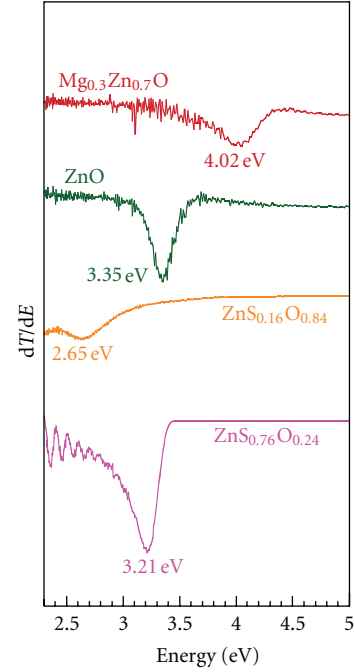

FIGURE 7: The plots of the derivative of the transmission with respect to energy.

via the pulsed laser deposition [7]. The bandgap of the $ZnS_{0.16}O_{0.84}$ and $ZnS_{0.76}O_{0.24}$ alloys are 2.65 and 3.21 eV, respectively, values which agree with those predicated from the first-principle plane-wave calculations presented in Figure 2 [14]. As such the transmission derivative method estimates well the bandgap of our materials.

The PL properties of the films presented in Figures 8 and 9 show that the $Mg_{0.3}Zn_{0.7}O$ film has two optical emissions: one at 3.38 and the other at a 3.95 eV. At Mg composition of $\sim 30\%$, the sample is expected to be phase segregate due to the limited solubility of the MgO–ZnO solid solution (see Figure 1). Accordingly, the peak emissions at 3.38 and at 3.95 eV are attributed to ZnO-rich and to MgO-rich domains, respectively. The $ZnS_{0.16}O_{0.84}$ film was found to luminesce at the visible range of 2.48 eV; however, the PL intensity was only visible at 77 K, and the PL of the $ZnS_{0.76}O_{0.24}$ was found to be extremely weak. The low efficiency of the PL may be a result of a significant concentration of structural defects due to the highly mismatched nature of this alloy system. As can be seen in Figure 5(b), the morphology of the sample is very coarse, unlike that of the MgZnO film presented in Figure 3. These structural defects may act as nonradiative centers impeding the PL efficiency.

Mapping of the bandgap via luminescence is a very informative technique for the study of deep impurities and defect centers in ZnO. ZnO has been found to have a characteristic broad In-gap PL with components in the green, yellow, and red part of the spectrum [30–32]. Although the origins of these PL are as yet under investigation, the consensus is that they are related to oxygen and zinc vacancies as well as to interstitial oxygen. In addition to those intrinsic centers,
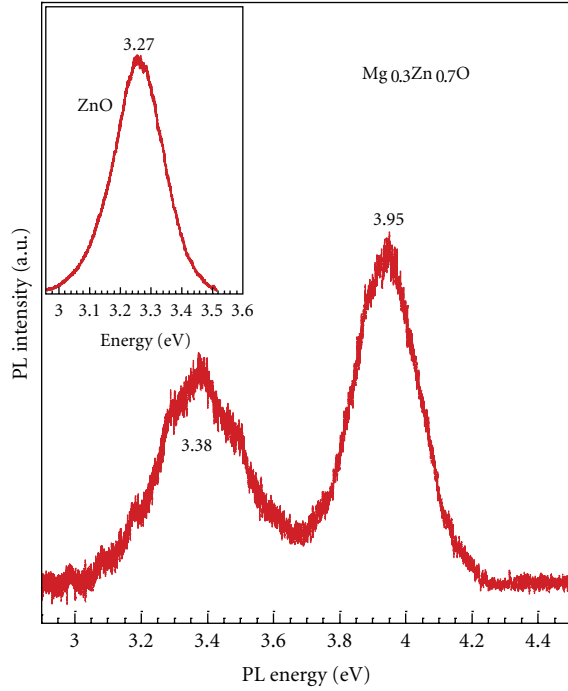
FIGURE 8: The room temperature PL spectrum of the $Mg_{0.3}Zn_{0.7}O$ sample. The inset is the spectrum of the ZnO sample.

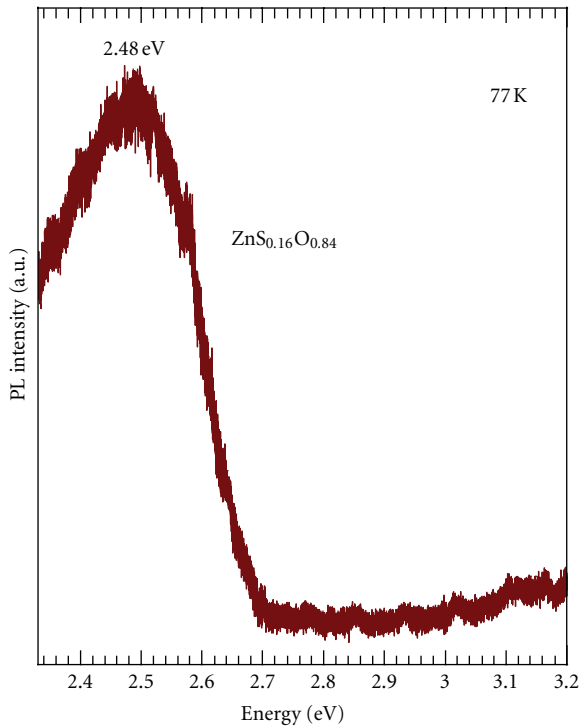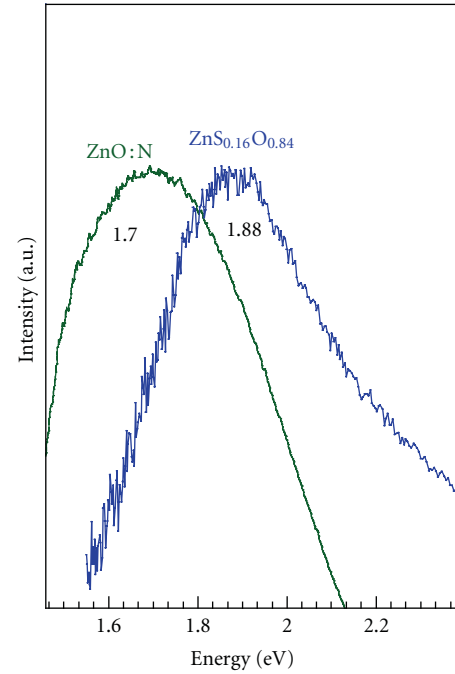FIGURE 10: The In-gap PL of a nitrogen-doped ZnO (from [19]) and that of nitrogen-doped $ZnS_{0.16}O_{0.84}$ film.

FIGURE 9: The PL spectrum of the $ZnS_{0.16}O_{0.84}$ sample. The PL was acquired at 77 K.

it was established that nitrogen doped ZnO also exhibits a broad in-gap PL at ~ 1.7 eV [19, 33]. Recent findings concerning the characteristics of nitrogen in ZnO found that nitrogen is a deep acceptor with acceptor level 1.3 eV above the valence band maximum [19, 34].

Unlike the deep level of nitrogen in ZnO, in $ZnS_{1-x}O_x$ the acceptor level was predicated to be relatively shallow for the low regime of sulfur concentration [15]. As was discussed in the introduction, this comes about due to the rising of the valence band toward the acceptor level upon alloying. The implication of the phenomenon is that p-type doping might be realized in lightly alloyed ZnO. Figure 10 presents the in-gap PL spectrum of nitrogen-doped ZnO taken from [19] and that of the $ZnS_{0.16}O_{0.84}$ film that exhibits a broad PL band at ~ 1.88 eV. The close proximity of the two peak positions and their similar linewidths suggest that that PL of the $ZnS_{0.16}O_{0.84}$ is due to nitrogen centers. Based on the in-gap PL emission, and the bandgap found for the $ZnS_{0.16}O_{0.84}$, a tentative bandgap diagram is presented in Figure 11 for which the nitrogen impurity has a level of ~ 0.37 eV above the valence band. In this diagram, it was assumed that the lattice coupling of the nitrogen center in $ZnS_{0.16}O_{0.84}$ is similar to that calculated for the same center in ZnO, that is, ~ 0.4 eV; for a smaller coupling, the nitrogen level should be a little higher and is at ~ 0.77 eV above the valence band in the limiting case of no coupling. For intermediate coupling energy ~ 0.22 eV, the nitrogen level will be at 0.55 eV, which is aligned with that of ZnO. Several factors may impact the observed in-gap PL energies, such as residual stress and structural defect-states, that might cause some discrepancy between the theory and experiments. Study of
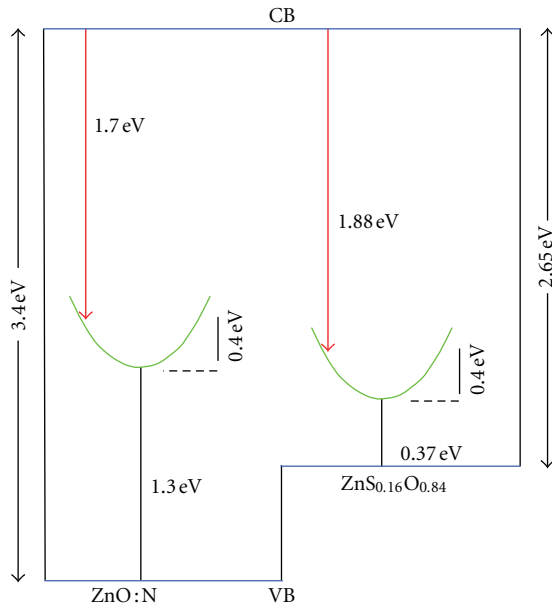
FIGURE 11: A schematic of bandgap diagram of the samples described in Figure 10.

nitrogen-doped ZnS films demonstrated that effective p-type conductivity can be readily attained, and a shallow nitrogen acceptor level about 0.19 eV above the valance band was suggested [35]. Thus, $ZnS_{1-x}O_x$ may have potential as a material component in ZnO-based devices when p-type doping is required.

4. Conclusions

$ZnS_{0.16}O_{0.84}$, $ZnS_{0.76}O_{0.24}$, ZnO, and $Mg_{0.3}Zn_{0.7}O$ nanocrystalline films were grown via a sputtering technique on a flexible substrate with the objective of achieving ZnO-based alloys with bandgaps spanning the visible to the UV. The bandgaps of the films were found to be 2.65, 3.21, 3.35, and 4.02 eV, respectively. The PL spectra of the $Mg_{0.3}Zn_{0.7}O$ exhibit a band-edge peak at 3.95 eV, and one at 3.38 eV that is attributed to a Zn-rich MgZnO segregates that arise from the inherent low solubility limit of this alloy system. The PL intensity of the $ZnS_{0.16}O_{0.84}$ and $ZnS_{0.76}O_{0.24}$ films was found to be extremely week. Structural defects, arising from the highly mismatched alloy constituents, were discussed to be the nonradiative optical centers. Future study will investigate whether the $ZnS_{1-x}O_x$ alloy system possesses an efficient PL. The $ZnS_{0.16}O_{0.84}$ was found to have an in-gap PL attributed to nitrogen centers, and a nitrogen energy level at the range $\sim$0.37–0.77 eV relative to the valence-band was proposed.

Acknowledgment

References

[1] Y. S. Park, C. W. Litton, T. C. Collins, and D. C. Reynolds, "Exciton spectrum of ZnO," *Physical Review*, vol. 143, no. 2, pp. 512–519, 1966.

[2] W. Y. Liang and A. D. Yoffe, "Transmission spectra of ZnO single crystals," *Physical Review Letters*, vol. 20, no. 2, pp. 59–62, 1968.

[3] R. Laskowski and N. E. Christensen, "Ab initio calculation of excitons in ZnO," *Physical Review B*, vol. 73, no. 4, Article ID 045201, 7 pages, 2006.

[4] B. K. Meyer, H. Alves, D. M. Hofmann et al., "Bound exciton and donor-acceptor pair recombinations in ZnO," *Physica Status Solidi*, vol. 241, no. 2, pp. 231–260, 2004.

[5] X.-B. Chen, J. Huso, J. L. Morrison, and L. Bergman, "The properties of ZnO photoluminescence at and above room temperature," *Journal of Applied Physics*, vol. 102, no. 11, Article ID 116105, 2007.

[6] J. Huso, J. L. Morrison, H. Che et al., "ZnO and MgZnO nanocrystalline flexible films: optical and material properties," *Journal of Nanomaterials*, vol. 2011, Article ID 691582, 7 pages, 2011.

[7] A. Ohtomo, M. Kawasaki, T. Koida et al., "$Mg_xZn_{1-x}O$ as a II-VI widegap semiconductor alloy," *Applied Physics Letters*, vol. 72, no. 19, pp. 2466–2468, 1998.

[8] S. Choopun, R. D. Vispute, W. Yang, R. P. Sharma, T. Venkatesan, and H. Shen, "Realization of band gap above 5.0 eV in metastable cubic-phase $Mg_xZn_{1-x}O$ alloy films," *Applied Physics Letters*, vol. 80, no. 9, pp. 1529–1531, 2002.

[9] R. C. Whited, C. J. Flaten, and W. C. Walker, "Exciton thermoreflectance of MgO and CaO," *Solid State Communications*, vol. 13, no. 11, pp. 1903–1905, 1973.

[10] P. D. Johnson, "Some optical properties of MgO in the vacuum ultraviolet," *Physical Review*, vol. 94, no. 4, pp. 845–846, 1954.

[11] U. Sahaym, M. G. Norton, J. Huso, J. L. Morrison, H. Che, and L Bergman, "Microstructure evolution and photoluminescence in nanocrystalline $Mg_xZn_{1-x}O$ thin films," *Nanotechnology*, vol. 22, no. 42, Article ID 425706, 2011.

[12] X. Du, Z. Mei, Z. Liu et al., "Controlled growth of high-quality ZnO-based films and fabrication of visible-blind and solar-blind ultra-violet detectors," *Advanced Materials*, vol. 21, no. 45, pp. 4625–4630, 2009.

[13] B. K. Meyer, A. Polity, B. Farangis et al., "Structural properties and bandgap bowing of $ZnO_{1-x}S_x$ thin films deposited by reactive sputtering," *Applied Physics Letters*, vol. 85, no. 21, pp. 4929–4931, 2004.

[14] C.-Y. Moon, S.-H. Wei, Y. Z. Zhu, and G. D. Chen, "Band-gap bowing coefficients in large size-mismatched II-VI alloys: first-principles calculations," *Physical Review B*, vol. 74, Article ID 233202, 4 pages, 2006.

[15] C. Persson, C. Platzer-Björkman, J. Malmström, T. Törndahl, and M. Edoff, "Strong valence-band offset bowing of $ZnO_{1-x}S_x$ enhances p-type nitrogen doping of ZnO-like alloys," *Physical Review Letters*, vol. 97, no. 14, Article ID 146403, 2006.

[16] J. Wu, W. Walukiewicz, and E. E. Haller, "Band structure of highly mismatched semiconductor alloys: coherent potential approximation," *Physical Review B*, vol. 65, no. 23, Article ID 233210, 4 pages, 2002.

[17] K. M. Yu, W. Walukiewicz, W. Shan et al., "Synthesis and optical properties of II-O-VI highly mismatched alloys," *Journal of Applied Physics*, vol. 95, no. 11 I, pp. 6232–6238, 2004.

[18] A. X. Levander, K. M. Yu, S. V. Novikov et al., "Gan1-xbix: extremely mismatched semiconductor alloys," *Applied Physics Letters*, vol. 97, no. 14, Article ID 141919, 2010.

[19] M. C. Tarun, M. Z. Iqbal, and M. D. McCluskey, "Nitrogen is a deep acceptor in ZnO," *AIP Advances*, vol. 1, no. 2, Article ID 022105, 7 pages, 2011.

[20] J. I. Pankove, *Optical Processes in Semiconductors*, Dover, New York, NY, USA, 1971.

[21] M. Wang, E. J. Kim, S. Kim et al., "Optical and structural properties of sol—gel prepared MgZnO alloy thin films," *Thin Solid Films*, vol. 516, no. 6, pp. 1124–1129, 2008.

[22] R. Viswanatha, S. Chakraborty, S. Basu, and D. D. Sarma, "Blue-emitting copper-doped zinc oxide nanocrystals," *Journal of Physical Chemistry B*, vol. 110, no. 45, pp. 22310–22312, 2006.

[23] C. A. Parker, J. C. Roberts, S. M. Bedair et al., "Optical band gap dependence on composition and thickness of $In_xGa_{1-x}N$ (0<x<0.25) grown on gan," *Applied Physics Letters*, vol. 75, no. 17, pp. 2566–2568, 1999.

[24] B. Ullrich, C. Zhang, E. F. Schubert, J. E. Cunningham, and K. V. Klitzing, "Transmission spectroscopy on sawtooth-doping superlattices," *Physical Review B*, vol. 39, no. 6, pp. 3776–3779, 1989.

[25] B. K. Ridley, *Quantum Processes in Semiconductors*, Clarendon Press, Oxford University Press, New York, NY, USA, 1999.

[26] R. E. Marotti, D. N. Guerra, C. Bello, G. Machado, and E. A. Dalchiele, "Bandgap energy tuning of electrochemically grown ZnO thin films by thickness and electrodeposition potential," *Solar Energy Materials and Solar Cells*, vol. 82, no. 1-2, pp. 85–103, 2004.

[27] F. Stern, "Dispersion of the index of refraction near the absorption edge of semiconductors," *Physical Review*, vol. 133, no. 6A, pp. A1653–A1664, 1964.

[28] C. Tanguy, "Refractive index of direct bandgap semiconductors near the absorption threshold: influence of excitonic effects," *IEEE Journal of Quantum Electronics*, vol. 32, no. 10, pp. 1746–1751, 1996.

[29] V. Srikant and D. R. Clarke, "On the optical band gap of zinc oxide," *Journal of Applied Physics*, vol. 83, no. 10, pp. 5447–5451, 1998.

[30] D. Li, Y. H. Leung, A. B. Djurišić et al., "Different origins of visible luminescence in ZnO nanostructures fabricated by the chemical and evaporation methods," *Applied Physics Letters*, vol. 85, no. 9, pp. 1601–1603, 2004.

[31] Y. W. Heo, D. P. Norton, and S. J. Pearton, "Origin of green luminescence in ZnO thin film grown by molecular-beam epitaxy," *Journal of Applied Physics*, vol. 98, no. 7, Article ID 073502, 6 pages, 2005.

[32] A. B. Djurišić, Y. H. Leung, K. H. Tam et al., "Green, yellow, and orange defect emission from ZnO nanostructures: Influence of excitation wavelength," *Applied Physics Letters*, vol. 88, no. 10, Article ID 103107, 3 pages, 2006.

[33] R. Huang, S. Xu, W. Guo et al., "Nitrogen deep acceptors in ZnO nanowires induced by ammonia plasma ," *Applied Physics Letters*, vol. 99, no. 14, Article ID 143112, 3 pages, 2011.

[34] L. Lyons, A. Janotti, and C. G. Van de Walle, "Why nitrogen cannot lead to p-type conductivity in ZnO," *Applied Physics Letters*, vol. 95, no. 25, Article ID 252105, 3 pages, 2009.

[35] L. Svob, C. Thiandoume, A. Lusson, M. Bouanani, Y. Marfaing, and O. Gorochov, "P-type doping with n and li acceptors of zns grown by metalorganic vapor phase epitaxy," *Applied Physics Letters*, vol. 76, no. 13, pp. 1695–1697, 2000.

Research Article

Synthesis and Electroluminescent Properties of Bis(3H-1,2,3-triazolo-[4,5-b]pyridine-3-ol)zinc Zn(TAP)$_2$

Trinh Dac Hoanh,[1] Young Hoon Im,[1] Dong-Eun Kim,[2] Young-Soo Kwon,[2] and Burm-Jong Lee[1]

[1] *Department of Chemistry and Institute of Basic Sciences, Inje University, Gimhae 621-749, Republic of Korea*
[2] *Department of Electrical Engineering and NTRC, Dong-A University, Busan 604-714, Republic of Korea*

Correspondence should be addressed to Burm-Jong Lee, chemlbj@inje.ac.kr

A new light-emissive material, bis(3H-1,2,3-triazolo-[4,5-b]pyridine-3-ol)zinc (Zn(TAP)$_2$), has been synthesized and characterized by FT-NMR, FT-IR, UV-Vis, and elemental analysis. The photoluminescence (PL) of Zn(TAP)$_2$ was measured from the DMF solution at 460 nm. The HOMO (6.5 eV) and LUMO (2.8 eV) energy levels of Zn(TAP)$_2$ were estimated from the measurement of cyclic voltammetry. The devices with structures of ITO/NPB/Zn(TAP)$_2$/LiF/Al and ITO/NPB/Zn(TAP)$_2$/Alq$_3$/LiF/Al were constructed to investigate their electroluminescent (EL) performance. Zn (TAP)$_2$ is supposed to be a good emitting material in the EL device.

1. Introduction

Organic light-emitting diodes (OLEDs) are believed to be the next-generation flat panel displays due to low driving voltage, high contrast, ease of fabrication, wide viewing angle, and low cost [1–5]. Even now they have already become cheaper than their inorganic counterparts. In this field, the development of novel luminescent organic/organometallic compounds is a key to enhance the performance of organic and polymeric light-emitting devices. Luminescent chelate complexes have shown to be particularly useful in OLEDs because of their relatively high stability and volatility. Alq$_3$ is the most well-known example of such chelate compounds, where q is the 8-hydroxyquinolinato ligand, which is both a good emitter and a highly efficient electron-transporting material [6, 7].

Since the first OLEDs with Zn complexes were reported in 1993 [8], synthesis of novel zinc complexes as active materials for OLEDs have focused on improving electron mobility or producing a blue shift emission compared to Znq$_2$ [9, 10]. The electroluminescent performance of zinc complexes as the emitter is just comparable with that of Alq$_3$ [11]. However, in many instances, the electron-transporting mobility of zinc complexes goes beyond that of Alq$_3$ [12]. So zinc complexes may be potential candidates to enhance the electron-transporting properties for OLEDs.

Zn^{2+} ion is the only oxidation state of zinc atom and has no unoccupied valence electron orbits. Therefore, the oxidation and reduction of zinc complexes are mainly carried out in the ligands, that is, luminescence and charge transporting may be ascribed to intraligand electronic transition. One simple way to adjust the emission wavelength is to manipulate substituents in the 8-hydroxyquinoline rings or to modify the chemical structure. C2 position-substituted bis(2-methyl-8-hydroxyquinoline)zinc (ZnMq$_2$) [13], C5 position-substituted bis(8-hydroxy-5-piperidin-ylsulfonamidoquinolate)zinc (Zn(QS)$_2$) [14] and (ZnLn)$_2 \cdot$ 2H$_2$O (Ln = 5-amido-substituted-8-hydroxyquinolinate ligand) [11] have been reported one after the other. These complexes showed more or less either blue-shifting or red-shifting with reference to Znq$_2$. In our previous reports, [2-(2-hydroxyphenyl)benzoxazole]zinc [15] Zn(HPB)$_2$ and

FIGURE 1: Synthetic scheme of Zn(TAP)₂.
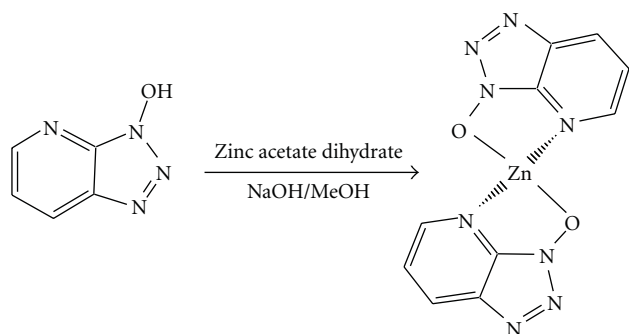
zinc [16] Zn(MHB)₂ have shown to be good materials for OLEDs as hole blocking layer and emitting layer.

In this paper, (3H-1,2,3-triazolo-[4,5-b]pyridine-3-ol) zinc Zn(TAP)₂ was synthesized and primarily applied as an emitting layer (EML) based on its energy gap level of 3.7 eV. Two types of OLEDs devices with the structures of ITO/NPB(40 nm)/Zn(TAP)₂(60 nm)/ Alq₃ (5 nm)/LiF/A1 and ITO/NPB(40 nm)/Zn(TAP)₂(60 nm)/LiF/A1 are fabricated by considering the balance of carriers injection and transportation as well as the matching of the energy level. The photoluminescent (PL) and EL properties of Zn(TAP)₂ were investigated.

2. Experimental Details

2.1. Materials and Characterization Equipments. 3H-1,2,3-triazolo-[4,5-b]pyridine-3-ol (>98%) and sodium hydroxide were purchased from TCI, and Zinc acetate dehydrate (>99%) was purchased from Fluka and used without further purification unless otherwise noted. Solvents were purified by normal procedures and handled under moisture-free atmosphere. The optical absorption spectra were measured by a Shimadzu UV-2501 PC Spectrometer. The PL spectrum was measured using a Perkin-Elmer LS45 luminescence spectrometer. The characteristics of the current density-voltage-luminance (I-V-L) and the efficiency were measured by IVL 300 series (JBS Inc.).
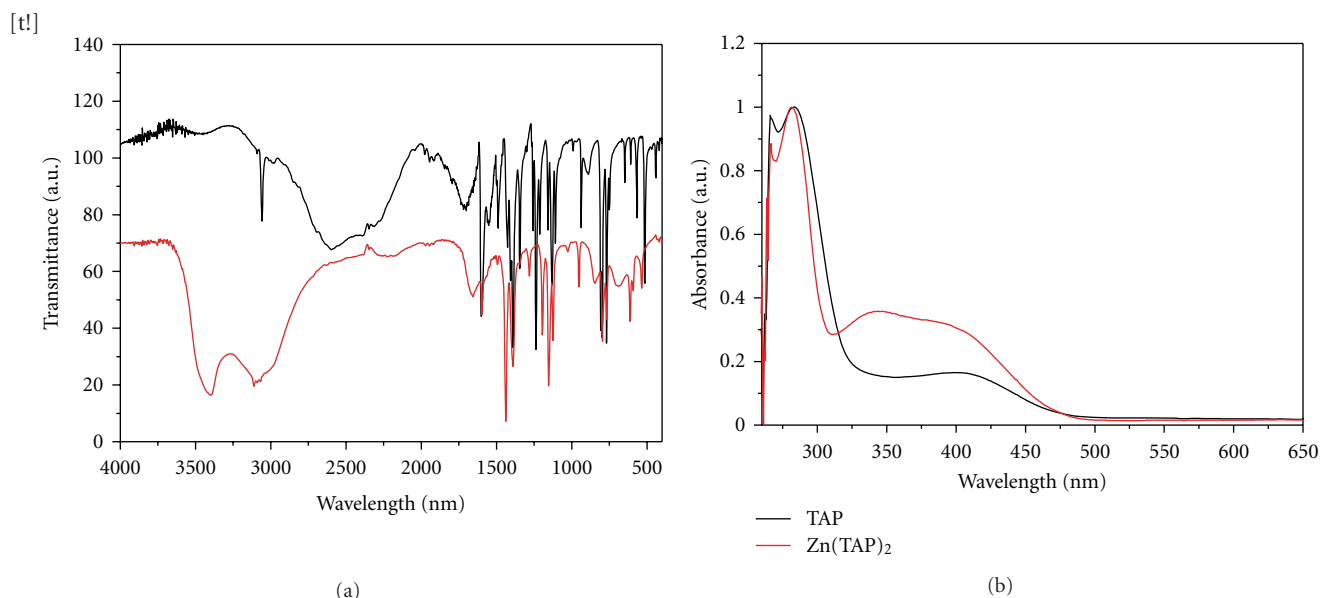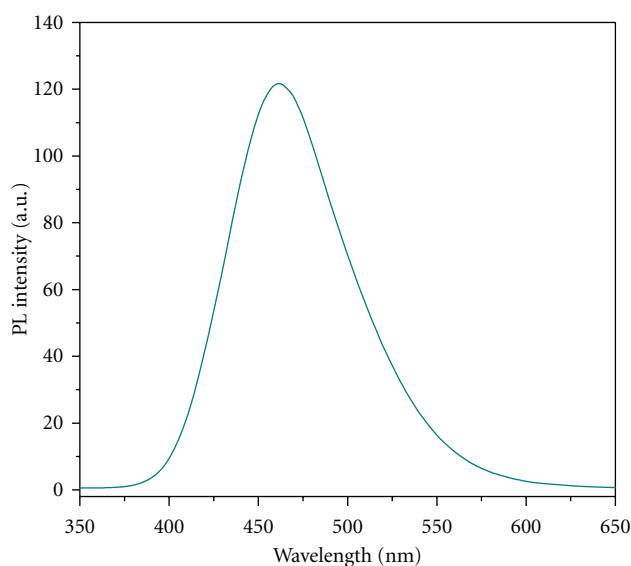
2.2. Synthesis of [3H-1,2,3-triazolo-[4,5-b]pyridine-3-ol]zinc Zn(TAP)₂. The synthetic scheme of Zn(TAP)₂ is shown in Figure 1. The synthesis of Zn(TAP)₂ was followed the closely related literature procedure and our previous works [15–18]. First, a solution of zinc acetate dihydrate (0.211 g, 1 mmol) in methanol (5 mL) was gradually added to a DMF solution of 3H-1,2,3-triazolo-[4,5-b]pyridine-3-ol (TAP) (0.27 g, 2 mmol) and sodium hydroxide (0.08 g, 2 mmol) in 5 mL methanol. After the mixture was stirred for 8 h at room temperature under N₂, a yellow precipitate was produced. The yellow precipitates were collected by filtration and purified by recrystallization from DMF and water and dried under vacuum. Anal. Calc. for $C_{10}H_6N_8O_2Zn$, C: 35.79, H: 1.80, N: 33.39. Found (%) C: 35.02, H: 1.82, N: 33.41. ¹H-NMR (300 MHz, [D₆] DMSO, ppm) δ 8.25 (2H), 8.20 (2H),

7.22 (2H). ¹³C-NMR (75 MHz, [D₆] DMSO, ppm) δ 146.06, 137.85, 134.25, 128.56, 119.90. FT-IR (KBr, cm⁻¹): 3402, 3166, 2305, 1657, 1597, 1394, 1153, 801. UV-Vis (nm, in DMF): 206, 282, 342, 406. (Reference UV-Vis (TAP): 265, 283, 406.).

2.3. Fabrication of EL Devices. The OLEDs containing Zn(TAP)₂ were fabricated by the vacuum deposition. The substrate was ITO-coated glass with a sheet resistance of 10Ω per square. The ITO-coated glass was pretreated according to a regular chemical cleaning procedure using detergent, deionized water and alcohol in sequence, and finished with UV-ozone method. The thermal evaporation of organic materials was carried out at a chamber pressure of 5 × 10⁻⁶ torr. The emission area of each device was 3 × 3 mm². All the organics were evaporated with a rate in the range of 0.1–0.3 nm/s. The metallic cathode was evaporated at higher rate (0.8–1 nm/s) with keeping the vacuum level.

3. Results and Discussion

3.1. Structure Characterization and PL Properties of Zn(TAP)₂. The chemical structure of the zinc complex was determined from FT-IR, UV-Vis, and ¹H-NMR and ¹³C-NMR. The FT-IR spectrum of Zn(TAP)₂ is shown in Figure 2(a). The high-frequency region (3300–3000 cm⁻¹) contains absorption bands originating mainly from localized C–H stretching vibrations, although the broad band around 3500 cm⁻¹ is still shown due to the hydration. The mid-frequency region (1700–1000 cm⁻¹) corresponds to in-plane stretching and bending of heavy atom vibrations. In the low-frequency region (below 1000 cm⁻¹), the out-of-plane modes are observed. The bands centered at 1657 and 1597 cm⁻¹ are assigned to the C=C stretching vibration involving the TAP ligand. The bands observed at 1496 and 1476 cm⁻¹ should correspond to a C=C/C=N stretching associated with the TAP mobility in Zn(TAP)₂. The absorption band at about 1100 cm⁻¹ should be assigned to the C–O stretching vibration frequency at the C–O–M site. The spectrum showed a sharp absorption band at about 1153 cm⁻¹. However, the absorption bands by Zn–O or Zn–N were not detected in the lower frequency region. During handling the complex sample, it showed a blue emission in DMF solution under the UV-lamp (exciting wavelength, 365 nm). The UV-vis absorption and photoluminescence (PL) spectra of the Zn(TAP)₂ are, respectively, shown in Figures 2(b) and 3. The UV-vis absorption and PL spectra were measured in the DMF solution. The absorption spectrum of the Zn(TAP)₂ exhibited the peaks at around 265, 282, 342, and 406 nm, which are attributed to π-π* transition of 3H-1,2,3-triazolo-[4,5-b]pyridine-3-ol ligand and the metal complex. The PL spectrum of Zn(TAP)₂ exhibits a maximum at around 460 nm (exciting wavelength, 350 nm). Figure 4(a) shows the ¹H-NMR spectrum of 3H-1,2,3-triazolo-[4,5-b]pyridine-3-ol with chemical shifts (δ) of 7.5 (1H), 8.5 (1H), and 8.7 (1H) ppm, which belong to the aromatic protons, and 13.8 ppm by the OH group. The ¹H-NMR spectrum of the Zn-complex (Figure 4(b)) agrees

[t!]

(a)

(b)

FIGURE 2: (a) FT-IR and (b) UV-vis spectra of Zn(TAP)$_2$.

FIGURE 3: Photoluminescence of Zn(TAP)$_2$.

with the moiety of 3H-1,2,3-triazolo-[4,5-b]pyridine-3-ol in Figure 4(a) with blue shift. It shows the peaks (δ) of 8.25 (2H), 8.20 (2H), and 7.22 (2H) ppm by the aromatic protons and the peak by the OH group disappears along with the complex formation. The ^{13}C-NMR spectrum (Figure 4(c)) also supports the chemical structure from five ^{1}H-decoupled ^{13}C-peaks (δ 146.06, 137.85, 134.25, 128.56, and 119.90) due to the aromatic ring.

3.2. Electrochemical Properties of Zn(TAP)$_2$. The energy band diagrams of the Zn(TAP)$_2$ were determined from the HOMO and LUMO energy levels and the band gaps, which were calculated from cyclic voltammetry (C-V) [19].

The C-V measurement was performed with a solution of tetrabutylammonium tetrafluoroborate (Bu$_4$NBF$_4$) (0.10 M) in acetonitrile at a scan rate of 400 mV/s at room temperature under the protection of argon. A Pt wire and an Ag/AgCl electrode were used as the counter electrode and reference electrode, respectively. From the onset potential for the oxidation, the HOMO energy level of the Zn(TAP)$_2$ was estimated by considering the energy level of the reference ferrocene/ferrocenium (Fc/Fc+) redox couple [20]. The oxidation onset potential of Zn(TAP)$_2$ was +1.7 V, and the reduction onset potential was found to be -2.0 V as shown in Figure 5. From these onset potentials of the oxidation and the reduction of cyclic voltammograms, the HOMO and LUMO energy were calculated as 6.5 and 2.8 eV, respectively, with an
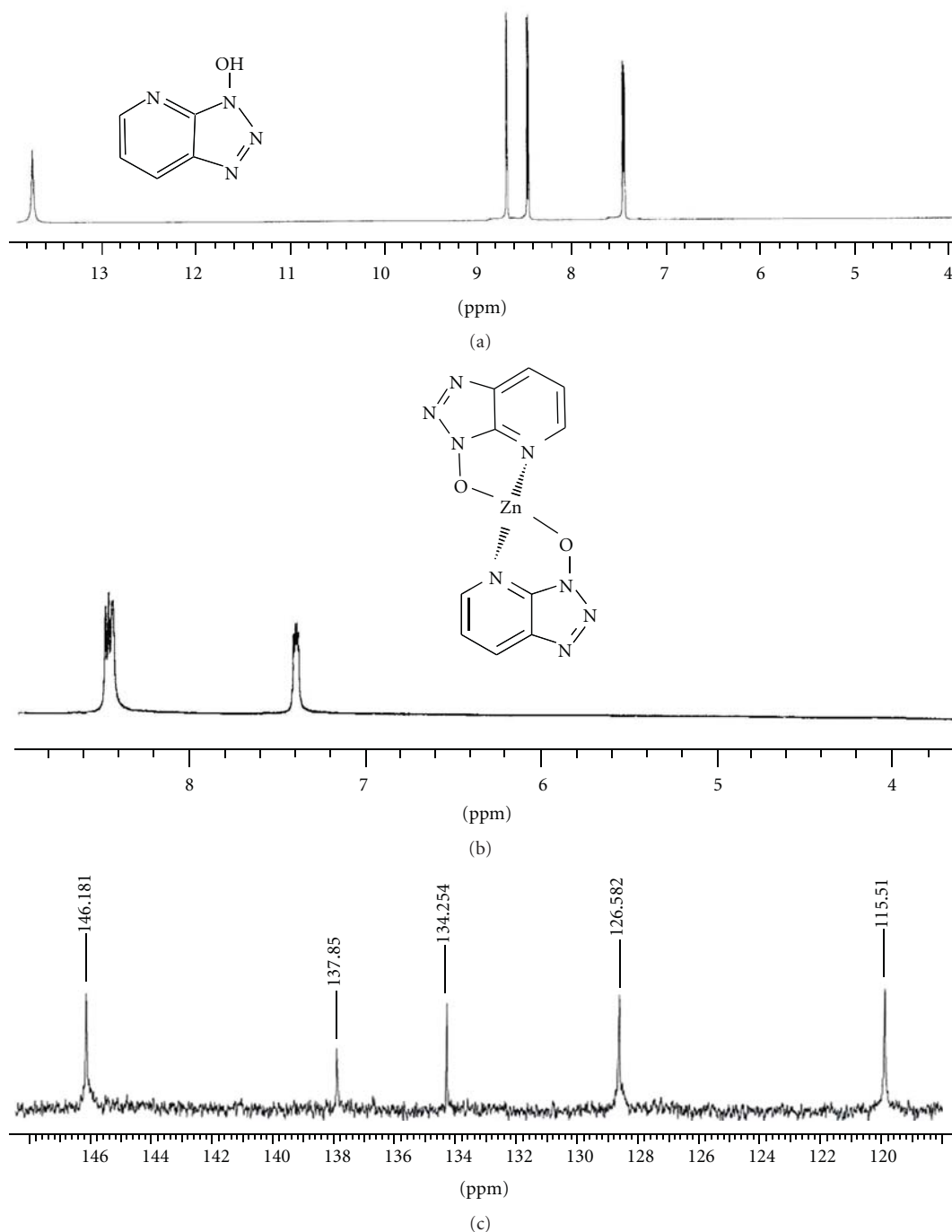
(a)

(b)

(c)

FIGURE 4: ^{1}H-NMR spectra of (a) TAP and (b) Zn (TAP)$_2$ and (c) ^{13}C- NMR spectrum of Zn (TAP)$_2$.

Eg of 3.7 eV. Figure 6 shows the work functions of electrodes and HOMO and LUMO energy levels of the materials for ITO/NPB/Zn(TAP)$_2$/Alq$_3$/LiF/Al device. It illustrates the possible combination of electrons and holes in the Zn(TAP)$_2$ layer.

3.3. Electroluminescence Properties. The normalized electroluminescence (EL) spectrum is shown in Figure 7(a). To

investigate the EL properties of the Zn(TAP)$_2$, devices with the configuration of ITO/NPB/Zn(TAP)$_2$/Alq$_3$/LiF/Al and ITO/NPB/Zn(TAP)$_2$/LiF/Al were fabricated. And to decrease the operating voltage and to achieve the best OLEDs performance of the devices, we optimized the thicknesses of emitting layer. The EL spectrum of the device shows maximum emission at the λ_{max} = 448 nm, considerably blue-shifted compared to the PL spectrum.
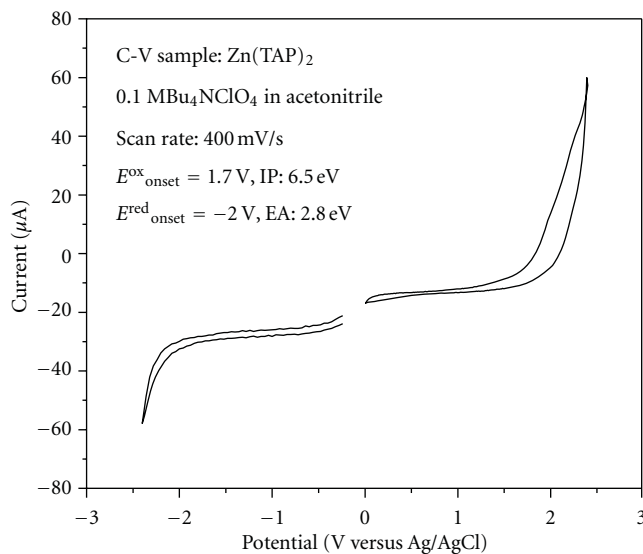
FIGURE 5: Cyclic voltammogram of $Zn(TAP)_2$.
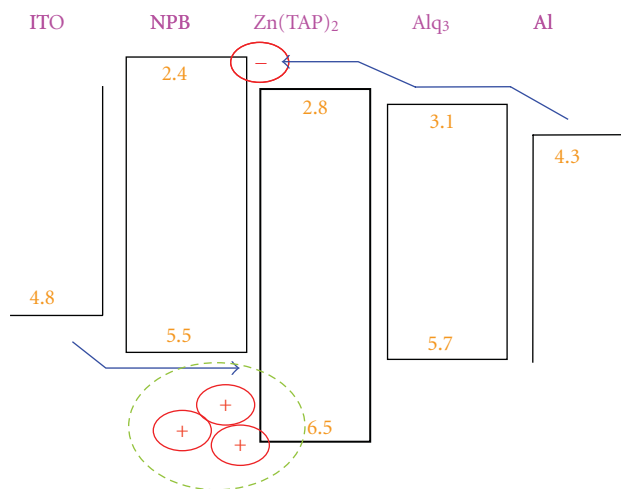
FIGURE 6: Work functions of electrodes and HOMO and LUMO energy levels of the materials for ITO/NPB/$Zn(TAP)_2$/Alq_3/LiF/Al device.

The current density-voltage-luminance (I-V-L) and current density-efficiency characteristics of the device are shown in Figures 7(b), 7(c), and 7(d). The device showed a turn-on voltage as low as 5 V. For the ITO/NPB(40 nm)/ $Zn(TAP)_2$(60 nm)/Alq_3(5 nm)/LiF/Al device driven at a current density of 2,100 mA/cm^2, the maximum luminance of 2,800 cd/m^2 was achieved with an efficiency of 1.85 lm/W. In addition, we constructed another device without Alq_3 as ITO/NPB(40 nm)/$Zn(TAP)_2$(60 nm)/LiF/Al to compare the component performance. In this case, at the current density of 1,500 mA/cm^2, the maximum luminance of 1,800 cd/m^2 was achieved with an efficiency of 1.25 lm/V. Therefore, the performance by the first device was better than the later one. It means that the Alq_3 with the thickness of 5 nm played as the electrons transport layer (ETL), which increased the combination of electrons with the holes in the emitting layer of $Zn(TAP)_2$. We expect that the EL performance could be further improved by introducing other buffer layers or applying the zinc complex to electron balancing layer.

4. Conclusion

We synthesized a novel blue emitting material, [3H-1,2,3-triazolo-[4,5-b]pyridine-3-ol]zinc $Zn(TAP)_2$). In DMF solution, $Zn(TAP)_2$ showed strong blue photoluminescence around 460 nm and the EL device showed blue emission at λ_{max} of 448 nm. The blue emitting device using $Zn(TAP)_2$ as emitting material showed the luminance of 2,800 cd/m^2 at 12 V. The preliminary electrical characteristics of $Zn(TAP)_2$
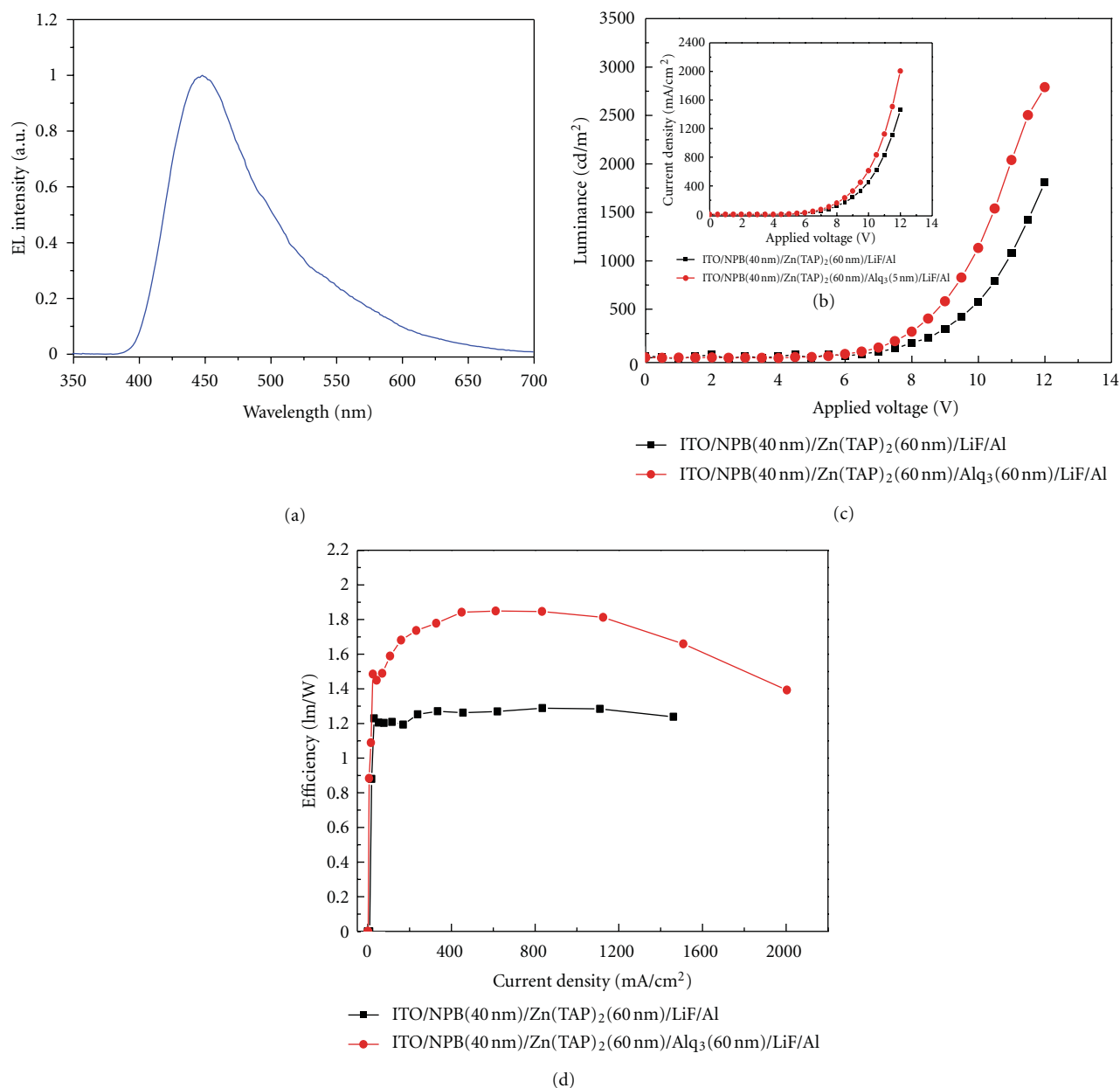
(a)

(c)

(d)

FIGURE 7: (a) EL spectra of OLEDs devices using Zn(TAP)$_2$ as emitting layer, (b) current density versus applied voltage, (c) luminance versus applied voltage, and (d) efficiency versus applied voltage characteristics of OLEDs devices.

suggest that its related compounds can be possible candidates for the OLEDs materials.

References

[1] C. W. Tang and S. A. Vanslyke, "Organic electroluminescent diodes," *Applied Physics Letters*, vol. 51, no. 12, pp. 913–915, 1987.

[2] C. Adachi, S. Tokito, T. Tsutsui, and S. Saito, "Organic electroluminescent device with a three-layer structure," *Japanese Journal of Applied Physics*, vol. 27, no. 4, pp. 713–715, 1988.

[3] J. H. Burroughes, D. D. C. Bradley, A. R. Brown et al., "Light-emitting diodes based on conjugated polymers," *Nature*, vol. 347, no. 6293, pp. 539–541, 1990.

[4] J. R. Sheats, H. Antoniadis, M. Hueschen et al., "Organic electroluminescent devices," *Science*, vol. 273, no. 5277, pp. 884–888, 1996.

[5] H. Nakada and T. Tohma, *Inorganic and Organic Electroluminescence*, Wissenschaft-und-Technik-Verlag, Berlin, Germany, 1996.

[6] S. F. Liu, C. Seward, H. Aziz, N. X. Hu, Z. Popović, and S. Wang, "Syntheses, structures, and luminescence/electroluminescence of bph2(mqp), al(ch3)(mqp)2, and

al(mqp)3 (mqp = 2-(4′-methylquinolinyl)-2-phenolato),” *Organometallics*, vol. 19, no. 26, pp. 5709–5714, 2000.

[7] A. Curioni, W. Andreoni, R. Treusch et al., “Atom-resolved electronic spectra for Alq$_3$ from theory and experiment,” *Applied Physics Letters*, vol. 72, no. 13, pp. 1575–1577, 1998.

[8] Y. Hamada, T. Sano, M. Fujita, T. Fujii, Y. Nishio, and K. Shibata, “Organic electroluminescent devices with 8-hydroxyquinoline derivative-metal complexes as an emitter,” *Japanese Journal of Applied Physics, Part 2: Letters*, vol. 32, no. 4 A, pp. L514–L515, 1993.

[9] A. Kraft, A. C. Grimsdale, and A. B. Holmes, “Electroluminescent conjugated polymers—seeing polymers in a new light,” *Angewandte Chemie*, vol. 37, no. 4, pp. 402–428, 1998.

[10] M. T. Bernius, M. O’Brien, J. Inbasekaran, and W. Wu, “Progress with light-emitting polymers,” *Advanced Materials*, vol. 12, no. 23, pp. 1737–1750, 2000.

[11] S. Tokito, K. Noda, H. Tanaka, Y. Taga, and T. Tsutsui, “Organic light-emitting diodes using novel metal-chelate complexes,” *Synthetic Metals*, vol. 111, pp. 393–396, 2000.

[12] J. W. Park, G. C. Choi, D.E. Kim, B. S. Kim, B. J. Lee, and Y. S. Kwon, “Electron transporting layer effect of OLED using Zn(HPQ)$_2$,” *Molecular Crystals and Liquid Crystals*, vol. 520, pp. 90–96, 2010.

[13] J. F. Wang, G. E. Jabbour, E. A. Mash et al., “Oxadiazole metal complex for organic light-emitting diodes,” *Advanced Materials*, vol. 11, no. 15, pp. 1266–1269, 1999.

[14] R. Pohl, V. A. Montes, J. Shinar, and P. Anzenbacher, “Red-green-blue emission from tris(5-aryl-8-quinolinolate)al(iii) complexes,” *Journal of Organic Chemistry*, vol. 69, no. 5, pp. 1723–1725, 2004.

[15] W. S. Kim, J. M. You, B. J. Lee, Y. K. Jang, D. E. Kim, and Y.-S. Kwon, “Synthesis and blue electroluminescent properties of zinc (ii) [2-(2-hydroxyphenyl)benzoxazole],” *Thin Solid Films*, vol. 515, no. 12, pp. 5070–5074, 2007.

[16] J. K. Park, D. E. Kim, T. D. Hoanh, Y. S. Kwon, and B. J. Lee, “Zinc complex based on 2-(5-methyl-2-hydroxyphenyl)benzotriazole: synthesis and electroluminescence characteristics,” *Journal of Nanoscience and Nanotechnology*, vol. 8, no. 10, pp. 5071–5075, 2008.

[17] N. Nakamura, S. Wakabayashi, K. Miyairi, and T. Fujii, “A novel blue light emitting material prepared from 2-(o-Hydroxyphenyl)benzoxazole,” *Chemistry Letters*, vol. 23, no. 9, p. 1741, 1994.

[18] T. Yasuda, Y. Yamaguchi, K. Fujita, and T. Tsutsui, “Electron and hole mobility in vacuum deposited organic thin films of bis[2-(2-hydroxyphenyl)benzoxazolate]zinc and its derivatives,” *Chemistry Letters*, vol. 32, no. 7, pp. 644–645, 2003.

[19] F. S. Rodembusch, F. R. Brand, D. S. Corrêa, J. C. Pocos, M. Martinelli, and V. Stefani, “Transition metal complexes from 2-(2′-hydroxyphenyl)benzoxazole: a spectroscopic and thermogravimetric stability study,” *Materials Chemistry and Physics*, vol. 92, no. 2-3, pp. 389–393, 2005.

[20] J. Olivier, B. Servet, M. Vergnolle, M. Mosca, and G. Garry, “Stability/instability of conductivity and work function changes of ito thin films, uv-irradiated in air or vacuum. measurements by the four-probe method and by kelvin force microscopy,” *Synthetic Metals*, vol. 122, no. 1, pp. 87–89, 2001.

Research Article

Urea-Based Synthesis of Zinc Oxide Nanostructures at Low Temperature

J. Z. Marinho,[1] F. C. Romeiro,[1] S. C. S. Lemos,[1] F. V. Motta,[2] C. S. Riccardi,[3] M. S. Li,[4] E. Longo,[3] and R. C. Lima[1]

[1] *Instituto de Química, Universidade Federal de Uberlândia, 38400-902 Uberlândia, MG, Brazil*
[2] *Departamento de Engenharia de Materiais, Universidade Federal do Rio Grande do Norte, 59072-970 Natal, RN, Brazil*
[3] *Instituto de Química, Universidade Estadual Paulista, 14800-900 Araraquara, SP, Brazil*
[4] *Instituto de Física de São Carlos, Universidade de São Paulo, 13566-590 São Carlos, SP, Brazil*

Correspondence should be addressed to R. C. Lima, rclima@iqufu.ufu.br

The preparation of nanometer-sized structures of zinc oxide (ZnO) from zinc acetate and urea as raw materials was performed using conventional water bath heating and a microwave hydrothermal (MH) method in an aqueous solution. The oxide formation is controlled by decomposition of the added urea in the sealed autoclave. The influence of urea and the synthesis method on the final product formation are discussed. Broadband photoluminescence (PL) behavior in visible-range spectra was observed with a maximum peak centered in the green region which was attributed to different defects and the structural changes involved with ZnO crystals which were produced during the nucleation process.

1. Introduction

Zinc oxide (ZnO) is a well-known semiconducting material with photoluminescent and electric conductivity which has a band gap value of 3.37 eV and an excitation energy band of 60 meV at room temperature [1, 2]. With these properties, ZnO has a wide area of application such as solar cells [3, 4], catalysis [5, 6], sensors [7], laser diodes [8], and varistors [5, 9]. Chemical and structural properties of ZnO particles are very important in these applications; different preparation methods for this oxide were used by various researchers such as a sol-gel process [10], homogeneous precipitation [5], thermal decomposition [11], microwave heating [12], a conventional hydrothermal method [13–17], a polymeric precursor method [10], and an MH-assisted method [18, 19]. The characteristics of the powders obtained for specific applications are determined by the crystal size, morphology, porosity, crystal type, and particle shape [6, 20, 21].

The use of polymers or surfactants [22, 23] to prepare zinc oxide nanoparticles is advantageous due to a surface modification process which eliminates agglomeration during synthesis and controls the morphology and the shape of developed ZnO nanocrystals. However, repetitive washing and centrifugation is required with appropriate reagents such as absolute ethanol and distilled water. Therefore, directly controlling experimental factors to obtain nanoparticles with ideal morphologies is a significant objective which is essential for future device application [24]. Furthermore, the MH method has commanded intensive interest due to simple manipulation, low cost, clean technology, and short synthesis time [25–27].

In this paper, the effect of the synthesis method on the formation of zinc oxide nanostructures in an aqueous solution was investigated. Thus, we prepared this oxide using conventional water bath heating and the MH method using urea as one of the reactants. The samples were characterized by field emission gun scanning electron microscopy (FE-SEM) and Raman spectroscopy. The formation of a hexagonal ZnO wurtzite phase was verified by X-ray diffraction (XRD) patterns. The morphology, growth mechanism, and PL properties were recorded.

2. Experimental

2.1. Synthesis. Zinc oxide nanostructures were obtained: zinc acetate ($Zn(CH_3COO)_2 \cdot 2H_2O$) (99%, Aldrich) and urea ($CO(NH_2)_2$) (99%, Synth) (1 : 1 stoichiometry) were dissolved in deionized water under constant agitation. A potassium hydroxide (KOH) (3.0 mol/L solution) was added until the pH reached 12 followed by stirring at room temperature for 15 min.

The solution was then heated by two different methods: conventional water bath heating and the MH method. In the MH heating, the solution was transferred to a Teflon-lined stainless steel autoclave, sealed, and placed in domestic microwave (2.45 GHz) which was maintained at 100°C for 2 and 8 min. The pressure in the sealed autoclave was stabilized at 1.0 atm. The autoclave was cooled to room temperature naturally. A white product was separated by centrifugation, washed with deionized water and ethanol, and dried at 60°C in air.

2.2. Characterization of Samples. The powders obtained were structurally characterized by XRD using a Shimadzu XRD 6000 (Japan) equipped with CuK$\propto$ radiation ($\lambda = 1.5406$ Å) in the 2θ range from 10° to 80° with 0.02°/min scan increment. The morphology was characterized by FE-SEM (Supra 35-VP, Carl Zeiss, Germany). Raman spectra were recorded on a RFS/100/S Bruker FT-Raman spectrometer with a Nd:YAG laser providing an excitation light at 1064.0 nm and a spectral resolution of 4 cm^{-1}. The PL was measured with a Thermal Jarrel-Ash Monospec 27 monochromator and a Hamamatsu R446 photomultiplier. The 350.7 nm exciting wavelength of a krypton ion laser (Coherent Innova) was employed, and the nominal output power of the laser was maintained at 550 mW. All measurements were made at room temperature.

3. Results and Discussion

XRD patterns of samples obtained using conventional water bath heating and the MH method for 2 and 8 min are shown in Figure 1. The results revealed that all diffraction peaks can be indexed to the hexagonal ZnO structure which shows good agreement with data reported in the literature (JCPDS card number 36–1451). The strong and sharp peaks indicate that the zinc oxide powders are highly crystalline and structurally ordered at long range. These results show that the MH processing promotes the complete crystallization of ZnO samples at low temperatures and reduced processing time. No secondary phases were detected.

Five active Raman modes can be observed for ZnO samples: (i) at 437 cm^{-1} a narrow strong band has been assigned to one of the two E_2 modes involving mainly a Zn motion which is a band characteristic of the wurtzite phase [35]; (ii) bands at approximately 332 cm^{-1} and several common low-frequency features should be assigned to the second-order Raman spectrum arising from zone boundary phonons $3E_{2H}$-E_{2L}; (iii) at 530 cm^{-1}, a very weak band from the E_1 (LO) mode of ZnO associated with oxygen deficiency [36]. Its intensity depends upon the crystallinity,
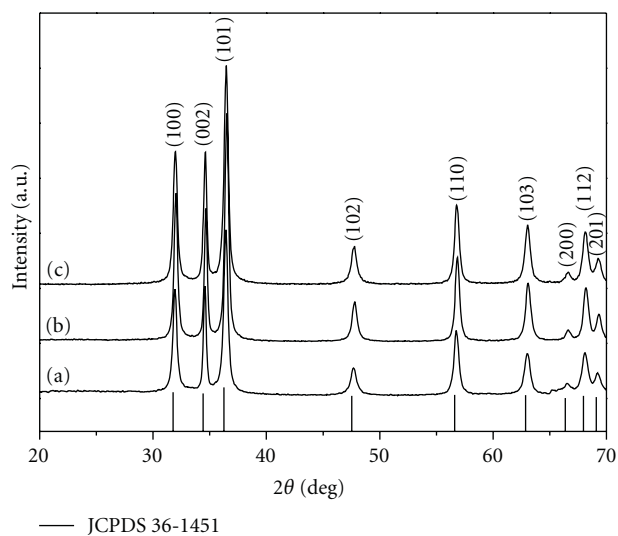

FIGURE 1: XRD patterns of the ZnO sample obtained by (a) conventional water bath heating, (b) the MH method for 2 min, and (c) the MH method for 8 min.

preparation method and crystal orientation. Figure 2 shows Raman spectra of ZnO powders obtained. The asymmetric band at 378 cm^{-1} (A_{1T} mode) related to the structural order-disorder in the lattice [37] is covered by broad band characteristic of a Zn–O bond at 437 cm^{-1}.

Well-crystallized zinc compounds with different morphologies can be obtained by several synthesis methods by using urea (see Table 1). Precursors, the concentration of urea, the synthesis method and the reaction time are important factors influencing the structural evolution and the morphology of the products. The weak basicity of the solution gives rise to a zinc carbonate species product (Table 1). The use of MH crystallization facilitates the direct preparation of pure oxide powders in less time with desired particle sizes and shapes from the control parameters such as solution pH, reaction temperature, reaction time, solute concentration and the type of solvent [38–40].

Hydrolysis characteristics of urea are well known in H_2O over 293–373 K at 1 bar [41]. Urea is highly soluble in water, and its controlled hydrolysis in aqueous solutions can yield ammonia and carbon dioxide. In the crystal growth process, first ZnO tiny crystalline nuclei were formed, and nanoparticles of this oxide were precipitated by an increase in pH due to NH_4^+ ions generated from of NH_3 which resulted from urea decomposition when the temperature rose. The NH_4^+ ion formation is controlled by ammonia in water, and the hydrolysis of urea leads to a rise in the pH. The urea hydrolysis progresses slowly, and the basic solution undergoes supersaturation of the zinc hydroxide species [42]. Thus, the formation of ZnO occurs by a nucleation process and the preferred growth direction of the crystal.

During the MH process, the urea is readily hydrolyzed; its hydrolysis is also accompanied by the formation of gas molecules and an increase in the pressure in the system which is expected to perturb nanocrystalline growth and thereby

TABLE 1: Zinc species obtained by different synthesis method using urea as a precursor.

| Synthesis method	Product 1	Temperature/time	Product 2	Morphology/size	Reference
Precipitation	$Zn_5(OH)_6(CO_3)_2$ + ZnO	4 h of synthesis	ZnO	Bipods/3.1–7.9 μm	[3]
Precipitation	$[Zn(OH)_2(H_2O)_2]$	1000°C/2 h	ZnO	Hexagonal plates/35–45 μm	[6]
Sol-gel	$Zn_5(OH)_6(CO_3)_2$	500°C–900°C/2 h	ZnO	Spherical particles/20 nm	[28]
Conventional hydrothermal	white powder	550°C/4 h	ZnO	Column-, rosette-fiber-like/0,5–10 μm	[29]
Microwave-induced combustion technique	ZnO	—	—	Flowers-like/2–5 μm	[30]
Refluxing route	ZnO	—	—	Rods-likes/30–40 nm (diameter) and 500–700 nm (length)	[31]
Conventional hydrothermal	$Zn_5(OH)_6(CO_3)_2$	500°C/1 h	ZnO	Spherical particles/25 nm	[32]
Conventional hydrothermal	$Zn_4(OH)_6CO_3 \cdot H_2O$	400°C/2 h	ZnO	Flakes-like/0.65–1.5 mm	[33]
Conventional hydrothermal	$Zn_5(OH)_6(CO_3)_2$	600°C	ZnO	Flakes-like/10–20 nm	[11]
Solvothermal	$ZnOCO_3$ + ZnO	180°C/24 h	ZnO	Spherical particles/50–300 nm	[23]
Urea aqueous solution process	$Zn_5(OH)_6(CO_3)_2$	600°C/30 min	ZnO	Spherical chrysanthemums/2–6 μm	[34]
Conventional water bath heating	ZnO	—	—	Irregular nanoparticles	This work
Microwave-assisted hydrothermal	ZnO	—	—	Spheres-like/85 nm	This work
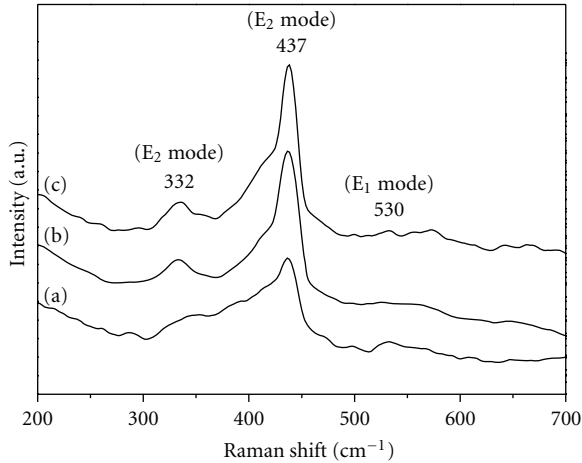
FIGURE 2: Raman spectra of ZnO powders prepared by (a) conventional water bath heating, (b) the MH method for 2 min, and (c) the MH method for 8 min.
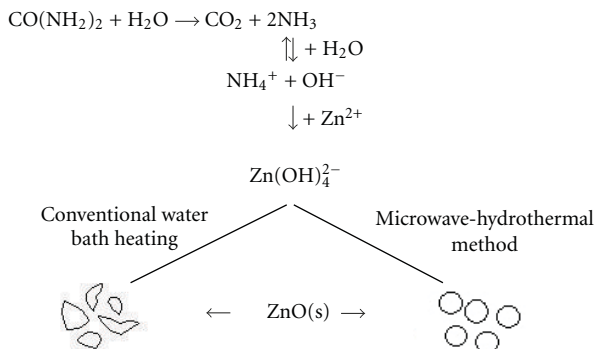
TABLE 2: Fitting parameters of five Gaussian peaks.

Peak center (eV)	1.76	1.95	2.15	2.36	2.61
Conventional water bath heating (area %)	11.1	29.0	34.5	19.0	6.4
MH for 2 min (area %)	10.1	26.1	31.2	24.1	8.5
MH for 8 min (area %)	9.2	29.9	33.5	20.8	6.5

FIGURE 3: Schematic representation of ZnO formation.

results in morphological changes. This process may accelerate the reaction between the synthesis precursors which leads to anisotropic crystal growth and the crystallization of oxide under mild temperature conditions and reaction times. A schematic representation of ZnO nanostructure formation is shown in Figure 3.

The morphology of ZnO powders was investigated using FE-SEM (see Figure 4). These images reveal that samples prepared without the MH process had an irregular shape and were not uniform in size, whereas spherical and uniform particles were observed for samples prepared using the MH method. The MH method contributes significantly to ZnO production with homogeneous shapes after short processing times.

Diffusivity in the medium and interface mobility could be enhanced using the MH process which contributes significantly to ZnO production with homogeneous shapes after short processing times. Nanosized structures were formed by this method, and different average particle distributions were obtained after treatment under hydrothermal conditions (see inset in Figures 4(b) and 4(c)). Average particle diameters were 90 nm and 85 nm for samples treated by the MH process for 2 and 8 min, respectively.

Disordered structures in solids cause degeneracy and destabilization in the localized states of the atoms which act
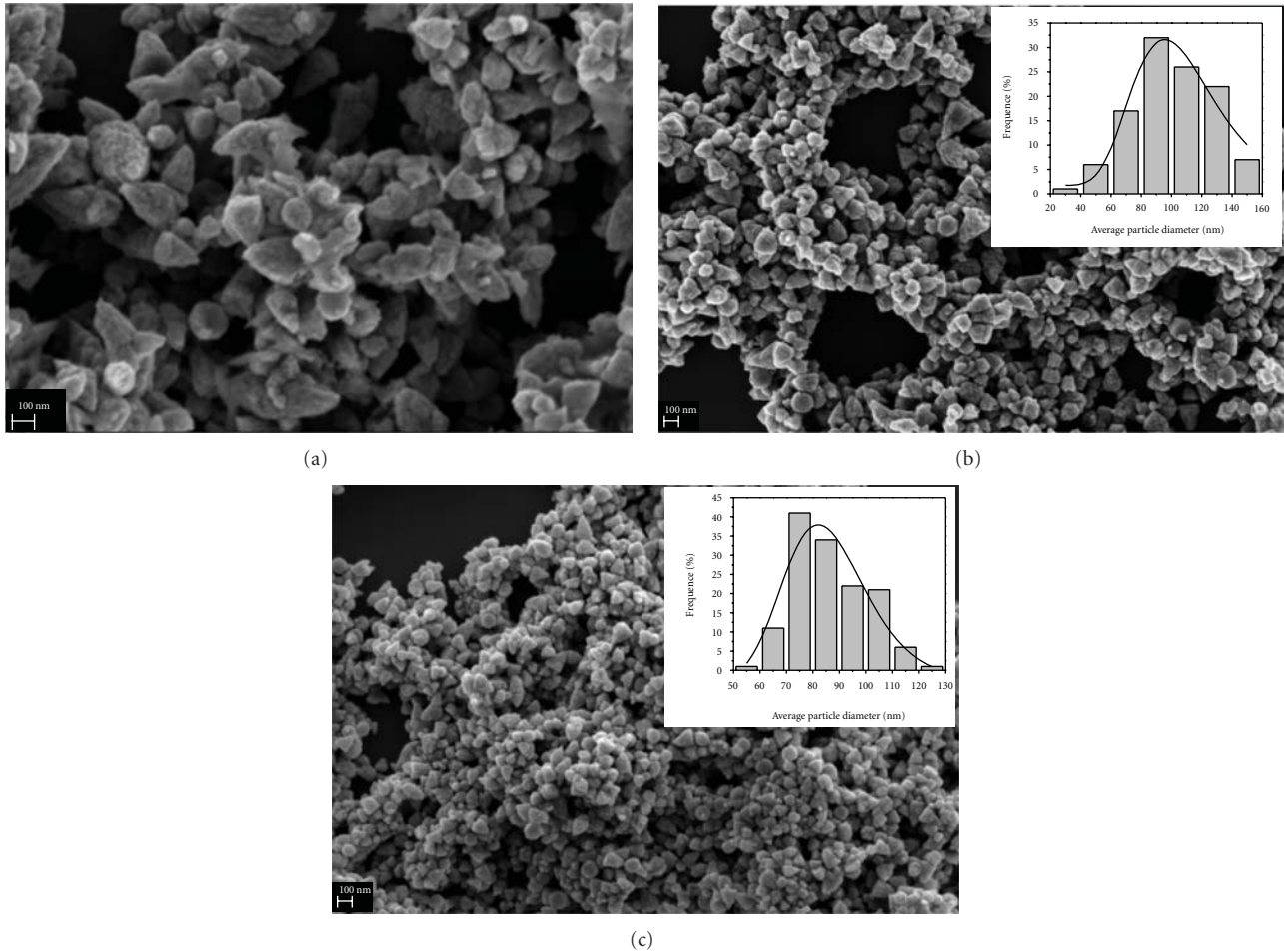
(a)

(b)

(c)

FIGURE 4: FE-SEM images of ZnO powders prepared using (a) conventional water bath heating, (b) the MH method for 2 min (average distribution of particles is inserted), and (c) the MH method for 8 min (average distribution of particles is inserted).

as electron-hole pairs and support broadband PL phenomena. PL spectra recorded at room temperature are illustrated in Figure 5(a).

Theoretical results verify that a symmetry breaking process in the structure of various semiconductors associated with order-disorder effects is a necessary condition for intermediate levels in the forbidden band gap [43–45]. These structural changes can be related to the charge polarization in different ranges that are (at the very least) manifestations of quantum confinement when they occur at short and intermediate ranges independent of the particle size. The main reason for quantum confinement to occur is the formation of discrete levels in the band gap which is not possible with as a periodic crystal defect (dispersion interaction) [46]. The formation of isolated energy levels (quantum confinement) and $[ZnO_3 \cdot V_o^\bullet]$ clusters leads to a substantial recombination between photoexcited electrons and holes during the excitation process. Probably the $[ZnO_4]^x - [ZnO_3 \cdot V_o^x]$ clusters are activated during the excitation process which changes their symmetry in progressing from singlet or triplet states as demonstrated for the perovskite

structure [47]. These defects induce new energies in the band gap which can be attributed to zinc-oxygen vacancy centers. The structural and electronic reconstructions of all possible combinations of clusters in a crystal are essential to understand the cluster-to-cluster charge transfer process and even the PL phenomenon.

PL curves were decomposed into five components using the Gaussian method and the Peak Fit program: a red component (1.76 eV), a yellow component (1.95 eV), two green components (2.15 and 2.36 eV), and a blue component (2.61 eV). These emissions arise from a radiative recombination between electrons and holes trapped in the gap states. Figures 5(b) to 5(d) illustrate decomposition data, and Table 2 lists the areas under each curve of the respective transitions. The percentage was obtained by dividing the area of each decomposed PL curve by the total PL area. Each color represents a different type of electronic transition and can be linked to a specific structural arrangement. The high PL intensity displayed by the sample obtained for 2 min under MH conditions seems to indicate that this material must
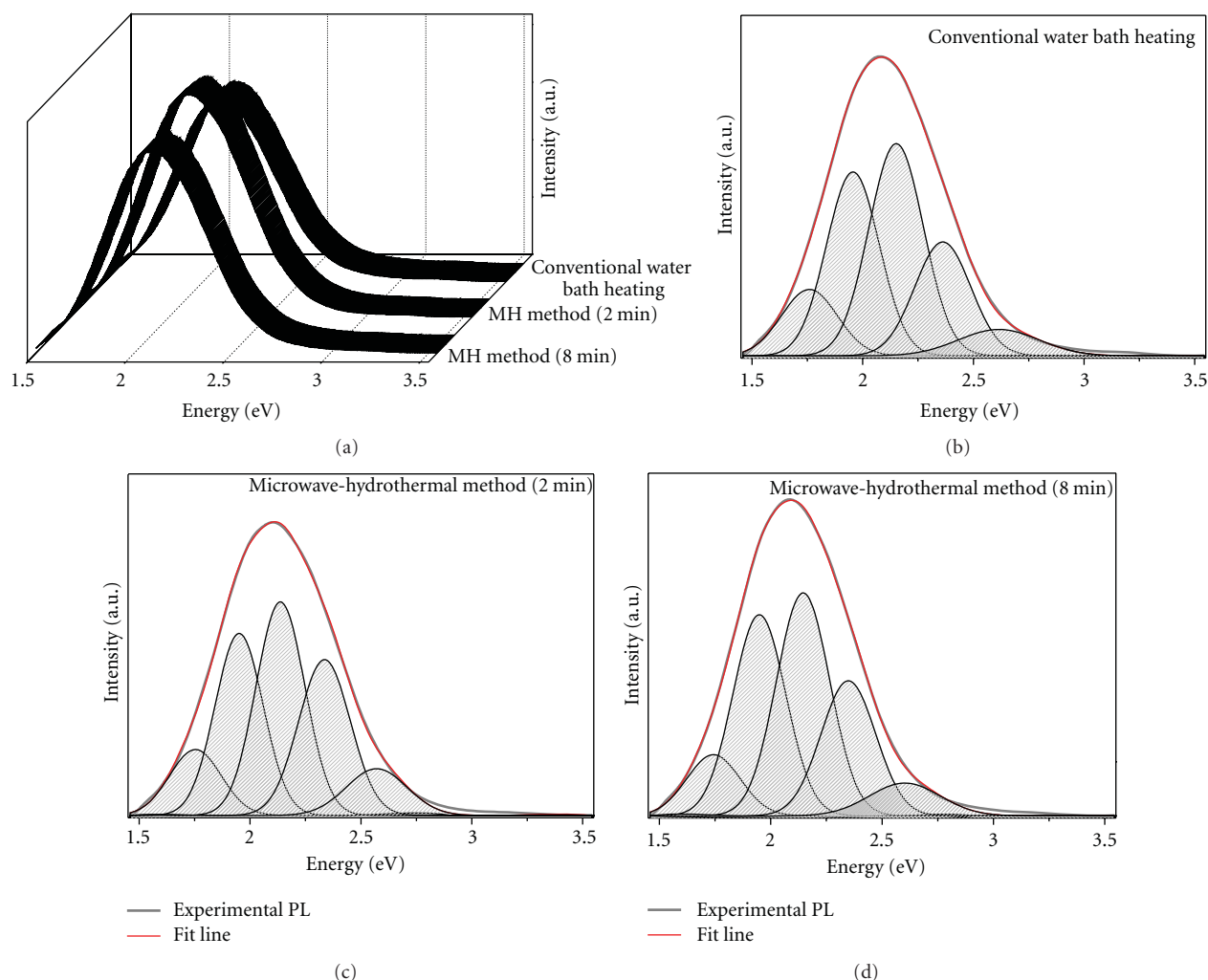
FIGURE 5: (a) PL spectra at room temperature of ZnO powders; deconvolution results of ZnO samples obtained by (b) conventional water bath heating, (c) the MH method for 2 min, and (d) the MH method for 8 min.

possess an optimum structural order-disorder degree for PL to occur.

4. Conclusions

The MH process affects the growth process of ZnO nanostructures from an aqueous solution of zinc acetate and urea which leads to the rapid and uniform growth of particles. The PL emission of semiconductors is an important property because it can provide information on defects and relaxation pathways of excited states depending upon the preparation techniques which can generate different structural defects.

Acknowledgments

References

[1] Y. Huang, X. Duan, Q. Wei, and C. M. Lieber, "Directed assembly of one-dimensional nanostructures into functional networks," *Science*, vol. 291, no. 5504, pp. 630–633, 2001.

[2] Q. X. Zhao, M. Willander, R. E. Morjan, Q. H. Hu, and E. E. B. Campbell, "Optical recombination of ZnO nanowires grown on sapphire and Si substrates," *Applied Physics Letters*, vol. 83, no. 1, pp. 165–167, 2003.

[3] M. Bitenc and Z. Crnjak Orel, "Synthesis and characterization of crystalline hexagonal bipods of zinc oxide," *Materials Research Bulletin*, vol. 44, no. 2, pp. 381–387, 2009.

[4] A. M. Peiró, P. Ravirajan, K. Govender et al., "Hybrid polymer/metal oxide solar cells based on ZnO columnar structures," *Journal of Materials Chemistry*, vol. 16, no. 21, pp. 2088–2096, 2006.

[5] C. K. Srikanth and P. Jeevanandam, "Effect of anion on the homogeneous precipitation of precursors and their thermal decomposition to zinc oxide," *Journal of Alloys and Compounds*, vol. 486, no. 1-2, pp. 677–684, 2009.

[6] K. Ada, M. Goekgoez, M. Oenal, and Y. Sankaya, "Preparation and characterization of a ZnO powder with the hexagonal plate particles," *Powder Technology*, vol. 181, no. 3, pp. 285–291, 2008.

[7] C. Cheng, B. Liu, H. Yang et al., "Hierarchical assembly of ZnO nanostructures on SnO_2 backbone nanowires: low-temperature hydrothermal preparation and optical properties," *ACS Nano*, vol. 3, no. 10, pp. 3069–3076, 2009.

[8] S. Baruah and J. Dutta, "Hydrothermal growth of ZnO nanostructures," *Science and Technology of Advanced Materials*, vol. 10, no. 1, Article ID 013001, 2009.

[9] S. D. G. Ram, M. A. Kulandainathan, and G. Ravi, "On the study of pH effects in the microwave enhanced rapid synthesis of nano-ZnO," *Applied Physics A*, vol. 99, no. 1, pp. 197–203, 2010.

[10] S. A. M. Lima, M. Cremona, M. R. Davolos, C. Legnani, and W. G. Quirino, "Electroluminescence of zinc oxide thin-films prepared via polymeric precursor and via sol-gel methods," *Thin Solid Films*, vol. 516, no. 2–4, pp. 165–169, 2007.

[11] S. Music, S. Popovic, M. Maljkovic, and E. Dragcevic, "Influence of synthesis procedure on the formation and properties of zinc oxide," *Journal of Alloys and Compounds*, vol. 347, no. 1-2, pp. 324–332, 2002.

[12] A. M. Peiro, C. Domingo, J. Peral et al., "Nanostructured zinc oxide films grown from microwave activated aqueous solutions," *Thin Solid Films*, vol. 483, no. 1-2, pp. 79–83, 2005.

[13] J. Jiang, Y. Li, S. Tan, and Z. Huang, "Synthesis of zinc oxide nanotetrapods by a novel fast microemulsion-based hydrothermal method," *Materials Letters*, vol. 64, no. 20, pp. 2191–2193, 2010.

[14] M. Mo, J. C. Yu, L. Zhang, and S. K. A. Li, "Self-assembly of ZnO nanorods and nanosheets into hollow microhemispheres and microspheres," *Advanced Materials*, vol. 17, no. 6, pp. 756–760, 2005.

[15] A. Wei, X. W. Sun, C. X. Xu et al., "Growth mechanism of tubular ZnO formed in aqueous solution," *Nanotechnology*, vol. 17, no. 6, pp. 1740–1744, 2006.

[16] D. R. Chen, X. Jiao, and G. Cheng, "Hydrothermal synthesis of zinc oxide powders with different morphologies," *Solid State Communications*, vol. 113, no. 6, pp. 363–366, 2000.

[17] C. H. Lu and C. H. Yeh, "Influence of hydrothermal conditions on the morphology and particle size of zinc oxide powder," *Ceramics International*, vol. 26, no. 4, pp. 351–357, 2000.

[18] A. P. de Moura, R. C. Lima, M. L. Moreira et al., "ZnO architectures synthesized by a microwave-assisted hydrothermal method and their photoluminescence properties," *Solid State Ionics*, vol. 181, no. 15-16, pp. 775–780, 2010.

[19] Y.-C. Chen and S. L. Lo, "Effects of operational conditions of microwave-assisted synthesis on morphology and photocatalytic capability of zinc oxide," *Chemical Engineering Journal*, vol. 170, no. 2-3, pp. 411–418, 2011.

[20] L. N. Dem'yanets, V. V. Artemov, L. E. Li, Y. M. Mininzon, and T. G. Uvarova, "Zinc oxide hollow microstructures and nanostructures formed under hydrothermal conditions," *Crystallography Reports*, vol. 53, no. 5, pp. 888–893, 2008.

[21] Y. P. Fang, X. Wen, S. Yang et al., "Hydrothermal synthesis and optical properties of ZnO nanostructured films directly grown from/on zinc substrates," *Journal of Sol-Gel Science and Technology*, vol. 36, no. 2, pp. 227–234, 2005.

[22] C. G. Kim, K. Sung, T. M. Chung, D. Y. Jung, and Y. Kim, "Monodispersed ZnO nanoparticles from a single molecular precursor," *Chemical Communications*, vol. 9, no. 16, pp. 2068–2069, 2003.

[23] C. L. Wang, E. Wang, E. Shen et al., "Growth of ZnO nanoparticles from nanowhisker precursor with a simple solvothermal route," *Materials Research Bulletin*, vol. 41, no. 12, pp. 2298–2302, 2006.

[24] E. Savary, S. Marinel, H. Colder, C. Harnois, F. X. Lefevre, and R. Retoux, "Microwave sintering of nano-sized ZnO synthesized by a liquid route," *Powder Technology*, vol. 208, no. 2, pp. 521–525, 2011.

[25] M. L. Dos Santos, R. C. Lima, C. S. Riccardi et al., "Preparation and characterization of ceria nanospheres by microwave-hydrothermal method," *Materials Letters*, vol. 62, no. 30, pp. 4509–4511, 2008.

[26] L. S. Cavalcante, J. C. Sczancoski, J. W. M. Espinosa, J. A. Varela, P. S. Pizani, and E. Longo, "Photoluminescent behavior of $BaWO_4$ powders processed in microwave-hydrothermal," *Journal of Alloys and Compounds*, vol. 474, no. 1-2, pp. 195–200, 2009.

[27] J. F. Huang, C. Xia, L. Cao, and X. Zeng, "Facile microwave hydrothermal synthesis of zinc oxide one-dimensional nanostructure with three-dimensional morphology," *Materials Science and Engineering B*, vol. 150, no. 3, pp. 187–193, 2008.

[28] R. Wahab, S. G. Ansari, Y. S. Kim, M. A. Dar, and H. S. Shin, "Synthesis and characterization of hydrozincite and its conversion into zinc oxide nanoparticles," *Journal of Alloys and Compounds*, vol. 461, no. 1-2, pp. 66–71, 2008.

[29] G. F. Zou, D. Yu, D. Wang et al., "Controlled synthesis of ZNO nanocrystals with column-, rosette-and fiber-like morphologies and their photoluminescence property," *Materials Chemistry and Physics*, vol. 88, no. 1, pp. 150–154, 2004.

[30] Y. A. Cao, B. Liu, R. Huang, Z. Xia, and S. Ge, "Flash synthesis of flower-like ZnO nanostructures by microwave-induced combustion process," *Materials Letters*, vol. 65, no. 2, pp. 160–163, 2011.

[31] J. W. Zhang, W. Wang, P. Zhu, J. Chen, Z. Zhang, and Z. Wu, "Synthesis of small diameter ZnO nanorods via refluxing route in alcohol-water mixing solution containing zinc salt and urea," *Materials Letters*, vol. 61, no. 2, pp. 592–594, 2007.

[32] S.-H. Hu, Y. C. Chen, C. C. Hwang, C. H. Peng, and D. C. Gong, "Analysis of growth parameters for hydrothermal synthesis of ZnO nanoparticles through a statistical experimental design method," *Journal of Materials Science*, vol. 45, no. 19, pp. 5309–5317, 2010.

[33] L. L. Wu, Y. Wu, and Y. Lü, "Self-assembly of small ZnO nanoparticles toward flake-like single crystals," *Materials Research Bulletin*, vol. 41, no. 1, pp. 128–133, 2006.

[34] M. Bitenc, M. Marinšek, and Z. Crnjak Orel, "Preparation and characterization of zinc hydroxide carbonate and porous zinc oxide particles," *Journal of the European Ceramic Society*, vol. 28, no. 15, pp. 2915–2921, 2008.

[35] C. Li, Y. Lv, L. Guo, H. Xu, X. Ai, and J. Zhang, "Raman and excitonic photoluminescence characterizations of ZnO star-shaped nanocrystals," *Journal of Luminescence*, vol. 122-123, no. 1-2, pp. 415–417, 2007.

[36] C. F. Windisch Jr, G. J. Exarhos, C. Yao, and L. Q. Wang, "Raman study of the influence of hydrogen on defects in ZnO," *Journal of Applied Physics*, vol. 101, no. 12, Article ID 123711, 2007.

[37] Z. W. Dong, C. F. Zhang, H. Deng, G. J. You, and S. X. Qian, "Raman spectra of single micrometer-sized tubular ZnO," *Materials Chemistry and Physics*, vol. 99, no. 1, pp. 160–163, 2006.

[38] J. S. Lee and S. C. Choi, "Crystallization behavior of nano-ceria powders by hydrothermal synthesis using a mixture of H_2O_2

and NH$_4$OH," *Materials Letters*, vol. 58, no. 3-4, pp. 390–393, 2004.

[39] S. Komarneni, Q. H. Li, and R. Roy, "Microwave-hydro-thermal processing for synthesis of layered and network phosphates," *Journal of Materials Chemistry*, vol. 4, no. 12, pp. 1903–1906, 1994.

[40] S. Komarneni, R. Pidugu, Q. H. Li, and R. Roy, "Microwave-hydrothermal processing of metal powders," *Journal of Materials Research*, vol. 10, no. 7, pp. 1687–1692, 1995.

[41] M. L. Kieke, J. W. Schoppelrei, and T. B. Brill, "Spectroscopy of hydrothermal reactions. 1. The CO$_2$-H$_2$O system and kinetics of urea decomposition in an FTIR spectroscopy flow reactor cell operable to 725 K and 335 bar," *Journal of Physical Chemistry*, vol. 100, no. 18, pp. 7455–7462, 1996.

[42] K. Kakiuchi, E. Hosono, T. Kimura, H. Imai, and S. Fujihara, "Fabrication of mesoporous ZnO nanosheets from precursor templates grown in aqueous solutions," *Journal of Sol-Gel Science and Technology*, vol. 39, no. 1, pp. 63–72, 2006.

[43] E. Longo, E. Orhan, F. M. Pontes et al., "Density functional theory calculation of the electronic structure of Ba$_{0.5}$Sr$_{0.5}$TiO$_3$: photoluminescent properties and structural disorder," *Physical Review B*, vol. 69, no. 12, pp. 125115–125117, 2004.

[44] V. M. Longo, E. Orhan, L. S. Cavalcante et al., "Understanding the origin of photoluminescence in disordered Ca$_{0.60}$Sr$_{0.40}$WO$_4$: an experimental and first-principles study," *Chemical Physics*, vol. 334, no. 1–3, pp. 180–188, 2007.

[45] R. C. Lima, L. R. Macario, J. W. M. Espinosa et al., "Toward an understanding of intermediate- and short-range defects in ZnO single crystals. A combined experimental and theoretical study," *Journal of Physical Chemistry A*, vol. 112, no. 38, pp. 8970–8978, 2008.

[46] R. C. Lima, J. Andres, J. R. Sambrano et al., *Photoluminescence: Applications, Types and Efficacy: An Overview on the Photoluminescence Emission in ZnO Single Crystal: A Joint Experimental and Theoretical Analysis*, Nova Science Publishers, New York, NY, USA, 2012.

[47] L. Gracia, J. Andrés, V. M. Longo, J. A. Varela, and E. Longo, "A theoretical study on the photoluminescence of SrTiO$_3$," *Chemical Physics Letters*, vol. 493, no. 1–3, pp. 141–146, 2010.

Research Article

Crystallinity Improvement of ZnO Thin Film on Different Buffer Layers Grown by MBE

Shao-Ying Ting,[1] Po-Ju Chen,[2,3] Hsiang-Chen Wang,[2,3] Che-Hao Liao,[1] Wen-Ming Chang,[1] Ya-Ping Hsieh,[2,3] and C. C. Yang[1]

[1] *Institute of Photonics and Optoelectronics, National Taiwan University, Taipei 10617, Taiwan*
[2] *Graduate Institute of Opto-Mechatronics, National Chung Cheng University, Chia-Yi 62102, Taiwan*
[3] *Advanced Institute for Manufacturing with High-Tech Innovations, National Chung Cheng University, Chia-Yi 62102, Taiwan*

Correspondence should be addressed to Hsiang-Chen Wang, hcwang@ccu.edu.tw

The material and optical properties of ZnO thin film samples grown on different buffer layers on sapphire substrates through a two-step temperature variation growth by molecular beam epitaxy were investigated. The thin buffer layer between the ZnO layer and the sapphire substrate decreased the lattice mismatch to achieve higher quality ZnO thin film growth. A GaN buffer layer slightly increased the quality of the ZnO thin film, but the threading dislocations still stretched along the *c*-axis of the GaN layer. The use of MgO as the buffer layer decreased the surface roughness of the ZnO thin film by 58.8% due to the suppression of surface cracks through strain transfer of the sample. From deep level emission and rocking curve measurements it was found that the threading dislocations play a more important role than oxygen vacancies for high-quality ZnO thin film growth.

1. Introduction

Recently, ZnO has received considerable attention due to its excellent emission properties in the UV region. ZnO is a direct band-gap material with wurtzite-structure, exhibits a wide band-gap of 3.37 eV, and has a large exciton binding energy of 60 meV at room temperature [1]. Based on these fundamental properties, ZnO has many applications in the short wavelength region such as optically pumped lasers, UV light emitting diodes, detectors, solar cells, and gas sensors [2–6]. However, the growth of ZnO thin film for such applications still remains problematic. So far, various methods have been employed to grow high quality ZnO thin films, for example, sputtering, pulsed laser deposition, metal organic chemical vapor deposition (MOCVD), and molecular beam epitaxy (MBE) [7–10]. MBE is a promising technique for the growth of high quality ZnO thin films due to its operation in ultra-high-vacuum conditions ($> 10^{-9}$ torr), using ultra pure substrates (6 N), and Angstrom-scale-thickness control. ZnO films are grown on different substrates including c-Al_2O_3, ZnO, GaN, and $ScAlMgO_4$. Among these substrates,

c-Al_2O_3 is the most frequently used because of its low price, ease of producing large wafers, and ready availability for growing epitaxial films [11]. When ZnO films are grown on c-Al_2O_3 substrates without a buffer layer, however, the ZnO films generally show poor crystalline quality with a high dislocation density because of the 18% lattice mismatch between ZnO and c-Al_2O_3. Furthermore, a large difference in the thermal expansion coefficients between ZnO and c-Al_2O_3 ($\alpha_{ZnO} = 6.51 \times 10^{-6}$ K^{-1} and $\alpha_{sapphire} = 8.00 \times 10^{-6}$ K^{-1}) will generate strain under the high temperature growth conditions. Chen et al. demonstrated a two-step growth method that carries out the initial growth at a lower temperature followed by a growth step at high temperature. Through this method a densely packed ZnO film with larger grains and well-aligned crystallographic orientation can be obtained [12].

In addition, the improvement in growth quality by using a buffer layer to decrease the lattice mismatch between ZnO and c-Al_2O_3 is a well-known method. These thin buffer layers for growing ZnO are GaN, MgO, ZnS, or SiC [13–16]. GaN and MgO are the most popular buffer layers for

ZnO grown on sapphire substrate. With the GaN buffer layer, the similar lattice structure, low lattice mismatch between ZnO and GaN, and similar thermal expansion coefficients ($\alpha_{\mathrm{GaN}} = 5.59 \times 10^{-6}\,\mathrm{K}^{-1}$) provide suitable conditions for ZnO growth [17]. Thus, a GaN buffer layer can solve the cracking problem during the quick growth of ZnO thin films by acting as a homoepitaxy quasi substrate [18]. A ZnO thin film on a GaN buffer layer on a c-sapphire substrate does, however, suffer compressive stress.

When using MgO as a buffer layer there are two approaches to solving the issues of high quality ZnO growth. For high temperature growths (750–850°C), the interaction between MgO and Al_2O_3 dominats: the Mg^{2+} and Al^{3+} diffuse to form a spinel intermediate layer ($MgAl_2O_4$). The 18% lattice mismatch between ZnO and Al_2O_3 is stepwise divided between ZnO/MgO, MgO/spinel, and spinel/Al_2O_3. A maximum mismatch of about 9.2% remains at the ZnO/MgO interface while the lattice mismatch between the MgO grains and the spinel layer is about 5.6%. Experiments reveal that the density of threading dislocation decreases by a factor of five when using MgO as the buffer layer [19].

For ZnO growth at low temperature (~600°C), the reaction between MgO and Al_2O_3 cannot occur, but the MgO buffer layer still decreases the lattice mismatch during the ZnO growth. For thin MgO layers, the ZnO grown on the MgO layer is a layer-by-layer epitaxy and the threading dislocations cannot stretch along the c-axis of the ZnO. In such a condition, the threading dislocations of the ZnO cluster occur only within 20 nm of the ZnO/MgO interface, which can improve the crystallization quality of the ZnO growth [20, 21].

In this paper, the growth of ZnO thin films on c-plane sapphire substrates by a two-step temperature variation was demonstrated using different MBE-deposited buffer layers. Temperature-dependent photoluminescence results showed the optical features of ZnO thin film samples with and without buffer layers. The crystallization quality and strain distribution of ZnO structures were analyzed through X-ray diffraction (XRD) and X-ray rocking curve (XRC) measurements. The surface morphologies of the ZnO thin films were studied by atomic force microscopy (AFM) and scanning electron microscopy (SEM). The ZnO thin film with a 7 nm thick MgO buffer layer, 18 nm thick low-temperature-grown ZnO layer, and 100 nm thick high-temperature-grown ZnO layer showed the best crystallization properties in this study.

2. Growth Conditions and Structures of the Growth Samples

The ZnO thin films were grown on commercial (0001) c-Al_2O_3 substrates by MBE. For Sample A, ZnO was grown with a thickness of 6 nm at low temperature (LT) on the c-Al_2O_3 substrate with no buffer layer. In this step, the growth temperature, beam equivalent pressure, and O_2 flow rate were 500°C, 5×10^{-7} torr, and 3 sccm, respectively. Then ZnO was grown with a thickness of 600 nm at high temperature (HT) on the LT-ZnO layer. In this step, the growth temperature, beam equivalent pressure, and O_2 flow rate were 600°C, 6×10^{-7} torr, and 4 sccm, respectively. Sample B is a ZnO thin film on a GaN buffer layer. The GaN buffer layer was grown on a c-Al_2O_3 substrate at 1,000°C with a thickness of $2\,\mu m$ by MOCVD. Then the LT-ZnO was grown with a thickness of 10 nm on the GaN buffer layer. In this step, the growth temperature, beam equivalent pressure, and O_2 flow rate were 300°C, 5×10^{-7} torr, and 3 sccm, respectively. Finally, HT-ZnO was grown with a thickness of 250 nm on the LT-ZnO layer. In this step, the growth temperature, beam equivalent pressure, and O_2 flow rate were 600°C, 5×10^{-7} torr, and 2 sccm, respectively. Samples C, D, and E were ZnO thin films on 7 nm thick MgO buffer layers, which were grown on c-Al_2O_3 substrates. In this step, the growth temperature, beam equivalent pressure, and O_2 flow rate were 550°C, 2×10^{-7} torr, and 3 sccm, respectively. For these samples, the growth conditions of the LT-ZnO layers were the same as for Sample B. But sample D had an 18 nm-thick LT-ZnO layer. For the HT-ZnO layers, these three samples had the same growth temperature of 600°C as for Sample B. In this step, the growth thickness, beam equivalent pressure, and O_2 flow rate of Samples C, D, and E were 400 nm, 7.5×10^{-7} torr, and 3.5 sccm; 100 nm, 5.0×10^{-7} torr, and 2.5 sccm; 100 nm, 5.0×10^{-7} torr, and 1.4 sccm, respectively. Figure 1 summarizes the layer structures of the samples.

Samples A, B, C, and D were grown in an O_2-rich condition. Sample E was grown in the stoichiometric condition ($Zn : O_2 = 1 : 1$), which results in more oxygen vacancies. After the HT-ZnO layers' growth, all of the samples were annealed at 700°C for 10 minutes to improve crystallization. Table 1 shows the growth parameters of the samples.

3. XRD and XRCs Measurements

Figure 2 shows the XRD spectra of the samples with only (002) ZnO peak. Figure 3 shows the normalized XRC results of the samples. In this figure, the largest full width at half maximum (FWHM) of 791.74 arcsec was measured in Sample A, which indicated that a high density of threading dislocations existed due to a larger lattice mismatch between ZnO and c-Al_2O_3. The FWHM of Sample B was 242.58 arcsec, a 69.40% decrease from sample A. This decrease came from the small lattice mismatch of 1.80% between ZnO and GaN, which resulted in a decrease of the dislocation density in the ZnO layer. However, many threading dislocations still existed in the GaN buffer layer due to the larger lattice mismatch of 16% between GaN and the c-Al_2O_3 substrate. In this study, the GaN buffer layer in Sample B was thicker than MgO buffer layers in Samples C, D, and E to minimize the influence of lattice mismatch between GaN and c-Al_2O_3 for high quality ZnO thin film growth [13]. Thus, the GaN buffer layer showed some limitations for high quality ZnO thin film growth. The FWHM of Samples C, D, and E are 64.18, 48.66, and 98.01 arcsec, respectively, representing 91.89%, 93.85%, and 87.60% decreases compared to Sample A. These results indicate the higher quality of ZnO growth on an MgO buffer layer. Although the lattice mismatch between MgO and ZnO of 8.4% is more than that between ZnO and GaN (1.8%),
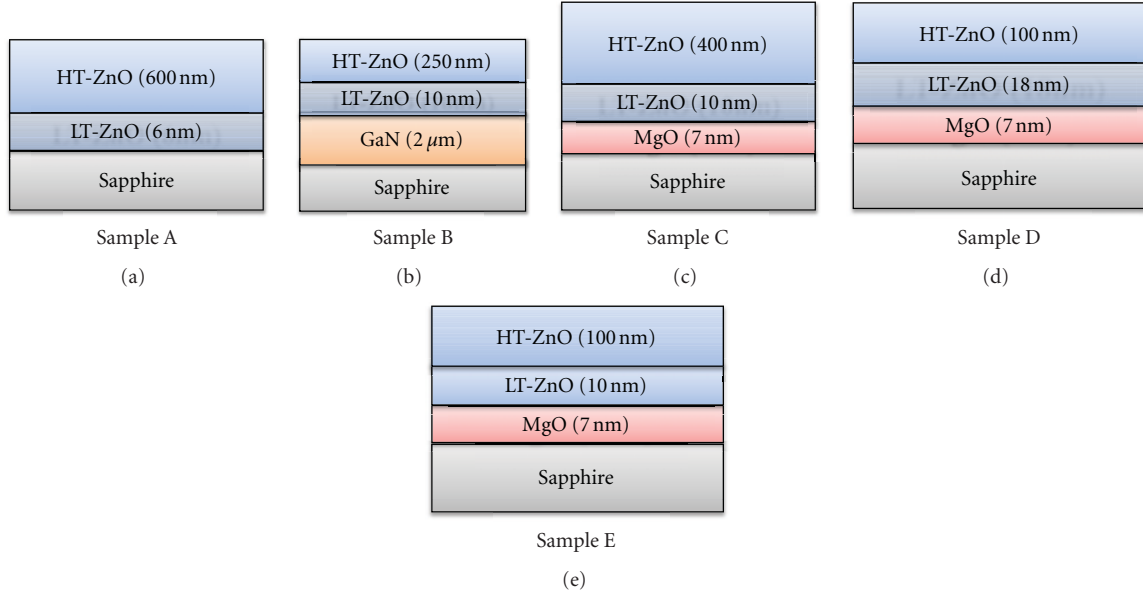
FIGURE 1: Schematic picture for the layer structures of (a) Sample A, (b) Sample B, (c) Sample C, (d) Sample D, and (e) Sample E used in this work.

TABLE 1: The growth parameters of ZnO thin film samples.

sample	HT-ZnO growth temperature (°C)	HT-ZnO growth conditions	HT-ZnO thickness (nm)	LT-ZnO	Buffer layer
A	600	O_2-rich	600	500°C 6 nm	N/A
B	600	O_2-rich	250	300°C 10 nm	1000°C 2 μm GaN
C	600	O_2-rich	400	300°C 10 nm	550°C 7 nm MgO
D	600	O_2-rich	100	300°C 18 nm	550°C 7 nm MgO
E	600	$Zn : O_2 = 1 : 1$	100	300°C 10 nm	550°C 7 nm MgO

the MgO buffer can effectively suppress the stretching of threading dislocations to the c-axis of the ZnO layer. The highest degree of crystallinity was achieved for ZnO thin films grown on 7 nm thick MgO buffer layers, which is a fivefold improvement over the 2 μm thick GaN buffer layer.

Table 2 shows the material parameters of ZnO thin film samples obtained from XRD measurement. The grain size of each sample was calculated using the Sherrer equation [22–25]: $D = 0.94\lambda/\beta \cos\theta$. Here D, λ, β, and θ are the grain size, beam wavelength (0.15405 nm), FWHM, and diffraction angle of the XRD measurement, respectively. In Table 2, the lattice parameters a and c were calculated through the Bragg Diffraction equation ($2d \sin\theta = n\lambda$) and the lattice equation of the wurtzite structure (1) [22]:

$$a = d_{hkl}\sqrt{\frac{4}{3}(h^2 + hk + k^2) + l^2\left(\frac{a}{c}\right)^2},$$

$$\frac{a}{c} = \sqrt{\frac{8}{3}}. \quad (1)$$

Here d_{hkl} is the interplanar distance and h, k, l are the Miller Indices. The biaxial stress was calculated by comparing the c-lattice constant to the strain-free lattice parameter ($c_0 = 0.5205$ nm) measured from a ZnO powder sample: σ
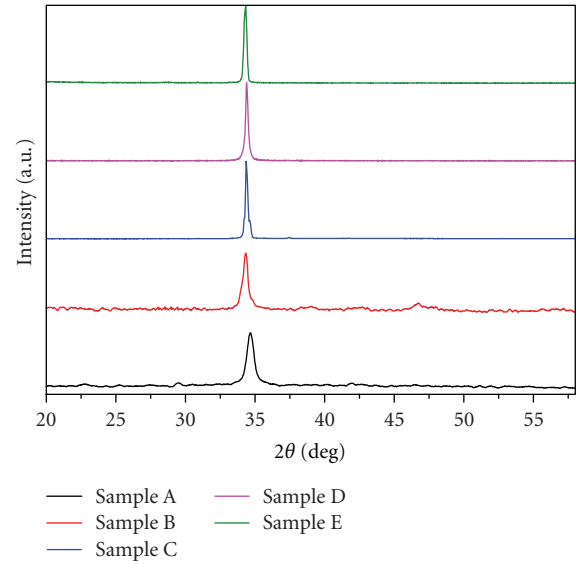

FIGURE 2: XRD ω-2θ spectra of the Samples A, B, C, D, and E.

$= -453.6 \times 10^9 [(c - c_0)/c_0]$. The strain was calculated by: $\varepsilon = \beta/4\tan\theta$ [22–24, 26].

TABLE 2: Peak position, FWHM, grain size, strain, stress, and lattice constants (d) of the samples from XRD measurements and derived lattice parameters (a, c).

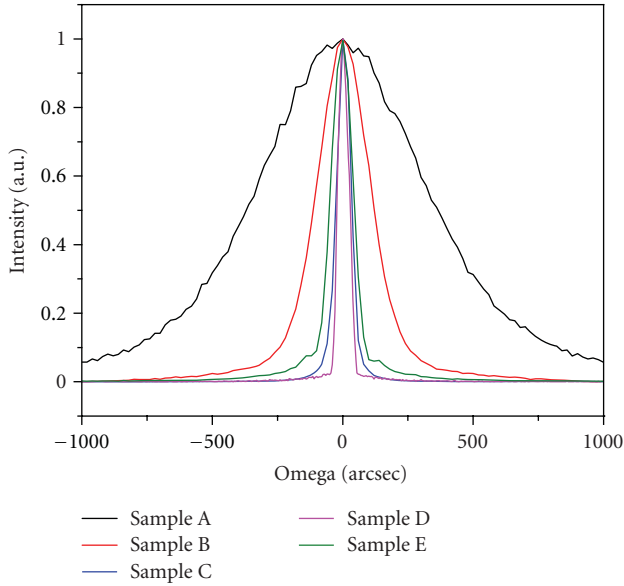| Sample	2 theta (degree)	FWHM (acrsec)	Grain size (nm)	Strain (microstrain)	Stress (Gpa)	d (Å)	a (Å)	c (Å)
A	34.68	791.74	37.872	299.624	3.306	2.584	3.164	5.167
B	34.33	242.58	123.493	90.809	−1.171	2.609	3.196	5.218
C	34.37	64.18	466.849	24.057	−0.606	2.606	3.192	5.212
D	34.41	48.66	615.805	18.261	−0.120	2.603	3.188	5.206
E	34.33	98.01	305.715	36.692	−1.145	2.609	3.195	5.218

FIGURE 3: Normalized XRC results of the Samples A, B, C, D, and E.

From these calculations the ZnO layer in Sample A suffered tensile stress of 3.306 GPa and 299.624 microstrain. The high tensile stress caused cracking during the ZnO thin film growth. In Sample B, the ZnO layer suffered compressive stress of −1.171 GPa and 90.809 microstrain. The change from tensile stress to compressive stress using GaN as a buffer layer can solve the problem of the film cracking.

Using MgO as a buffer layer (Samples C, D, and E) resulted in an increased strain release in the ZnO thin film growth. In sample D, the minimum compressive stress (−0.120 GPa) and strain (18.261 microstrain) were observed and were found to be close to the stress-free condition. These results imply that threading dislocations were effectively confined in the ZnO/MgO interface due to the cubic structure of MgO during the ZnO thin film growth [20, 21]. Sample D exhibited the highest crystalline quality ZnO thin film in this study.

4. Deep Level and Edge Band Emission

The PL spectra of the ZnO thin film samples at room temperature (Figure 4(a)) show strong edge band emissions (EBE) with very weak deep level emissions (DLE), which confirms their good crystalline and optical quality. The band-edge emission peaks of the samples are located at 3.312 eV, 3.305 eV, 3.304 eV, 3.298 eV, and 3.317 eV, for Samples A, B, C, D, and E, respectively, while the broad DLE peaks are at about 2.25 eV. The DLE results reveal the presence of defects and oxygen vacancies in the ZnO thin films [25]. In order to compare the optical quality of these samples, the integrated intensity ratio of the EBE to the DLE as a function of temperature for each of the samples is shown in Figure 4(b). The integrated intensity of EBE and DLE ranges from 2.918 eV to 3.758 eV and 1.771 eV to 2.756 eV, respectively, corresponding to the shaded areas in Figure 4(a). The EBE/DLE values decrease rapidly with increasing temperature up to some specific temperature for each of the samples. These specific temperatures are approximately 45 K, 45 K, 75 K, 90 K, and 75 K for Samples A, B, C, D, and E, respectively. Above these specific temperatures, no rapid decrease in EBE/DLE values is observed. The specific temperature represents the critical temperature below which radiative recombination dominates and above which nonradiative recombination dominates. For Sample A the low EBE/DLE values in all temperature ranges represent a higher density of threading dislocations, more stress, and higher defect density in the ZnO thin film, corresponding to the lower optical quality of the sample. The EBE/DLE values increase significantly in the samples with GaN or MgO buffer layers. These results confirm the improvement of ZnO thin film crystallinity from using GaN and MgO buffer layers. When comparing Sample E to Samples C and D, the apparently lower optical quality of Sample E originates from the stoichiometric growth condition (Zn : O₂= 1 : 1). This growth condition induces more oxygen vacancies in the ZnO layer leading to a higher DLE intensity. This order of DLE intensity for the samples is the same for the entire temperature range.

In order to check the consistency between the optical measurements and structural measurements, the integrated intensity ratio of the EBE to the DLE and the inverse FWHM of the XRC of each samples are shown in Figure 5. The maximum EBE/DLE means the EBE/DLE value of sample at 10 K. Higher EBE/DLE ratios and higher values for FWHM^{-1} from XRC measurements represent improved optical and material qualities of the samples. Samples C, D, and E, with MgO buffer layers, show an enhancement of their crystalline and optical qualities. Sample B with a GaN buffer layer exhibits inferior results. Sample A without any buffer layer had the worst quality.
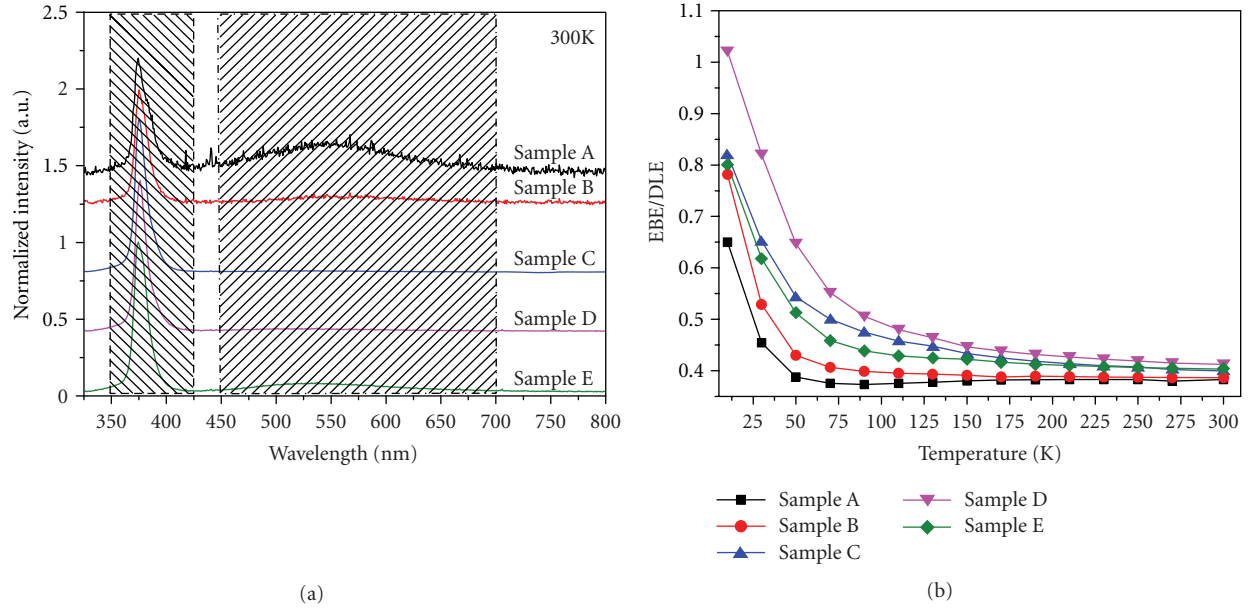
(a)

(b)

FIGURE 4: (a) Photoluminescence and deep level emission spectra of the Samples A, B, C, D, and E at room temperature, (b) the integrated intensity ratio of the EBE to the DLE of samples as functions of temperature.
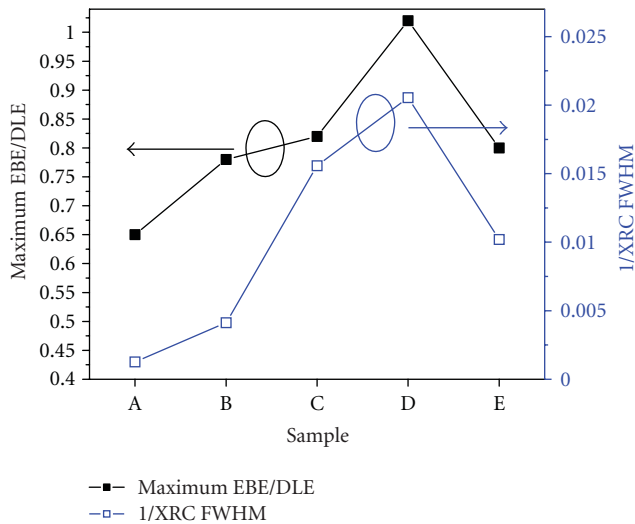

FIGURE 5: The integrated intensity ratio of the EBE to the DLE and the inverse FWHM of XRC of Samples A, B, C, D, and E.

5. SEM and AFM Images

Figures 6(a) and 6(b) show SEM and AFM images of Samples A and D. In the SEM image of Sample A (Figure 6(a)), surface pits can be seen. The rougher surface of Sample A compared to Sample D originates from the larger lattice mismatch in the ZnO/sapphire interface. The large tensile stress in Sample A is induced by this increased lattice mismatch. AFM measurement reveals a larger root mean square (RMS) roughness of about 6.982 nm without a buffer layer. For the MgO buffer layer in sample D, the RMS roughness is about 2.875 nm. The decrease in RMS roughness by 58.8% is attributed to the change from tensile stress to compressive stress when using the MgO buffer layer compared to no buffer layer. These results indicate that the growth of ZnO thin films on buffer layers, especially MgO, results in better crystallinity of samples, thus improved optical characteristics.

In summary, by including a buffer layer in the growth of ZnO thin films, the lattice mismatch of the film surface to the sapphire substrate surface was decreased significantly. Including a GaN buffer layer in Sample B resulted in higher optical and structural quality than Sample A. The comparison between ZnO growth on the GaN and the MgO buffer layers shows that dislocations stretching along the c-axis could not be suppressed effectively by a thick GaN buffer layer. Samples C, D, and E were of higher quality than sample B.

For the MgO buffer layer growth, the stoichiometric growth condition induced more oxygen vacancies in the ZnO layer, resulting in lower crystal quality in Sample E compared to Samples C and D. In the two-step temperature variation growth, the optimal LT-ZnO thickness was about 40 nm for Sample D [11], which showed the highest crystallinity in this study. Thus, the LT-ZnO has an important effect in changing the crystal quality of the following HT-ZnO. The LT-ZnO with optimal thickness could cause relatively disordered HT-ZnO growth on the MgO buffer layer resulting in a three-dimensional island morphology, resulting in different defect configurations in the HT-ZnO layer [11]. From the description above, one can see that the order of ZnO thin film crystallinity, from best to worst, is D, C, E, B, and A.

6. Conclusion

In conclusion, the influence of the GaN and MgO buffer layers on the structural, electrical, and optical properties
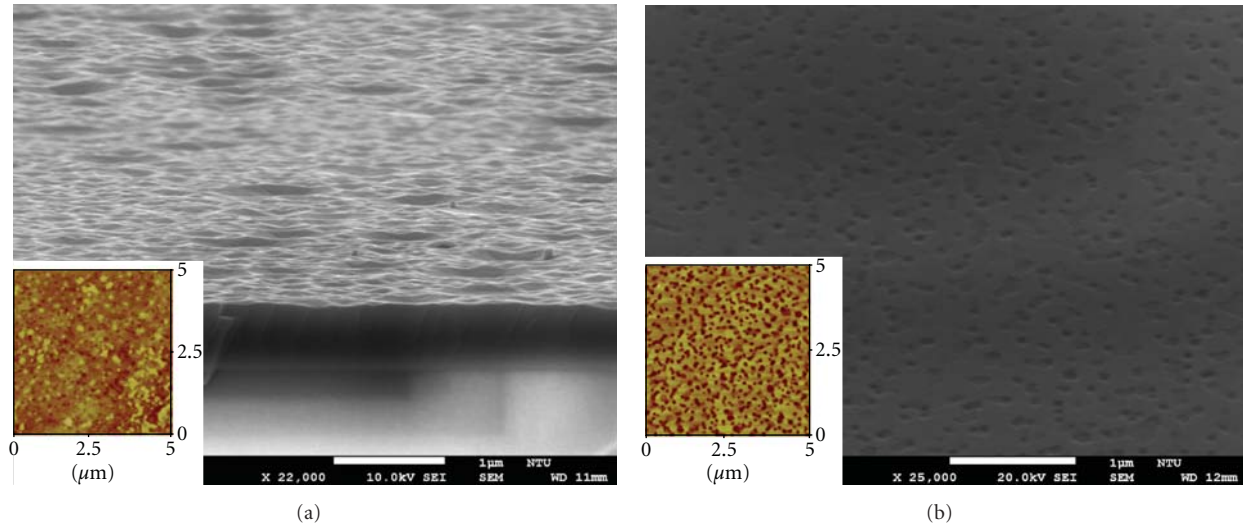
FIGURE 6: SEM and AFM images of (a) Sample A and (b) Sample D.

of ZnO thin films grown on sapphire substrates by MBE was investigated. The XRD and XRCs investigations revealed that the buffer layer had diminished the strain and changed the stress from tensile to compressive, leading to threading dislocation elimination. The PL revealed a strong edge band emission with a weak deep level emission, suggesting the good crystalline quality of the ZnO thin films on the MgO buffer layer. The increase in the integrated intensity ratio of the EBE to the DLE and the inverse FWHM of XRC with GaN and MgO as buffer layers demonstrated the enhancement of the structural and optical qualities of the ZnO thin films.

Acknowledgments

References

[1] D. C. Look, "Recent advances in ZnO materials and devices," *Materials Science and Engineering B*, vol. 80, no. 1–3, pp. 383–387, 2001.

[2] D. M. Bagnall, Y. F. Chen, Z. Zhu et al., "Optically pumped lasing of ZnO at room temperature," *Applied Physics Letters*, vol. 70, no. 17, pp. 2230–2232, 1997.

[3] J. H. Lim, C. K. Kong, K. K. Kim, I. K. Park, D. K. Hwang, and S. J. Park, "UV electroluminescence emission from ZnO light-emitting diodes grown by high-temperature radiofrequency sputtering," *Advanced Materials*, vol. 18, no. 20, pp. 2720–2724, 2006.

[4] S. Liang, H. Sheng, Y. Liu, Z. Huo, Y. Lu, and H. Shen, "ZnO Schottky ultraviolet photodetectors," *Journal of Crystal Growth*, vol. 225, no. 2–4, pp. 110–113, 2001.

[5] M. Law, L. E. Greene, J. C. Johnson, R. Saykally, and P. Yang, "Nanowire dye-sensitized solar cells," *Nature Materials*, vol. 4, no. 6, pp. 455–459, 2005.

[6] Q. Wan, Q. H. Li, Y. J. Chen et al., "Fabrication and ethanol sensing characteristics of ZnO nanowire gas sensors," *Applied Physics Letters*, vol. 84, no. 18, pp. 3654–3656, 2004.

[7] Y. Zhang, G. Du, D. Liu et al., "Crystal growth of undoped ZnO films on Si substrates under different sputtering conditions," *Journal of Crystal Growth*, vol. 243, no. 3-4, pp. 439–443, 2002.

[8] S. K. Hong, H. J. Ko, Y. Chen, and T. Yao, "Control of ZnO film polarity," *Journal of Vacuum Science and Technology B*, vol. 20, no. 4, pp. 1656–1663, 2002.

[9] T. Gruber, C. Kirchner, K. Thonke, R. Sauer, and A. Waag, "MOCVD growth of ZnO for optoelectronic applications," *Physica Status Solidi A*, vol. 192, no. 1, pp. 166–170, 2002.

[10] M. Fujita, N. Kawamoto, T. Tatsumi, K. Yamagishi, and Y. Horikoshi, "Molecular beam epitaxial growth of ZnO on Si substrate using ozone as an oxygen source," *Japanese Journal of Applied Physics Part 1*, vol. 42, no. 1, pp. 67–70, 2003.

[11] J. G. Kim, S. K. Han, S. M. Yang et al., "Effects of low temperature ZnO and MgO buffer thicknesses on properties of ZnO films grown on (0001) Al2O3 substrates by plasma-assisted molecular beam epitaxy," *Thin Solid Films*, vol. 519, no. 1, pp. 223–227, 2010.

[12] Y. J. Chen, Y. Y. Shih, C. H. Ho, J. H. Du, and Y. P. Fu, "Effect of temperature on lateral growth of ZnO grains grown by MOCVD," *Ceramics International*, vol. 36, no. 1, pp. 69–73, 2010.

[13] X. Q. Wang, H. P. Sun, and X. Q. Pan, "Effect of GaN interlayer on polarity control of epitaxial ZnO thin films grown by molecular beam epitaxy," *Applied Physics Letters*, vol. 97, no. 15, Article ID 151908, 2010.

[14] B. Pecz, A. El-Shaer, A. Bakin, A. C. Mofor, A. Waag, and J. Stoemenos, "Structural characterization of ZnO films grown by molecular beam epitaxy on sapphire with MgO buffer," *Journal of Applied Physics*, vol. 100, no. 10, Article ID 103506, 2006.

[15] A. A. Ashrafi, A. Ueta, H. Kumano, and I. Suemune, "Role of ZnS buffer layers in growth of zincblende ZnO on GaAs substrates by metalorganic molecular-beam epitaxy," *Journal of Crystal Growth*, vol. 221, no. 1–4, pp. 435–439, 2000.

[16] Z. D. Sha, J. Wang, Z. C. Chen et al., "Initial study on the structure and optical properties of ZnO film on Si(1 1 1) substrate with a SiC buffer layer," *Physica E*, vol. 33, no. 1, pp. 263–267, 2006.

[17] B. M. Ataev, W. V. Lundin, V. Mamedov, A. M. Bagamadova, and E. E. Zavarin, "Low-pressure chemical vapour deposition growth of high-quality ZnO films on epi-GaN/α-Al2O3," *Journal of Physics Condensed Matter*, vol. 13, no. 9, pp. L211–L214, 2001.

[18] J. P. Cui, Y. Duan, X. F. Wang, and Y. P. Zeng, "Strain status in ZnO film on sapphire substrate with a GaN buffer layer grown by metal-source vapor phase epitaxy," *Microelectronics Journal*, vol. 39, no. 12, pp. 1542–1544, 2008.

[19] A. Bakin, J. Kioseoglou, B. Pecz et al., "Misfit reduction by a spinel layer formed during the epitaxial growth of ZnO on sapphire using a MgO buffer layer," *Journal of Crystal Growth*, vol. 308, no. 2, pp. 314–320, 2007.

[20] Y. Chen, H. J. Ko, S. K. Hong, and T. Yao, "Layer-by-layer growth of ZnO epilayer on Al2O3(0001) by using a MgO buffer layer," *Applied Physics Letters*, vol. 76, no. 5, pp. 559–561, 2000.

[21] Y. Chen, S. K. Hong, H. J. Ko et al., "Effects of an extremely thin buffer on heteroepitaxy with large lattice mismatch," *Applied Physics Letters*, vol. 78, no. 21, pp. 3352–3354, 2001.

[22] P. Singh, A. Kumar, Deepak, and D. Kaur, "ZnO nanocrystalline powder synthesized by ultrasonic mist-chemical vapour deposition," *Optical Materials*, vol. 30, no. 8, pp. 1316–1322, 2008.

[23] W. Taeg Lim and C. Hyo Lee, "Highly oriented ZnO thin films deposited on Ru/Si substrates," *Thin Solid Films*, vol. 353, no. 1, pp. 12–15, 1999.

[24] J. Ye, S. Gu, S. Zhu et al., "The growth and annealing of single crystalline ZnO films by low-pressure MOCVD," *Journal of Crystal Growth*, vol. 243, no. 1, pp. 151–156, 2002.

[25] B. H. Kong, D. C. Kim, S. K. Mohanta, and H. K. Cho, "Influence of VI/II ratios on the growth of ZnO thin films on sapphire substrates by low temperature MOCVD," *Thin Solid Films*, vol. 518, no. 11, pp. 2975–2979, 2010.

[26] D. Sahu, B. S. Acharya, and A. K. Panda, "Role of Ag ions on the structural evolution of nano ZnO clusters synthesized through ultrasonication and their optical properties," *Ultrasonics Sonochemistry*, vol. 18, no. 2, pp. 601–607, 2011.

Review Article

Luminescence Properties of Si Nanocrystals Fabricated by Ion Beam Sputtering and Annealing

Sung Kim,[1] Dong Hee Shin,[1] Dong Yeol Shin,[1] Chang Oh Kim,[1] Jae Hee Park,[1] Seung Bum Yang,[1] Suk-Ho Choi,[1] Seung Jo Yoo,[2] and Jin-Gyu Kim[2]

[1] *Department of Applied Physics, College of Applied Science, Kyung Hee University, Yongin 446-701, Republic of Korea*
[2] *Division of Electron Microscopic Research, Korea Basic Science Institute, 113 Gwahangno, Yusong-gu, Daejeon 305-333, Republic of Korea*

Correspondence should be addressed to Suk-Ho Choi, sukho@khu.ac.kr

During the past several decades, Si nanocrystals (NCs) have received remarkable attention in view of potential optoelectronic device applications. This paper summarizes recent progress in the study of luminescence from Si NCs, such as photoluminescence (PL), cathodoluminescence, time-solved PL, and electroluminescence. The paper is especially focused on Si NCs produced by ion beam sputtering deposition of SiO_x single layer or SiO_x/SiO_2 multilayers and subsequent annealing. The effects of stoichiometry (x) and thickness of SiO_x layers on the luminescence are analyzed in detail and discussed based on possible mechanisms.

1. Introduction

Light-emitting silicon nanocrystals (Si NCs) have attracted considerable attention since the first report on photoluminescence (PL) of porous Si in 1990 [1] was published as an effort to build Si-based photonics. Besides fundamental physics related to quantum-confinement effect (QCE) in an indirect-gap semiconductor, Si [2–5], there have been intensive studies on novel interesting phenomena such as light emission from electrically excited Si NCs or quantum dots (QDs) [6–9] and energy transfer to Er^{3+} ions [10–12], highly potential for optoelectronics applications. For realizing the device applications as well as for clarifying the origin of the observed luminescence, tight size control of Si NCs should be essential.

Si NCs can be synthesized by a number of techniques: ion implantation of Si into SiO_2 matrix [5, 13, 14], deposition of substoichiometric oxide films using chemical vapour deposition (CVD) [8, 9, 15], RF sputtering [12, 16], and reactive evaporation [17]. Most of these methods should be followed by thermal annealing procedures inducing phase separation/crystallization. The synthesized Si NCs usually have a relatively broad size distribution, which can

complicate the characterization of Si NCs based on QCE and therefore is undesirable for the device applications. Ion beam sputtering deposition (IBSD) under oxygen ambient has been reported to be useful for the growth of the stoichiometric/substoichiometric oxide films [18]. This method has an advantage of providing relatively low-thermal budget, thereby producing uniform oxide films over the full depth and rendering their interface-free examination. In addition, in situ X-ray photoelectron spectroscopy (XPS) analysis during IBSD, because it enables looking into the oxidation/growth processes, is a powerful method to check the change of the chemical states on the top surface of the films.

Although Si NCs embedded in the SiO_2 exhibit efficient and tunable PL emission by changing the oxygen content (or NC size), the origin of the light emission is still under debate [19–21]. Discussions are mainly focused on whether the light emission is generated by the excitonic transitions inside Si NCs or by other defect-related centers. As reported previously, Si NCs formed in host materials such as SiO_2 have a broad distribution of size and orientation and a lot of oxygen-related defect centers exist at the interfaces of Si NCs/SiO_2 [3–5]. This explains why PL spectra of such materials have typically broad emission bands [20, 22]. The

Si=O or Si–O bonds are known to exist in the Si NCs/SiO$_2$ interfaces, which significantly reduce the effective optical band gap by creating localized states and pinning the band gap of Si NCs, resulting in the PL peak shift smaller than expected from QCE [23–25].

Even though there have been some technological advances in producing Si-NC-based light emitting diodes (LEDs) in the form of a metal oxide semiconductor (MOS LEDs) [6, 25, 27], no breakthrough for the efficient devices has been reported yet. One of the main obstacles in the production of efficient MOS LEDs is the problem of carrier injection into the insulating oxide matrix. Several models have been proposed for explaining the carrier injection processes, which are still in controversy. In addition to studies on electroluminescence (EL) as well as on PL, those on their correlations are especially needed for understanding the mechanisms of charge injection and light generation, thereby clarifying the operation principles of MOS LEDs.

In this paper, we review luminescence properties of Si NCs studied by continuous-wave/time-resolved PL, cathodoluminescence (CL), and EL spectroscopies and discuss their size-dependent correlations based on possible light-emitting mechanisms.

2. Experimental Details

SiO$_x$ single-layer (SL) films of 2 $\sim$ 200 nm and SiO$_x$/SiO$_2$ multilayers (MLs) with 50 periods of 2 nm thin layers were grown on n-type (100) Si wafers at room temperature (RT) using an Ar$^+$ beam with an ion energy of 750 eV and a Si target under oxygen atmosphere in a reactive IBSD system with a Kaufman-type DC ion gun. The relative film thickness was controlled from the growth rate calibrated by transmission electron microscopy (TEM) measurements of thin films grown within a given time. The deposition chamber was evacuated to a pressure of 5.0×10^{-9} torr before introducing argon gas into the system. Details of the system are described elsewhere [18]. The stoichiometry of the SiO$_x$ films could be analyzed and controlled with in situ XPS using Al $k\alpha$ line of 1486.6 eV. A stoichiometric SiO$_2$ thin film was used as a reference for the determination of the relative sensitivity factors of Si 2p and O 1s peaks. The B doping of the SiO$_x$ layers was achieved by cosputtering using a combination target where a small boron chip was fixed on a p-type Si wafer. The doping concentration was controlled by varying the size of the boron chip. The doping level of the SiO$_x$ layers was estimated by secondary ion mass spectroscopy (Cameca, model IMS-7f) using an oxygen-ion beam of 5 keV. The quantification of the B-doped SiO$_x$ layers was performed using a B-implanted certified reference material. After deposition, the samples were annealed at 1100°C in an ultrapure nitrogen ambient by using a horizontal furnace to form Si NCs in the layers. In order to passivate Si dangling bonds, some of the samples were hydrogenated by heating the samples at 650°C for 60 min under H$_2$ flow.

PL spectra were measured at RT using the 325 nm line of a HeCd laser as the excitation source. Emitted light was collected by a lens and analysed using a grating monochromator and a GaAs photomultiplier (PM) tube. Standard lock-in

detection techniques were used to maximize the signal-to-noise ratio. The laser beam diameter was about 0.3 mm and the power was about 3 mW. The excitation for time-resolved PL was done by a pulsed Nd:YAG laser (wavelength: 355 nm, pulse energy density: 0.6 mJ/cm^2, repetition frequency: 20 Hz, and pulse duration: 20 ps). The emitted light was analyzed by using a monochromator equipped with a gated intensified charge-coupled device (CCD) (detection energy: 1.38 $\sim$ 9.92 eV and response time: 40 ps, PI-Max, Princeton Instrument) triggered by exciting laser pulse. CL spectra were measured in the range of electron beam energies of 1 to 20 kV by using a JEOL 6330F field emission scanning electron microscope equipped with an Oxford Instrument Mono CL2. The CL spectra were dispersed by a 1200 lines/mm grating blazed at 500 nm and detected using a Hamamatsu R943-02 peltier-cooled PM tube. The current-voltage (I-V) curves of the LED devices were measured using Keithley 237 high-voltage source meter. For forward-bias conditions, positive voltages were applied to the Al contacts on the poly-Si layers of LED devices. The RT EL measurements were performed under forward bias by using DM 500 grating monochromator equipped with a Si CCD for light detection.

3. Results and Discussion

3.1. Continuous-Wave Photoluminescence. Figure 1(a) shows thickness dependence of the PL spectra for Si-NC SLs with $x = 1.4$. The major PL band in the range of 765 to 850 nm has been widely observed and attributed to the radiative recombination of quantum-confined electrons and holes in Si NCs [14, 21]. The PL spectra are redshifted monotonically with increasing the SiO$_x$ thickness (d) due to the size increase of Si NCs in thicker samples. Previously, it has been similarly reported that larger NCs grow in thicker SiO$_x$ [28]. Figure 1(b) summarizes the PL peak shift as a function of d at each x. For $x \leq 1.2$, the PL peaks show a rather confusing behavior, that is, weak blueshifts with increasing d. For $x \geq 1.4$, the PL peaks show monotonic redshifts as d increases, consistent with QCE.

A few nm thick natural SiO$_2$ is usually formed on the surface of the SiO$_x$ layer after deposition, thereby reducing the real thickness of SiO$_x$. During annealing, the NC size could be strongly influenced by the mixing of SiO$_x$ with SiO$_2$, which exists at the bottom interface of the SiO$_x$ layer/Si wafer as well as on the top surface of SiO$_x$, resulting in an increase of x value [19]. This is reasonable because the mixing during annealing can occur within a diffusion distance of Si in SiO$_x$ matrix that was reported to be as long as about 3 nm [29]. The SiO$_2$ layer would make a stronger effect on the stoichiometry of thinner SiO$_x$ layer. These considerations can explain why the PL peaks are located at smaller wavelengths in the samples with thinner SiO$_x$ layers, as shown in Figure 1(b).

It is possible to independently control NC size/density by employing a technique of ML growth for Si NCs [21, 28, 30]. The layer thickness/excess Si content of Si-rich oxide (SiO$_x$) in the ML structures of SiO$_x$/SiO$_2$ determines the NC size/density, respectively, after high-temperature
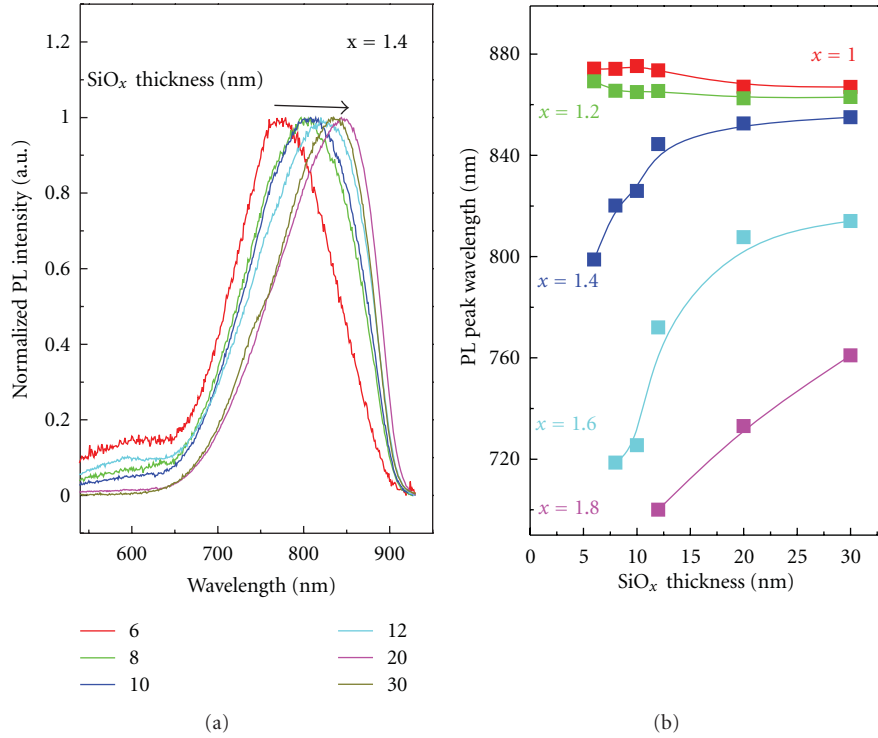
FIGURE 1: (a) SiO$_x$-layer-thickness-dependent PL spectra for single-layer (SL) Si NCs with $x = 1.4$. (b) PL peak shifts as functions of SiO$_x$-layer thickness at each x [21, 26].
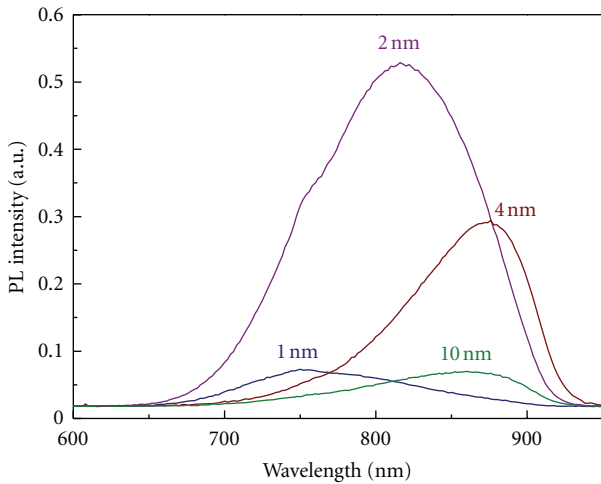

FIGURE 2: PL spectra of SiO$_x$/SiO$_2$ MLs after annealing at 1100°C for various thicknesses of the SiO$_x$ layer [21].

annealing. This approach can make it possible to engineer the energy of the band gap of Si NCs by optimizing the thickness/composition in the ML structures of Si NC/SiO$_2$. Figure 2 shows RT PL spectra of SiO$_x$/SiO$_2$ MLs after annealing for various thicknesses of the SiO$_x$ layer. The PL spectra are blueshifted with decreasing d, with their maximum intensity at $d = 2$ nm.

Figure 3(a) shows a cross-sectional high-resolution TEM (HRTEM) image of 50-period 2 nm SiO$_{1.0}$/2 nm SiO$_2$ MLs

after annealing at 1100°C, in which the ML structure and the phase separation are clearly observed. Using full-size HRTEM images, the average size and density of the Si NCs are estimated to be $\sim 3.8 \pm 0.8$ nm and 3.5×10^{12} cm^{-2}, respectively. Figure 3(b) compares full widths at half maximum (FWHMs) of PL spectra between ML and SL samples ($x = 1.0$) with the same total thickness of 200 nm. The PL spectra of both samples are almost identically peaked at around 860 nm (1.44 eV), in agreement with the estimated recombination energy for quantum-confined excitons in a ~3.5 nm diameter Si NCs [28]. The PL FWHM (70 nm) of ML sample is much smaller than that of SL sample (103 nm), indicating more-uniform-size distribution of Si NCs in ML samples, still valid for other x values, as shown in Figure 3(c). Figure 3(c) also shows the size-dependent PL peak shifts consistent with QCE for both samples.

3.2. Cathodoluminescence. It is hard to interpret the CL spectra of Si NCs based on the QCE effect because the CL emissions are sometimes mixed with those from the interface or surface defect states in the similar energy ranges [31, 32]. Recently, CL spectra of Si nanoparticles below 3 nm in porous Si have given an evidence of the CL light emission in the UV range from ultrasmall Si NCs [32]. In our previous work, a CL emission at 2.16 eV (574 nm) has been ascribed to 3.5 nm Si NCs formed in Al$_2$O$_3$ by ion implantation [33]. Figure 4(a) shows CL spectra of Si-NC MLs at each x after hydrogenation, which were measured by using an electron beam energy of 15 keV at 77 K. Two major CL bands are
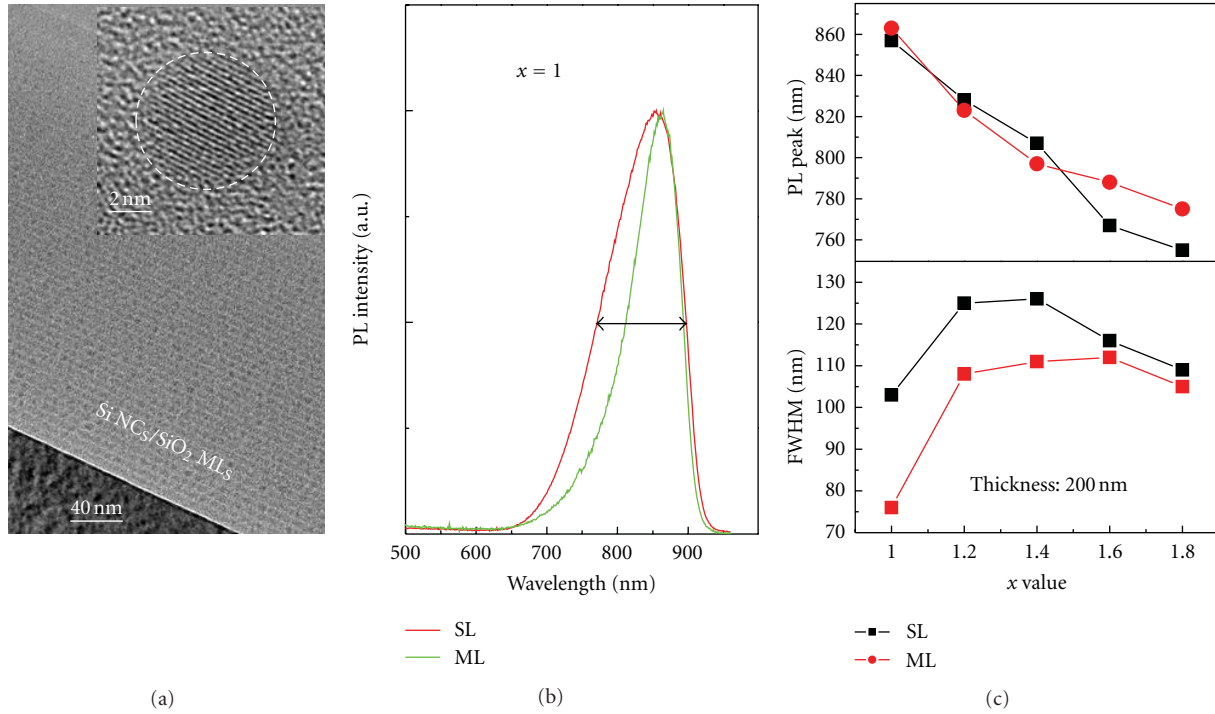
FIGURE 3: (a) Cross-sectional HRTEM image of 50-period 2 nm $SiO_{1.0}$/2 nm SiO_2 MLs after annealing at $1100°C$. (b) FWHMs of normalized PL spectra for ML and SL samples with the same total thickness of 200 nm. (c) Size-dependent PL peak energy and FWHMs of ML and SL samples.
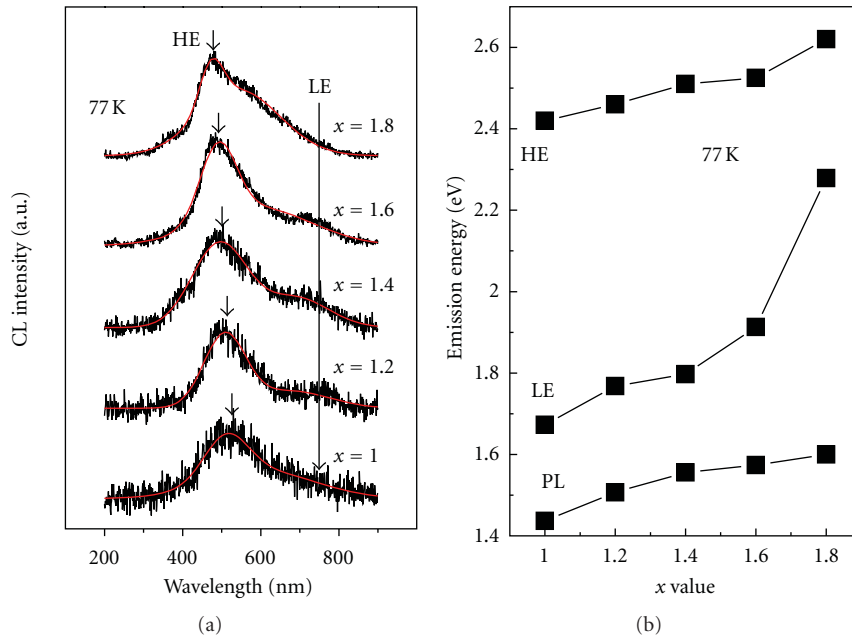

FIGURE 4: (a) CL spectra of the ML Si NCs at each x after hydrogenation. (b) Energy shifts of the deconvoluted CL (HE and LE) and PL bands as functions of x [22].

observed at ~ 1.66 eV (750 nm) and ~ 2.18 eV (570 nm) at $x = 1.0$, which are named low-energy (LE) and high-energy (HE) bands, respectively. The CL spectra were deconvoluted into two Gaussian bands in order to find peak positions of the HE and LE bands accurately. Figure 4(b) compares energy shifts of the deconvoluted CL bands with those of PL band as functions of x. The HE (LE) CL band is blueshifted from 2.18 (1.66) to 2.64 (2.16) eV, respectively, as x increases from 1.0 to 1.8. The total energy shift of the CL bands is more than two times as large as that of the PL band.
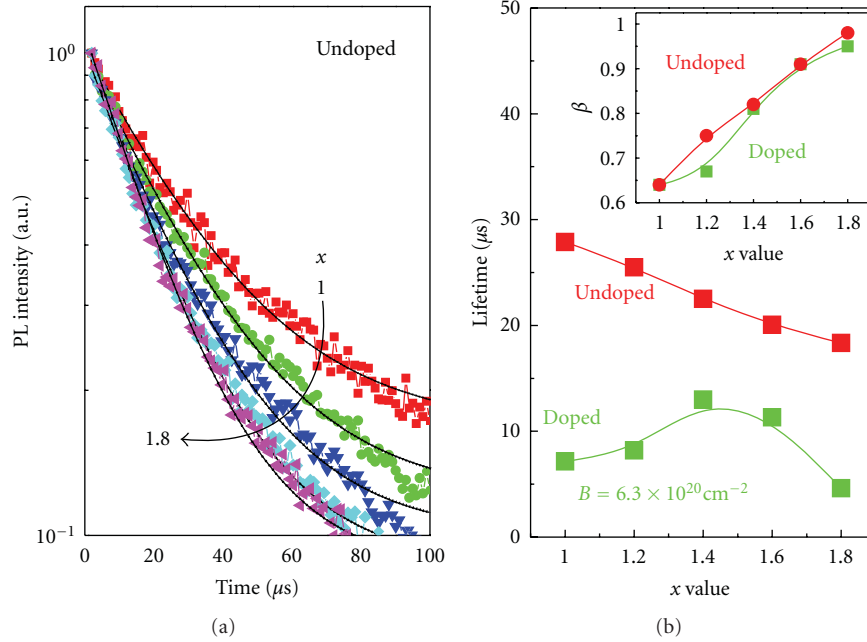
(a)

(b)

FIGURE 5: (a) PL decay curves of undoped ML Si NCs at 300 K for various x values. (b) Lifetimes as functions of x for undoped and B-doped Si NCs. The inset shows β values as functions of x for both samples.

The CL spectra exhibit very different behaviors at 300 K [22]. A new strong CL band appears at about 2.70 eV (460 nm) without almost any energy shift with x. The 2.70 eV peak has been attributed to amorphous SiO_2 defects in porous Si [31] or localized defects at the Si/SiO_2 interface [31, 32]. The HE band still remains at around 2.39 eV (520 nm) even in the 300 K spectra, but no peak shift with x is seen due to the dominant effect of the defect CL band. At 77 K, the defect CL band disappears, as shown in Figure 4(a), consistent with the observation that the defect-related CL band is reduced at lower temperature [31]. These results suggest that the CL band originating from Si NCs can be well analyzed at low temperature and reflect the size dependence of the peak shifts better than the PL band.

3.3. Time-Resolved Photoluminescence. The carrier relaxation and dynamics by state filling and migration [26, 34–36] are interesting phenomena involved in the light-emission processes of semiconductor nanostructures. The state-filling effect of Si NCs has been studied for discussing the parabolic confinement of Si NCs and the energy splitting between the energy levels [36]. Migration of the excitons between neighboring Si NCs has been shown to influence their optical properties [35, 36]. The migration process involves thermalization of the excitons, meaning the migration of excitons into the energetically most favorable low-energy states.

Figure 5(a) shows PL decay curves of undoped Si-NC MLs at 300 K. PL decay traces were measured for x values in the range of 1.0 to 1.8 and well fitted to a stretched exponential function, $I(t) = I_0 \exp[-(t/\tau_{PL})^\beta]$ [4, 18–20], where I_0 is the PL intensity at $t = 0$, τ_{PL} the effective PL lifetime, and β the dispersion factor having a value between

0 and 1. τ_{PL} for each x was obtained by fitting the decay traces taken at the peak wavelength in the PL spectra. The fitted results are drawn by solid lines in Figure 5(a). Figure 5(b) summarizes the variations of the lifetimes as functions of x for undoped and B-doped Si NCs. The lifetime of undoped Si NCs increases monotonically with decreasing x. The lifetime of B-doped Si NCs increases from 4.6 to 13.0 μs as x varies from 1.8 to 1.4, but by further decrease of x, it decreases.

As previously reported for undoped Si NCs by us [26, 34], the PL lifetime as well as the PL radiative lifetime showed monotonically increasing behaviors with increasing the size of NCs (decreasing x), possibly due to the reduction in the relative portion of the interface states between SiO_2 and NCs in the samples containing larger Si NCs [22]. In contrast, in doped Si NCs, the PL lifetime decreases with decreasing x (increasing the NC size) below 1.4, as shown in Figure 5(b), resulting from the increase of optically less active NCs by the increase of NCs containing more dopants at larger NC sizes. Optically less active NCs would affect the lifetime of neighboring NCs by the effect of coupling between the closely packed NCs [26], resulting in a reduction of the lifetime in the latter.

The inset of Figure 5(b) compares x-dependent β values for undoped and B-doped NCs, both of which show similar monotonic increasing behaviors with increasing x. The stretched line shape of the PL decay originates from a system of interacting Si NCs in which migration of excitons occurs [26, 36]. The dispersion factor β indicates a measure of the migration process [37]. For totally isolated NCs, β approaches 1, indicating a single exponential time decay of their PL signal. At smaller x (larger NCs), some interference is expected between adjacent NCs by tunneling of excitons
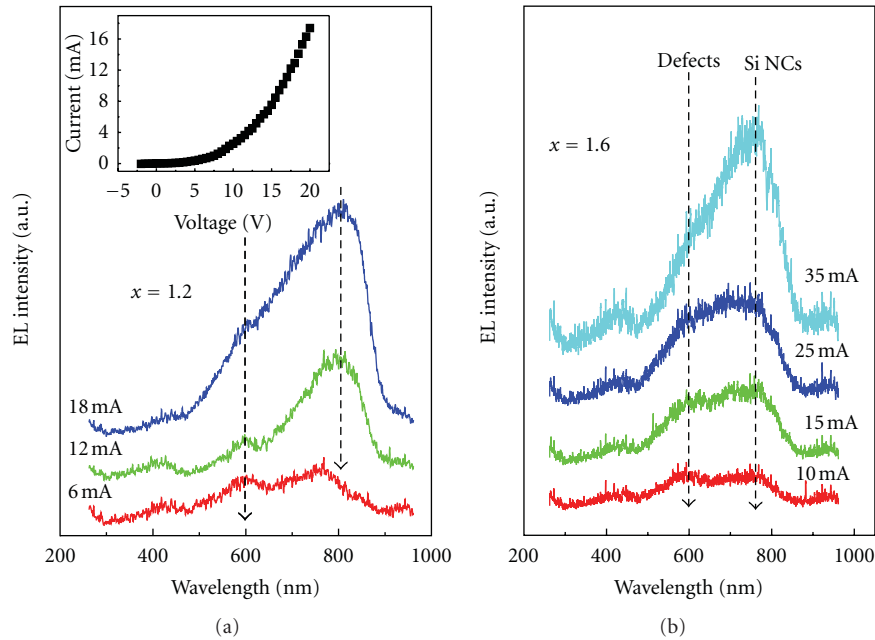
Figure 6: (a) EL spectra of a LED device containing Si NC MLs with $x = 1.2$ for various injection currents. The inset shows the I-V curve. (b) EL spectra of a LED device with $x = 1.6$ for various injection currents.

through the thin oxide between NCs, affecting the degree of exciton localization. Smaller NCs are more distant, resulting in stronger localization of excitons, thereby increasing β with increasing x, as shown in the inset of Figure 5(b). These results also suggest that doping would not affect the size-dependent behaviors of the exciton migration.

3.4. Electroluminescence. For fabricating MOS-LEDs [37, 38], 200 nm thick Si-NC MLs were formed on p$^+$-type Si wafers as a dielectric layer. A highly n$^+$-type 50 nm thick poly-Si layer was deposited on top of the Si-NC MLs by low-pressure CVD. The poly-Si layer would improve the efficiency of electron injection into Si NCs in the oxide layer. Then, a circular area of 0.3 mm in diameter was defined for the active area of the device by using standard photolithography. Finally, Al-based contacts defined as circular rings were fabricated on the polysilicon film and the Si substrate. The wide central area of the device is metal free to allow the exit of the light.

Figure 6(a) shows EL spectra of a typical LED device containing Si-NC MLs with $x = 1.2$ for various injection currents. The EL emission band originating from Si NCs is observed at around 800 nm, which is smaller than the PL peak wavelength, as shown in Figure 3(c). The EL peak wavelength shows no clear injection current dependence. Another EL band appears at around 600 nm, which is thought to originate from defect states at the interfaces of Si NCs/SiO$_2$ or SiO$_2$/Si substrate [6, 9]. The LED devices were also fabricated for various sizes of Si NCs by varying x value. Figure 6(b) shows a typical blueshift of the EL peak at $x = 1.6$ due to the size reduction of Si NCs. In contrast, the defect-related EL peak is almost fixed at around 600 nm, irrespective of the size variation of Si NCs. All LED devices showed good rectifying behaviors, as shown in the inset of Figure 6(a).

4. Conclusion

SiO$_x$ SL films and SiO$_x$/SiO$_2$ MLs were grown on n-type Si wafers by IBSD. The B doping of the SiO$_x$ layers was achieved by cosputtering using a combination target of a p-type Si wafer with a small boron chip on its center. The samples were annealed at 1100°C under nitrogen ambient to form Si NCs in the SiO$_x$ layers. The size of Si NCs and corresponding PL peak energy were strongly dependent on the thickness of the SiO$_x$ layer as well as its stoichiometry. The MLs shown to be more uniform in size than the SLs were turned out to be more useful for the characterization of Si NCs based on QCE and their device applications. The CL band originating from Si NCs could be well analyzed at low temperature and reflected the size dependence of the peak shifts better than the PL band. B doping of Si NCs resulted in the reduction of PL lifetime for larger NCs, possibly due to the increase of optically less active NCs. The decay traces of time-resolved PL spectra reflected the size dependence of the exciton migration, which was not influenced by B doping of Si NCs. The properties of EL from LEDs containing Si NC MLs were shown to be consistent with QCE by varying their size.

Acknowledgments

References

[1] L. T. Canham, "Silicon quantum wire array fabrication by electrochemical and chemical dissolution of wafers," *Applied Physics Letters*, vol. 57, no. 10, pp. 1046–1048, 1990.

[2] D. Kovalev, H. Heckler, M. Ben-Chorin, G. Polisski, M. Schwartzkopff, and F. Koch, "Breakdown of the k-conservation rule in Si nanocrystals," *Physical Review Letters*, vol. 81, no. 13, pp. 2803–2806, 1998.

[3] S. Godefroo, M. Hayne, M. Jivanescu et al., "Classification and control of the origin of photoluminescence from Si nanocrystals," *Nature Nanotechnology*, vol. 3, no. 3, pp. 174–178, 2008.

[4] M. L. Brongersma, P. G. Kik, A. Polman, K. S. Min, and H. A. Atwater, "Size-dependent electron-hole exchange interaction in Si nanocrystals," *Applied Physics Letters*, vol. 76, no. 3, pp. 351–353, 2000.

[5] L. Pavesi, L. Dal Negro, C. Mazzoleni, G. Franzò, and F. Priolo, "Optical gain in silicon nanocrystals," *Nature*, vol. 408, no. 6811, pp. 440–444, 2000.

[6] M. Wang, X. Huang, J. Xu, W. Li, Z. Liu, and K. Chen, "Observation of the size-dependent blueshifted electroluminescence from nanocrystalline Si fabricated by KrF excimer laser annealing of hydrogenated amorphous silicon/amorphous-SiN$_X$:H superlattices," *Applied Physics Letters*, vol. 72, no. 6, pp. 722–724, 1998.

[7] K.-Y. Cheng, R. Anthony, U. R. Kortshagen, and R. J. Holmes, "High-efficiency silicon nanocrystal light-emitting devices," *Nano Letters*, vol. 11, no. 5, pp. 1952–1956, 2011.

[8] A. Anopchenko, A. Marconi, M. Wang, G. Pucker, P. Bellutti, and L. Pavesi, "Graded-size Si quantum dot ensembles for efficient light-emitting diodes," *Applied Physics Letters*, vol. 99, no. 18, Article ID 181108, 2011.

[9] Z. Liu, J. Huang, P. C. Joshi et al., "Polarity-controlled visible/infrared electroluminescence in Si-nanocrystal/Si light-emitting devices," *Applied Physics Letters*, vol. 97, no. 7, Article ID 071112, 2010.

[10] P. G. Kik and A. Polman, "Gain limiting processes in Er-doped Si nanocrystal waveguides in SiO$_2$," *Journal of Applied Physics*, vol. 91, no. 1, pp. 534–536, 2002.

[11] P. G. Kik, M. L. Brongersma, and A. Polman, "Strong exciton-erbium coupling in Si nanocrystal-doped SiO$_2$," *Applied Physics Letters*, vol. 76, no. 17, pp. 2325–2327, 2000.

[12] I. Izeddin, D. Timmerman, T. Gregorkiewicz et al., "Energy transfer in Er-doped SiO$_2$ sensitized with Si nanocrystals," *Physical Review B*, vol. 78, no. 3, Article ID 035327, 2008.

[13] M. Perálvarez, J. Barreto, J. Carreras et al., "Si-nanocrystal-based LEDs fabricated by ion implantation and plasma-enhanced chemical vapour deposition," *Nanotechnology*, vol. 20, no. 40, Article ID 405201, 2009.

[14] M. L. Brongersma, A. Polman, K. S. Min, E. Boer, T. Tambo, and H. A. Atwater, "Tuning the emission wavelength of Si nanocrystals in SiO$_2$ by oxidation," *Applied Physics Letters*, vol. 72, no. 20, pp. 2577–2579, 1998.

[15] G. R. Lin, C. J. Lin, and C. T. Lin, "Low-plasma and high-temperature PECVD grown silicon-rich SiO$_x$ film with enhanced carrier tunneling and light emission," *Nanotechnology*, vol. 18, no. 39, Article ID 395202, 2007.

[16] H. Seifarth, R. Grötzschel, A. Markwitz, W. Matz, P. Nitzsche, and L. Rebohle, "Preparation of SiO$_2$ films with embedded Si nanocrystals by reactive r.f. magnetron sputtering," *Thin Solid Films*, vol. 330, no. 2, pp. 202–205, 1998.

[17] S. Zhang, W. Zhang, and J. Yuan, "The preparation of photoluminescent Si nanocrystal-SiO$_x$ films by reactive evaporation," *Thin Solid Films*, vol. 326, no. 1-2, pp. 92–98, 1998.

[18] K. J. Kim, D. W. Moon, S. H. Hong et al., "In situ characterization of stoichiometry for the buried SiO$_x$ layers in SiO$_x$/SiO$_2$ superlattices and the effect on the photoluminescence property," *Thin Solid Films*, vol. 478, no. 1-2, pp. 21–24, 2005.

[19] M. C. Kim, Y. M. Park, S. H. Choi, and K. J. Kim, "Photoluminescence characterization of dependence of Si-nanocrystals formation in Si-rich SiO$_x$ on thickness, oxygen content, and the existence of a SiO$_2$ cap layer," *Journal of the Korean Physical Society*, vol. 50, no. 6, pp. 1760–1763, 2007.

[20] S. Kim, M. C. Kim, S. H. Choi, K. J. Kim, H. N. Hwang, and C. C. Hwang, "Size dependence of Si 2p core-level shift at Si nanocrystal/ SiO$_2$ interfaces," *Applied Physics Letters*, vol. 91, no. 10, Article ID 103113, 2007.

[21] S. H. Hong, S. Kim, S. H. Choi et al., "Optical characterization of Si nanocrystals in Si-rich SiO$_x$ and SiO$_x$/SiO$_2$ multilayers grown by ion beam sputtering," *Journal of the Korean Physical Society*, vol. 45, no. 1, pp. 116–119, 2004.

[22] S. Kim, Y. M. Park, S. H. Choi, and K. J. Kim, "Origin of cathodoluminescence from Si nanocrystal/SiO$_2$ multilayers," *Journal of Applied Physics*, vol. 101, no. 3, Article ID 034306, 2007.

[23] X. X. Wang, J. G. Zhang, L. Ding et al., "Origin and evolution of photoluminescence from Si nanocrystals embedded in a SiO$_2$ matrix," *Physical Review B*, vol. 72, no. 19, Article ID 195313, pp. 1–6, 2005.

[24] M. V. Wolkin, J. Jorne, P. M. Fauchet, G. Allan, and C. Delerue, "Electronic states and luminescence in porous silicon quantum dots: the role of oxygen," *Physical Review Letters*, vol. 82, no. 1, pp. 197–200, 1999.

[25] A. Irrera, F. Iacona, I. Crupi et al., "Electroluminescence and transport properties in amorphous silicon nanostructures," *Nanotechnology*, vol. 17, no. 5, pp. 1428–1436, 2006.

[26] S. Kim and S. H. Choi, "Size-dependent correlation of the photoluminescence lifetime with Si suboxide states at Si nanocrystal/SiO$_2$ interfaces," *Journal of the Korean Physical Society*, vol. 52, no. 2, pp. 462–465, 2008.

[27] Y. Liu, T. P. Chen, L. Ding et al., "Influence of charge trapping on electroluminescence from Si-nanocrystal light emitting structure," *Journal of Applied Physics*, vol. 101, no. 10, Article ID 104306, 2007.

[28] M. Zacharias, J. Heitmann, R. Scholz, U. Kahler, M. Schmidt, and J. Bläsing, "Size-controlled highly luminescent silicon nanocrystals: a SiO/SiO$_2$ superlattice approach," *Applied Physics Letters*, vol. 80, no. 4, pp. 661–663, 2002.

[29] L. A. Nesbit, "Annealing characteristics of Si-rich SiO$_2$ films," *Applied Physics Letters*, vol. 46, no. 1, pp. 38–40, 1985.

[30] V. Osinniy, S. Lysgaard, V. Kolkovsky, V. Pankratov, and A. Nylandsted Larsen, "Vertical charge-carrier transport in Si nanocrystal/SiO$_2$ multilayer structures," *Nanotechnology*, vol. 20, no. 19, Article ID 195201, 2009.

[31] L. H. Abuhassan, M. R. Khanlary, P. Townsend, and M. H. Nayfeh, "Cathodoluminescence of small silicon nanoparticles under electron-beam excitation," *Journal of Applied Physics*, vol. 97, no. 10, Article ID 104314, pp. 1–5, 2005.

[32] G. Belomoin, J. Therrien, A. Smith et al., "Observation of a magic discrete family of ultrabright Si nanoparticles," *Applied Physics Letters*, vol. 80, no. 5, pp. 841–843, 2002.

[33] C. J. Park, Y. H. Kwon, Y. H. Lee et al., "Origin of luminescence from Si$^-$-implanted (1102) Al$_2$O$_3$," *Applied Physics Letters*, vol. 84, no. 14, pp. 2667–2669, 2004.

[34] S. Kim, Y. Min Park, S. H. Choi, K. Joong Kim, and D. Hoon Choi, "Temperature-dependent carrier recombination processes in nanocrystalline Si/SiO$_2$ multilayers studied by continuous-wave and time-resolved photoluminescence," *Journal of Physics D*, vol. 40, no. 5, article 005, pp. 1339–1342, 2007.

[35] S. Kim, Y. M. Park, S. H. Choi, and K. J. Kim, "Time-integrated and time-resolved photoluminescence properties of Si nanocrystal/SiO$_2$ multilayers grown by ion-beam sputtering," *Journal of the Korean Physical Society*, vol. 50, no. 3, pp. 567–570, 2007.

[36] L. Van Dao, X. Wen, M. T. T. Do et al., "Time-resolved and time-integrated photoluminescence analysis of state filling and quantum confinement of silicon quantum dots," *Journal of Applied Physics*, vol. 97, no. 1, Article ID 013501, 2005.

[37] J. Heitmann, F. Müller, L. Yi, M. Zacharias, D. Kovalev, and F. Eichhorn, "Excitons in Si nanocrystals: confinement and migration effects," *Physical Review B*, vol. 69, no. 19, Article ID 195309, 2004.

[38] A. Irrera, F. Iacona, I. Crupi et al., "Electroluminescence and transport properties in amorphous silicon nanostructures," *Nanotechnology*, vol. 17, no. 5, pp. 1428–1436, 2006.

Research Article

Hydrothermal Synthesis of β-NaYF$_4$:Yb, Er Nanocrystals with Upconversion Fluorescence Using Tetraethylene Pentamine as Chelating Ligand

Suli Wu, Yanhui Ning, and Shufen Zhang

State Key Laboratory of Fine Chemicals, Dalian University of Technology, Dalian 116024, China

Correspondence should be addressed to Suli Wu, wusuli@dlut.edu.cn

Novel chelating ligands are very significant for preparing nanocrystals with different morphologies and applications. In this paper, we directly introduced amine groups onto UCNPs by choosing a new chelating ligand tetraethylene pentamine (TEPA) to synthesis NaYF$_4$:Yb, Er through hydrothermal method. The influences of rare earth concentration, the ratio of RE/TEPA, solvent composition, and reaction time on the morphology and fluorescence intensity of the as-prepared NaYF$_4$:Yb, Er samples were systematically investigated and discussed. Field emission scanning electron microscopy (FE-SEM), powder X-ray diffraction (XRD), and upconversion luminescence spectroscopy were used to characterize the product. It was found that rare earth concentration, ratio of RE/TEPA, solvent composition, and reaction time were all responsible for the luminescent intensity and morphology.

1. Introduction

Upconversion (UC) means that the materials absorb long-waved photons to emit short-waved photons. Rare earth compounds have evoked much attention due to their novel electronic, optical, and chemical characteristics. The special 4f shell electron structure of the rare earth elements makes the upconverting nanoparticles (UCNPs) capable of converting two or more near-infrared (NIR) photons to one visible light photon via continuing electronic excitation and energy transfer processes [1]. Compared with downconversion materials quantum dots (QD), UCNPs have low toxicity to body, minimal autofluorescence, sharp absorption, and long life time [2]. These properties make them have great applications in various fields, such as biological labeling [3], illuminations [4], solar cells [5], optical storage [6], light-emitting diodes [7], drug-delivery [8], and photodynamic therapy [9]. NIR light with strong penetration ability has less harmful to cells and is safe for our bodies, so the applications of UCNPs on medicine and biological are especially important and have very bright prospects. As we know, NaYF$_4$ is the best host material for UCNPs due to the low lattice phonon energy and good thermal stability, and NaYF$_4$ doped with Yb, Er is frequently used as highly efficient upconversion materials.

Generally, the synthesis methods of UCNPs can be divided into two categories. One was thermolysis method, using long chain organic ligands as solvent and chelating ligand under very high temperature (300–340°C). Because of the high temperature of the thermolysis synthesis, few chelating ligands can be choosen. The most frequently used chelating ligand was oleic acid (OA) together with a non-coordinating solvent octadecene (ODE), which controlled the nucleation and growth as well as stabilization of the crystals in a thermolysis procedure. Other chelating ligands such as oleylamine [10], octadecylamine [11], oleamide [12], trioctylphosphine (TOP) [13], and trioctylphosphine oxide (TOPO) were also used to prepare NaYF$_4$:Yb, Er [14]. All these are high boiling point solvent, but the kinds of them are limited. The other method was hydro (solvent) thermal method. In this method, the reaction condition was relatively mild (heating temperature was generally 140–240°C), so some low boiling point ligands can be applied. However, few chelating ligands have reported to guide the crystal's growth

and control the morphology of the nanoparticles. Sodium citrate [15], ethylenediamine tetraacetate (EDTA) [16], and oleic acid (OA) [17] were most people's choices, the coordination groups of them are all carbonyl group with good coordination ability, and the shapes of $NaYF_4$:Yb, Er were mainly rod, prism, plate, and sphere. Using novel chelating ligands are very significant for preparing nanocrystals with different morphologies and applications. For example, in order to use UCNPs for bioprobe and bioimaging, some researchers used amine group to replace the other chelating ligands for biocompatibility by surface modification [18].

Herein, we directly introduced amine groups onto UCNPs by choosing a new chelating ligand tetraethylene pentamine (TEPA) to synthesis $NaYF_4$:Yb, Er through hydrothermal method. Tetraethylene pentamine's coordination groups are amine whose coordination ability is relatively week, while rod β-$NaYF_4$:Yb, Er nanoparticle can also be achieved. The exist of several amino of tetraethylene pentamine (TEPA) not only has a role of coordination but also can act as active point. We can introduce amine to the β-$NaYF_4$:Yb, Er nanocrystals directly without any other steps. Through amine, we can also introduce other functional groups, controlling the application performance of the β-$NaYF_4$:Yb, Er nanocrystals.

2. Experimental

2.1. Chemicals. All the chemicals were used directly without further purification. Tetraethylene pentamine (chemical grade) and Y $(NO_3)_3 \cdot 6H_2O$ (99.0%) were purchased from Sinopharm Chemicals Reagents Co., Ltd (Shanghai, China). Yb $(NO_3)_3 \cdot 5H_2O$ (99.99%), Er $(NO_3)_3 \cdot 5H_2O$ (99.9%) were supplied by Aladdin Chemistry Co. Ltd. NaF was analytical grade and brought from Tianjing Kermel Chemical Reagents Development Center (Tianjing, China).

2.2. Synthesis of $NaYF_4$:Yb, Er UCNPs. In a typical synthesis of hexagonal phase $NaYF_4$:Yb, Er nanocrystals, 4 mL 0.25 M 78% Y$(NO_3)_3$, 20% Yb$(NO_3)_3$, 2% Er$(NO_3)_3$ aqueous solution, 16 mL deionized water, and 20 mL ethanol were mixed with stirring at room temperature, after then, 0.2 mL TEPA was added into above solution, forming a A solution. 504 mg NaF was dissolved in 10 mL deionized water and 10 mL ethanol to form solution B. After 0.5 h stirring of solution A, B solution was added into A solution drop by drop under vigorous stirring. After aging for 30 min, the mixture was transferred to a 76 mL Teflon-lined autoclave, sealed, and heated at 200°C for 6 h. As the autoclave was cooled to room temperature naturally, collected the precipitates in the bottle, washed with ethanol and deionized water in sequence, gathered the products by centrifugation, then dried in air at 70°C for 10 h.

3. Characterizations

X-ray powder diffraction patterns were measured on a Rigaku D/MAX-2400 with Cu-Ka radiation. Upconversion fluorescence spectra were recorded on Hitachi F-4500 fluorescence spectrophotometer under the excitation of a 980 nm
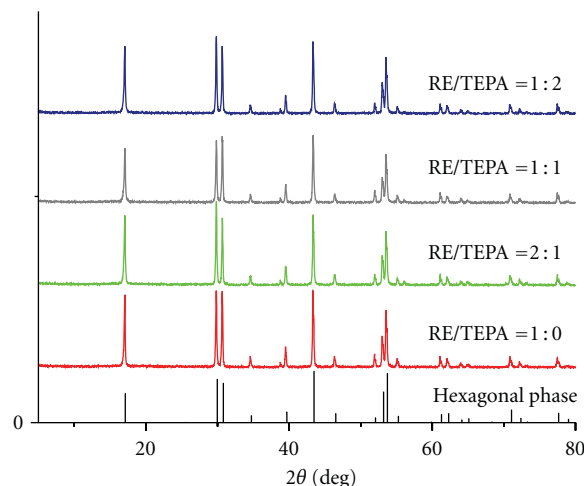

FIGURE 1: XRD patterns of $NaYF_4$:Yb, Er nanocrystals prepared under different ratio of RE/TEPA ($t = 6$ h; water/ethanol = 1 : 1; 16.7 mmol/L).
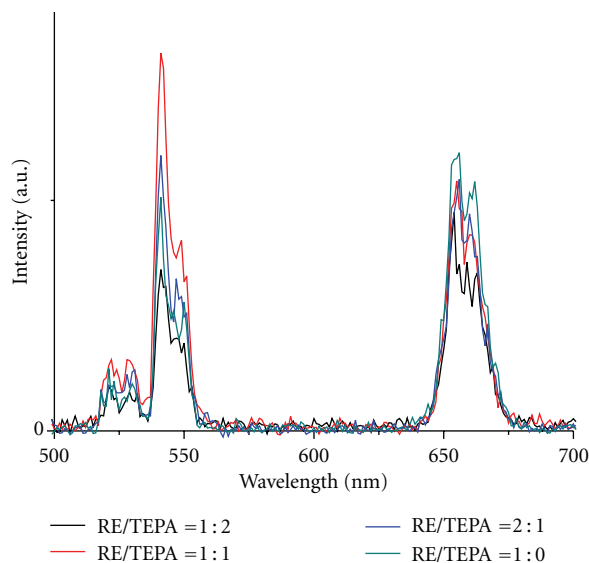

FIGURE 2: Upconverted fluorescence spectra of $NaYF_4$:Yb, Er nanocrystals prepared under different ratio of RE/TEPA ($t = 6$ h; water/ethanol = 1 : 1; 16.7 mmol/L).

diode laser. The morphologies of the samples were observed by using a Nova Nanosem 450 field emission scanning electron microscopy (FE-SEM).

4. Results and Discussion

The synthetic conditions of $NaYF_4$:Yb, Er via the hydrothermal method were investigated in detail. The influences of rare earth concentration, solvent composition, the ratio of RE/TEPA, and reaction time were all found to have effect on the luminescence properties and morphology of $NaYF_4$:Yb, Er nanocrystals.
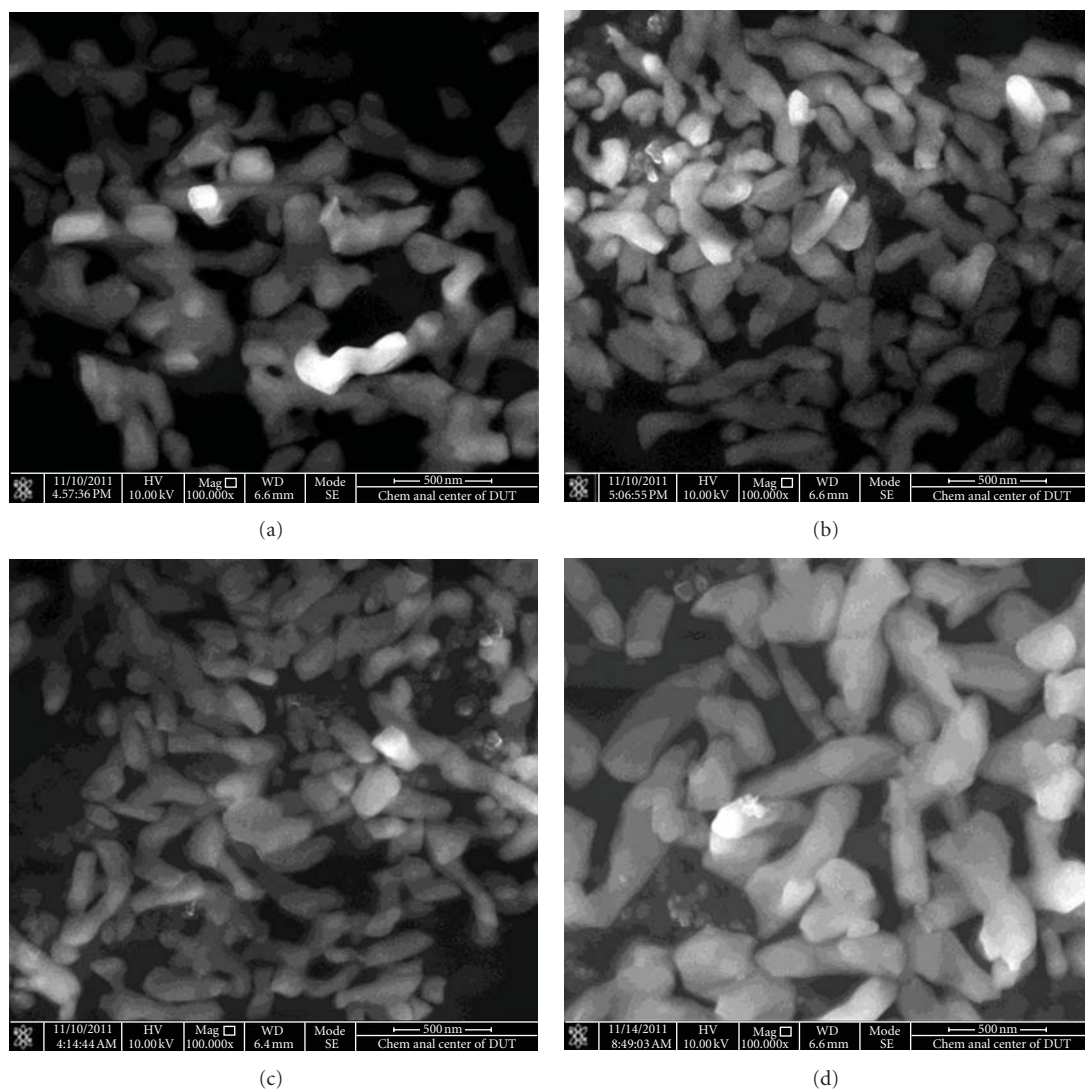
(a)

(b)

(c)

(d)

FIGURE 3: FE-SEM images of NaYF$_4$:Yb, Er nanocrystals prepared under different ratio of RE/TEPA: (a) RE/TEPA = 1 : 0; (b) RE/TEPA = 2 : 1; (c) RE/TEPA = 1 : 1; (d) RE/TEPA = 1 : 2 (t = 6 h; water/ethanol = 1 : 1; 16.7 mmol/L).

4.1. Effect of the Ratio of RE/TEPA. It is know that chelating agent is very important to the crystal's growth and aggregation. To prove the effect of TEPA on NaYF$_4$:Yb, Er nanocrystals, 0 mL, 0.1 mL, 0.2 mL, and 0.4 mL TEPA had been used to prepare NaYF$_4$:Yb, Er samples, that is, the ratio of the RE/TEPA was 1 : 0, 2 : 1, 1 : 1, and 1 : 2, respectively. Figure 1 shows the XRD spectra of the samples, and pure hexagonal NaYF$_4$ phases are observed for all the samples. From the fluorescence spectra (Figure 2) of the as-prepared products, it can be seen that, when RE/TEPA = 1 : 1, the luminescent intensity of the product is strongest, while the fluorescence intensity is lowest when the ratio of RE to TEPA is 1 : 2. This may be due to the fact that excessive TEPA will lead to energy loss through high energy vibration [19]. FE-SEM of the samples are showed in Figure 3; under the condition of no chelators added, the morphology of the as-prepared products was irregular. When TEPA is added, the

morphology of the products became relative better. When the ratio of RE/TEPA is 2 : 1; 1 : 1 and 1 : 2, the average size of the as-prepared nanocrystals are about 135 nm, 160 nm, and 222 nm, respectively. That is to say lower ratio of RE to TEPA is responsible for the larger particle size of β-NaYF$_4$:Yb, Er. Enough chelators could make more RE^{3+} coordinate with the N atom of TEPA and decrease the concentration of the RE^{3+} in the solvent; as a result, the speed of nucleation is delayed. As the time goes on, more and more rare earth ions are released and the crystals become bigger and bigger.

4.2. Effect of Reaction Time. Different reaction time was investigated to clarify that time has a effect on NaYF$_4$:Yb, Er nanocrystal's size and fluorescence intensity. 2 h; 4 h; 6 h; 8 h; 10 h were chosen to study. Figure 4 shows the XRD patterns of the samples, and it shows that all the samples are pure hexagonal; reaction time has little influence on
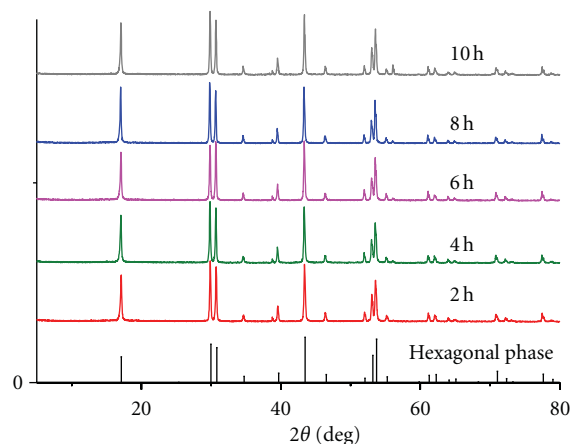
FIGURE 4: XRD patterns of NaYF$_4$:Yb, Er nanocrystals prepared under different reaction time (RE/TEPA = 1 : 1; water/ethanol = 1 : 1; 16.7 mmol/L).
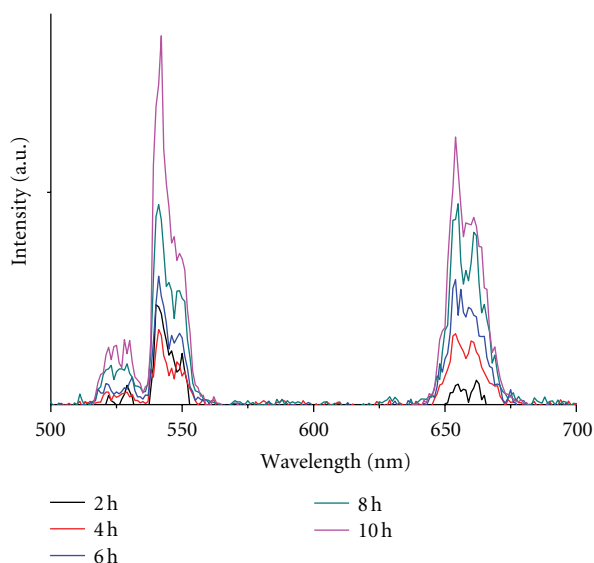

FIGURE 5: Upconverted fluorescence spectra of NaYF$_4$:Yb, Er nanocrystals prepared under different reaction time (RE/TEPA = 1 : 1; water/ethanol = 1 : 1; 16.7 mmol/L).

products' phase. Upconverted fluorescence spectra (Figure 5) show the difference between the as-prepared products; with the reaction time increases, the luminescent intensity of the nanoparticles was enhanced due to the increasing crystallinity. The FE-SEM of these samples (Figure 6) indicates when the reaction time is 2 h, the size of the as-prepared samples is relatively small, increases the time to 4 h, the size of the nanoparticles increases from 100 nm to 140 nm, while when the reaction time extends from 6 h to 10 h, the size of the nanoparticles has no evidence change.

4.3. Effect of Solvent Composition. Water and ethanol were used as solvent in this study. The composition of the

water/ethanol was taken as 2 : 1; 1 : 1; 1 : 2 with identical other parameters. The XRD of the as-prepared products is showed in Figure 7; it clearly shows that all the samples are pure hexagonal phase. As in Figure 9, FE-SEM images show the morphology of the corresponding products, the size becomes smaller when the ratio of water to ethanol changes from 2 : 1 to 1 : 2, the average size of the corresponding samples is about 245 nm; 160 nm; 94 nm. With the increase of ethanol in the solvent, the pressure of the autoclave increased and the solubility of the inorganic salts was lowered facilitating the supersaturation procedure, hence promoted the growth of the nanocrystal and improved the crystallinity of the nanocrystal [15]. Because the size of the sample prepared by water/ethanol = 1 : 2 is smaller than prepared by 1 : 1, considered both two factors, the luminescent intensity of the product prepared by water/ethanol = 1 : 1 was the strongest (Figure 8).

4.4. Effect of Rare Earth Concentration. As the volume of the Teflon-lined autoclave and total liquid is constant (60 mL), we changed moles of the rare earth to investigate the effect of the rare earth concentration on the fluorescence intensity and morphology of the as-prepared NaYF$_4$:Yb, Er. The concentration of the rare earth was taken as 8.33, 16.7, and 33.3 mmol/L, respectively, the other parameters were constant. Figure 10 is the XRD patterns of these samples. It can be seen that all of the products are hexagonal phase, so the rare earth concentration has no effect on crystal phase. Figure 12 is the FE-SEM of the product; the average size of the prepared nanocrystals is about 182 nm, 160 nm, and 125 nm, respectively, when the rare earth concentration was 8.33, 16.7, and 33.3 mmol/L. The lower the rare earth concentration is, the smaller the average size of the products. Rare earth concentration affects not only the morphology but also the fluorescence intensity of the prepared samples. The upconverted fluorescence spectra are given in Figure 11. When the rare earth concentration was 8.33 mmol/L, the luminescence intensity was the highest. With the increasing of the rare earth concentration, the luminescence intensity reduced. The phenomenon may be due to the difference in size, the larger the size, the stronger the luminescence intensity.

5. Conclusion

In summary, we have directly introduced amine groups onto UCNPs using TEPA as a new chelating ligand. A series of hexagonal phase NaYF$_4$:Yb, Er nanoparticles was obtained through hydrothermal method. The influences of rare earth concentration, the ratio of rare earth to TEPA, reaction time, and solvent composition on the morphology and fluorescence intensity of the as-prepared NaYF$_4$:Yb, Er samples were investigated. It was found the lower the rare earth concentration, the stronger the fluorescence intensity of the as-prepared NaYF$_4$:Yb, Er. When the ratio of RE/TEPA decreased, the size of the as-prepared nanocrystals increased, while when RE/TEPA reduced to 1 : 2, the fluorescence intensity of the product decreased. Long reaction time was
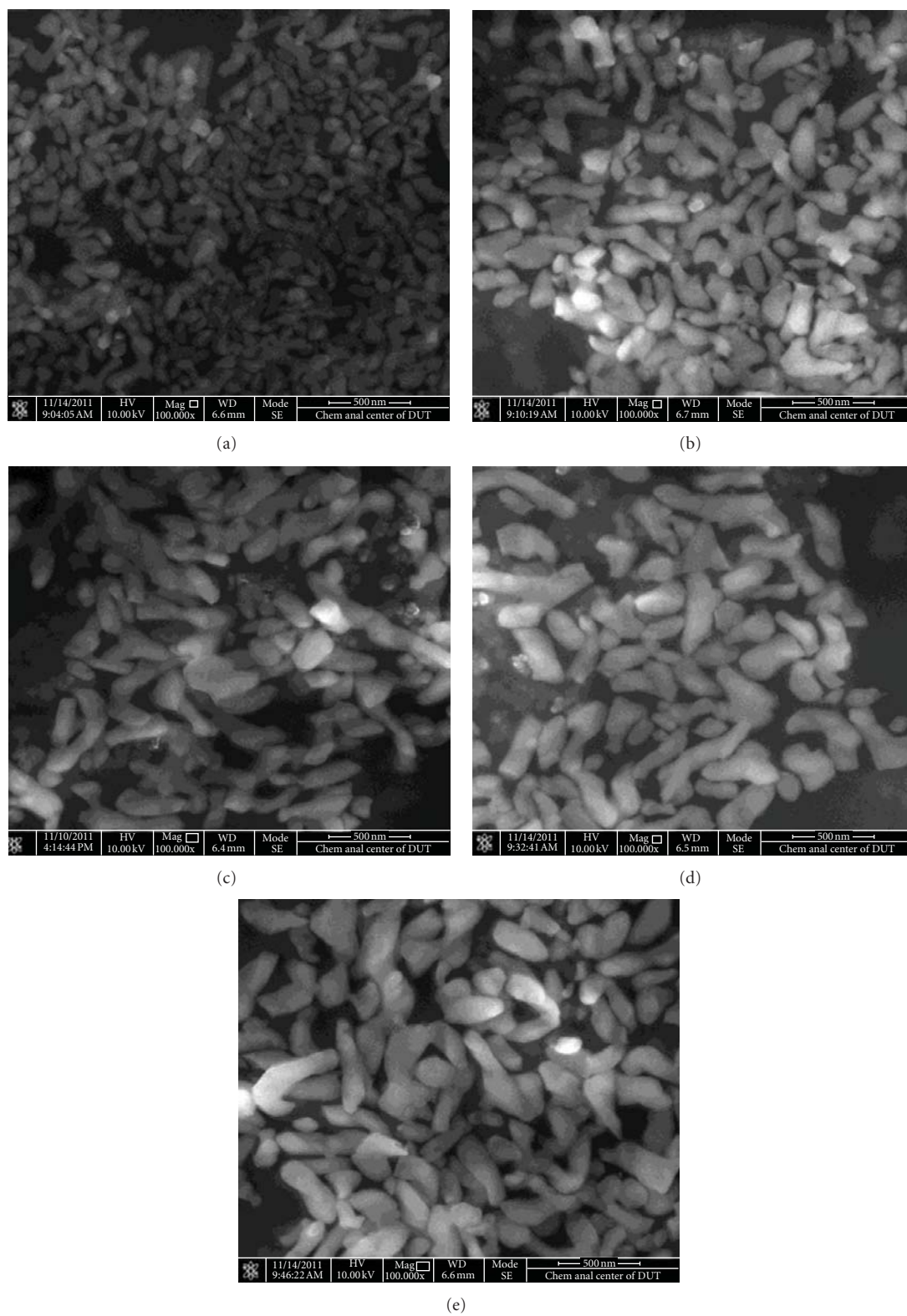
(a)

(b)

(c)

(d)

(e)

FIGURE 6: FE-SEM images of NaYF$_4$:Yb, Er nanocrystals prepared under different reaction times: (a) 2 h; (b) 4 h; (c) 6 h; (d) 8 h; (e) 10 h (RE/TEPA = 1 : 1; water/ethanol = 1 : 1; 16.7 mmol/L).
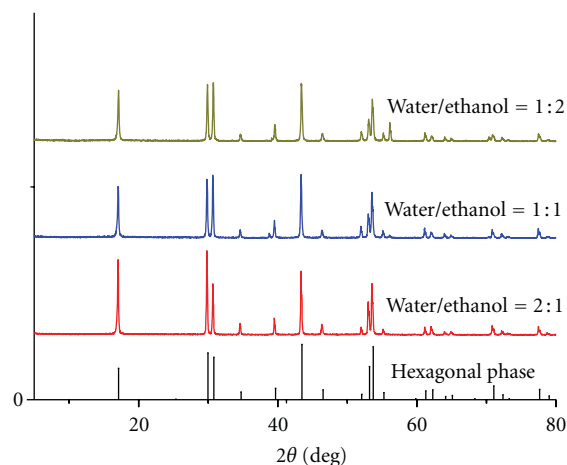
FIGURE 7: XRD patterns of NaYF$_4$:Yb, Er nanocrystals prepared under different solvent composition (RE/TEPA = 1:1; t = 6 h; 16.7 mmol/L).
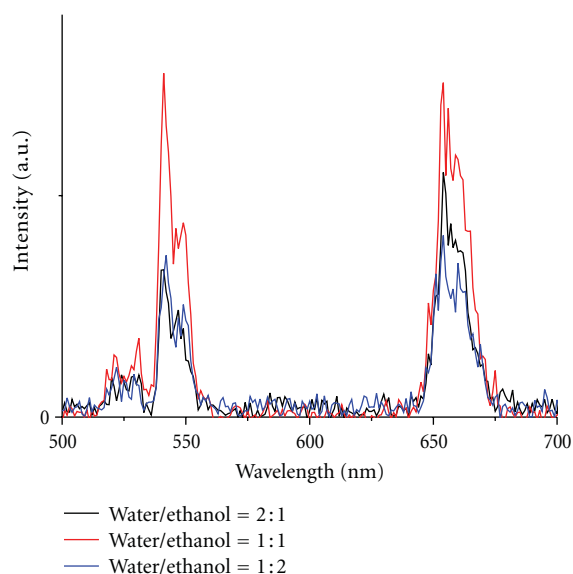
FIGURE 8: Upconverted fluorescence spectra of NaYF$_4$:Yb, Er nanocrystals prepared under different solvent composition (RE/TEPA = 1:1; t = 6 h; 16.7 mmol/L).

beneficial to the growth of the nanocrystal, when the time extended to 6 h, prolonged reaction time, nanocrystal's size had no evidence change, but the fluorescence intensity still enhanced. The solvent in different composition of water and ethanol was also discussed; with the increase of ethanol in the solvent, the size of the particle decreases, and when water/ethanol is 1:1, the fluorescence intensity of the as-prepared samples is strongest. The paper demonstrates that amine can be covered by nanocrystals directly without any other surface modification that makes the synthesis of bioprobe and bioimaging more easy and effective.
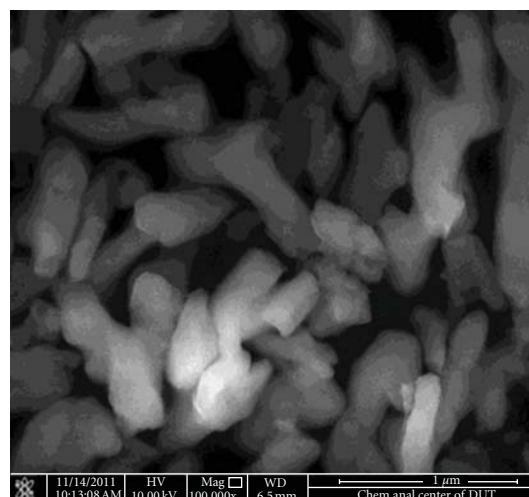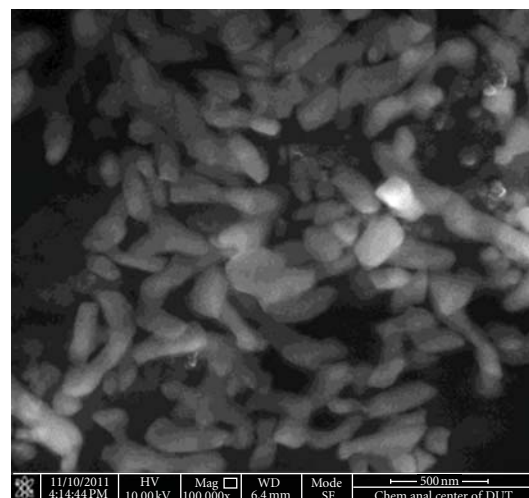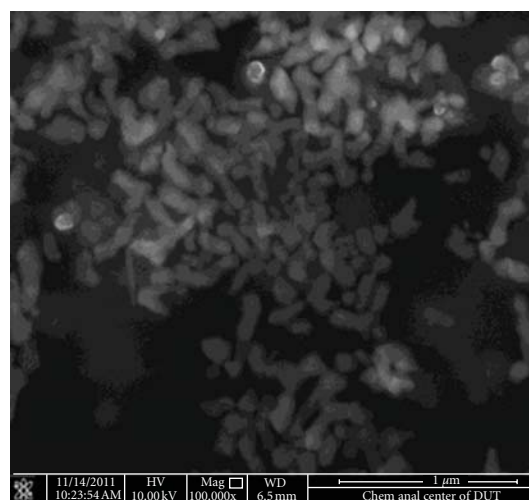
FIGURE 9: FE-SEM images of NaYF$_4$:Yb, Er nanocrystals prepared under different solvent composition: (a) water/ethanol = 2:1; (b) water/ethanol = 1:1; (c) water/ethanol = 1:2 (RE/TEPA = 1:1; t = 6 h; 16.7 mmol/L).
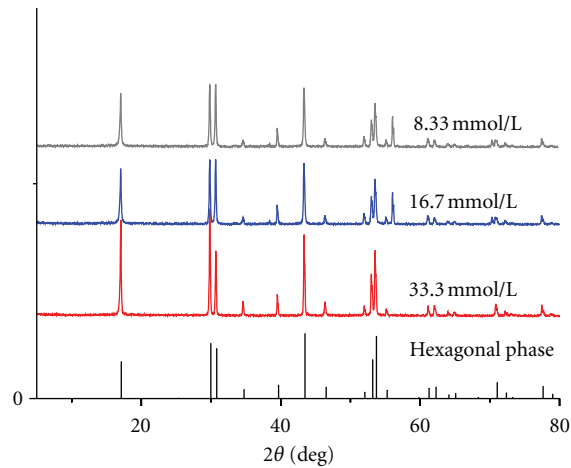
FIGURE 10: XRD patterns of NaYF$_4$:Yb, Er nanocrystals prepared under different rare earth concentration (RE/TEPA = 1 : 1; t = 6 h; water/ethanol = 1 : 1).
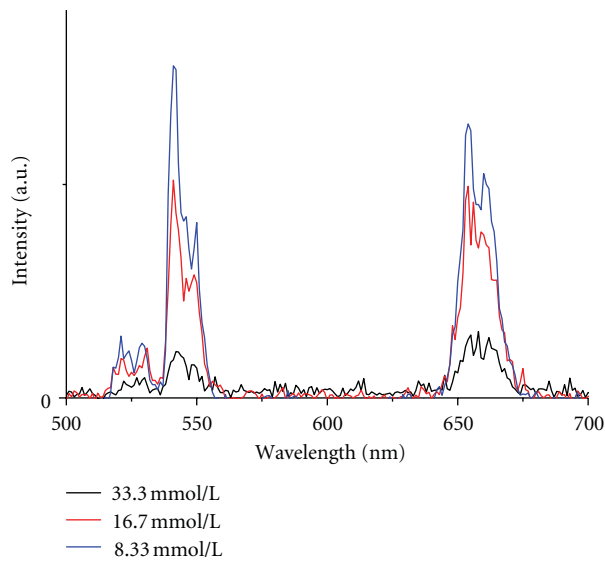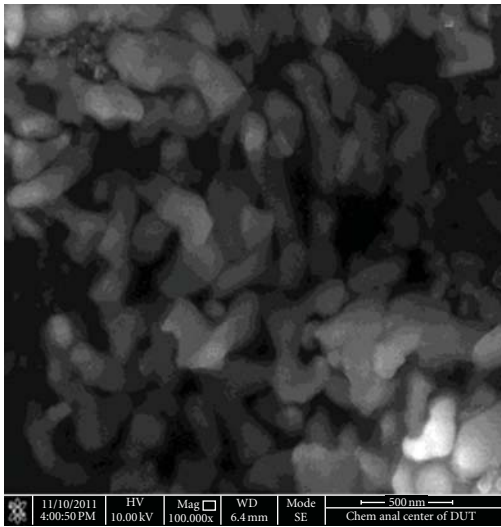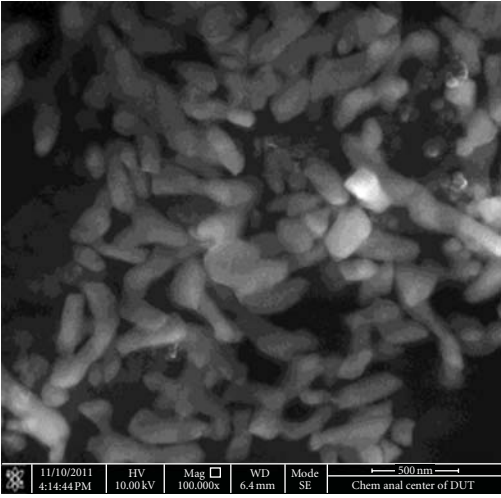

FIGURE 11: Upconverted fluorescence spectra of NaYF$_4$:Yb, Er prepared under different rare earth concentration (RE/TEPA = 1 : 1; t = 6 h; water/ethanol = 1 : 1).

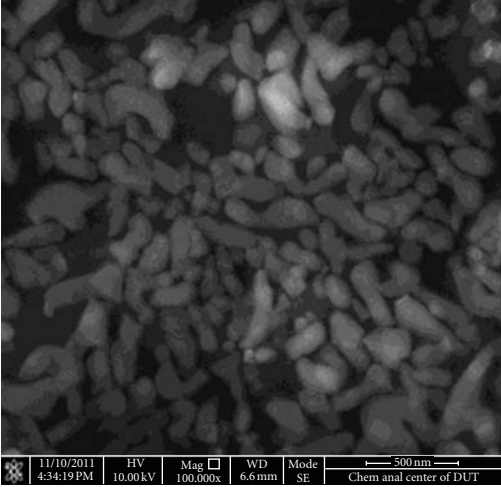## Acknowledgments

(a)

(b)

(c)

FIGURE 12: FE-SEM images of NaYF$_4$:Yb, Er nanocrystals prepared under different rare earth concentration: (a) 8.33 mmol/L; (b) 16.7 mmol/L; (c) 33.3 mmol/L (RE/TEPA = 1 : 1; t = 6 h; water/ethanol = 1 : 1).

References

[1] P. L. A. M. Corstjens, S. Li, M. Zuiderwijk et al., "Infrared up-converting phosphors for bioassays," *IEE Proceedings Nanobiotechnology*, vol. 152, no. 2, pp. 64–72, 2005.

[2] S. F. Lim, R. Riehn, W. S. Ryu et al., "In vivo and scanning electron microscopy imaging of upconverting nanophosphors in *Caenorhabditis elegans*," *Nano Letters*, vol. 6, no. 2, pp. 169–174, 2006.

[3] G. Yi, H. Lu, S. Zhao et al., "Synthesis, characterization, and biological application of size-controlled nanocrystalline NaYF$_4$:Yb,Er infrared-to-visible up-conversion phosphors," *Nano Letters*, vol. 4, no. 11, pp. 2191–2196, 2004.

[4] J. H. Zeng, J. Su, Z. H. Li, R. X. Yan, and Y. D. Li, "Synthesis and upconversion luminescence of hexagonal-phase NaYF$_4$:Yb, Er^{3+} phosphors of controlled size and morphology," *Advanced Materials*, vol. 17, no. 17, pp. 2119–2123, 2005.

[5] K. Deng, T. Gong, L. Hu, X. Wei, Y. Chen, and M. Yin, "Efficient near-infrared quantum cutting in NaYF$_4$: Ho^{3+}, Yb^{3+} for solar photovoltaics," *Optics Express*, vol. 19, no. 3, pp. 1749–1754, 2011.

[6] P. Cheben, F. Del Monte, D. J. Worsfold, D. J. Carlsson, C. P. Grover, and J. D. Mackenzie, "A photorefractive organically modified silica glass with high optical gain," *Nature*, vol. 408, no. 6808, pp. 64–67, 2000.

[7] F. Zhang, Y. Wan, T. Yu et al., "Uniform nanostructured arrays of sodium rare-earth fluorides for highly efficient multicolor upconversion luminescence," *Angewandte Chemie*, vol. 46, no. 42, pp. 7976–7979, 2007.

[8] Z. Hou, C. Li, P. Ma et al., "Electrospinning preparation and drug-delivery properties of an Up-conversion Luminescent Porous NaYF$_4$:Yb^{3+}, Er^{3+}@silica fiber nanocomposite," *Advanced Functional Materials*, vol. 21, no. 12, pp. 2356–2365, 2011.

[9] J. Shan, S. J. Budijono, G. Hu et al., "Pegylated composite nanoparticles containing upconverting phosphors and meso-tetraphenyl porphine (TPP) for photodynamic therapy," *Advanced Functional Materials*, vol. 21, no. 13, pp. 2488–2495, 2011.

[10] G. S. Yi and G. M. Chow, "Synthesis of hexagonal-phase NaYF$_4$:Yb,Er and NaYF$_4$:Yb,Tm nanocrystals with efficient upconversion fluorescence," *Advanced Functional Materials*, vol. 16, no. 18, pp. 2324–2329, 2006.

[11] W. Niu, S. Wu, S. Zhang, J. Li, and L. Li, "Multicolor output and shape controlled synthesis of lanthanide-ion doped fluorides upconversion nanoparticles," *Dalton Transactions*, vol. 40, no. 13, pp. 3305–3314, 2011.

[12] W. Niu, S. Wu, and S. Zhang, "A facile and general approach for the multicolor tuning of lanthanide-ion doped NaYF$_4$ upconversion nanoparticles within a fixed composition," *Journal of Materials Chemistry*, vol. 20, no. 41, pp. 9113–9117, 2010.

[13] J. Shan and Y. Ju, "Controlled synthesis of lanthanide-doped NaYF$_4$ upconversion nanocrystals via ligand induced crystal phase transition and silica coating," *Applied Physics Letters*, vol. 91, no. 12, Article ID 123103, 2007.

[14] J. Shan, X. Qin, N. Yao, and Y. Ju, "Synthesis of monodisperse hexagonal NaYF$_4$:Yb, Ln (Ln = Er, Ho and Tm) upconversion nanocrystals in TOPO," *Nanotechnology*, vol. 18, no. 44, Article ID 445607, 2007.

[15] Y. Wang, R. Cai, and Z. Liu, "Controlled synthesis of NaYF$_4$: Yb, Er nanocrystals with upconversion fluorescence via a facile hydrothermal procedure in aqueous solution," *CrystEngComm*, vol. 13, no. 6, pp. 1772–1774, 2011.

[16] J. H. Zeng, Z. H. Li, J. Su, L. Wang, R. Yan, and Y. Li, "Synthesis of complex rare earth fluoride nanocrystal phosphors," *Nanotechnology*, vol. 17, no. 14, article 032, pp. 3549–3555, 2006.

[17] X. Liang, X. Wang, J. Zhuang, Q. Peng, and Y. Li, "Synthesis of NaYF$_4$ nanocrystals with predictable phase and shape," *Advanced Functional Materials*, vol. 17, no. 15, pp. 2757–2765, 2007.

[18] C. Sun, C. Carpenter, G. Pratx, and L. Xing, "Facile synthesis of amine-functionalized Eu^{3+}-Doped La(OH)$_3$ nanophosphors for bioimaging," *Nanoscale Research Letters*, vol. 6, no. 1, pp. 24–30, 2010.

[19] P. R. Diamente and C. J. M. Frank, "Water-soluble Ln^{3+}-doped LaF$_3$ nanoparticles: retention of strong luminescence and potential as biolabels," *Journal of Fluorescence*, vol. 15, no. 4, pp. 543–551, 2005.

Research Article

Propeller-Shaped ZnO Nanostructures Obtained by Chemical Vapor Deposition: Photoluminescence and Photocatalytic Properties

S. L. Wang,[1] H. W. Zhu,[1] W. H. Tang,[2] and P. G. Li[1]

[1] *Department of Physics, Zhejiang Sci-Tech University, Hangzhou 310018, China*
[2] *School of Science, Beijing University of Posts and Telecommunications, Beijing 100876, China*

Correspondence should be addressed to S. L. Wang, slwang@zstu.edu.cn and P. G. Li, pgli@zstu.edu.cn

Propeller-shaped and flower-shaped ZnO nanostructures on Si substrates were prepared by a one-step chemical vapor deposition technique. The propeller-shaped ZnO nanostructure consists of a set of axial nanorod (50 nm in tip, 80 nm in root and 1 μm in length), surrounded by radial-oriented nanoribbons (20–30 nm in thickness and 1.5 μm in length). The morphology of flower-shaped ZnO nanostructure is similar to that of propeller-shaped ZnO, except the shape of leaves. These nanorods leaves (30 nm in diameter and 1–1.5 μm in length) are aligned in a radial way and pointed toward a common center. The flower-shaped ZnO nanostructures show sharper and stronger UV emission at 378 nm than the propeller-shaped ZnO, indicating a better crystal quality and fewer structural defects in flower-shaped ZnO. In comparison with flower-shaped ZnO nanostructures, the propeller-shaped ZnO nanostructures exhibited a higher photocatalytic property for the photocatalytic degradation of Rhodamine B under UV-light illumination.

1. Introduction

Zinc oxide (ZnO), a remarkable II–VI semiconductor with a wide direct band gap of 3.37 eV and large exciton binding energy of 60 meV at room temperature, has attracted considerable interests due to potential application in photocatalysis [1], sensors [2], light-emitting diodes [3], solar cells [4], and so forth. Compared with TiO_2, ZnO as a potential photocatalyst has the advantage of lower cost, absorbing more light quanta and higher photocatalytic efficiencies for the degradation of several organic pollutants in both acidic and basic medium than TiO_2 [5, 6]. Many strategies have been developed to improve the photocatalytic activity of ZnO nanostructures such as changing the structural and morphological characters (size, shape, and crystalline structure, etc.) [7, 8]. A variety of ZnO nanostructures such as nanowires [9], nanorings [10], nanorods [11], nanobelts [12], nanosheets [13], and star-shaped nanostructures [14] have been synthesized by a number of techniques, which mainly include the hydrothermal synthesis [15], solution-based synthesis [16], template-based synthesis [17], chemical vapor deposition (CVD) [18], arc discharge technique [19], and thermal evaporation process [20]. Although many works have been reported about the ZnO nanostructures, little information concerning the photocatalytic activity of propeller-shaped ZnO nanostructures was presented in previous studies [21, 22].

In this letter, propeller-shaped and flower-shaped ZnO nanostructures were prepared on Si substrates by a one-step chemical vapor deposition technique. The morphology, crystal structure, optical property, and photocatalytic property were studied.

2. Experimental Section

2.1. Sample Preparation. N type Si (001) substrates (1.5 cm × 1.5 cm) were ultrasonically cleaned in hydrochloric acid solution, acetone, and deionized water for 30 min, respectively. Commercial Zn powder (1.0 g) with a purity of 99.999% was used as the source material and put in an alumina boat, two pieces of Si substrates (position1: near the Zn powder at a

distance of 3 cm, the sample was labeled as S1; position 2: far from the Zn powder at a distance of 5 cm, the sample was labeled S2) were placed sequentially in the alumina boat. The boat was loaded into a furnace with a horizontal alumina tube. Two ends of the tube were sealed using mechanically clamped steel plates with the rubber gaskets. The tube was evacuated by a mechanical rotary pump. Then the furnace temperature was raised to 1000°C at a rate of ~20°C/min while oxygen gas was introduced into the chamber. After reaction for 1 h, the furnace was cooled down to room temperature naturally.

2.2. Characterization. The crystallographic information of the prepared samples was analyzed by powder X-ray diffraction (XRD) using a Bruker AXS D8 DISCOVER X-ray diffractometer with Cu Kα radiation (λ = 1.5406 Å). The morphology and composition of the as-deposited products were characterized by field emission scanning electron microscope (FESEM, S-4800) and energy-dispersive X-ray spectrometry (EDX), respectively. Transmission electron microscopy (TEM) and high-resolution transmission electron microscopy (HRTEM) were performed on JEOL 2010F high-resolution TEM system. Photoluminescence properties of ZnO nanostructures were measured on a FLSP920 fluorescence spectrometer using a Xe lamp with the excitation wavelength of 320 nm at room temperature. Brunauer-Emmett-Teller (BET) nitrogen adsorption-desorption was measured using a Micromeritics ASAP 2010 system.

The photocatalytic activity of the prepared samples was evaluated by the photocatalytic degradation of RhB aqueous solution performed at room temperature (ca. 20°C). The experimental procedure was as follows. 0.01 g of the prepared powders was dispersed in 30 mL of RhB aqueous solution with a concentration of 1.0×10^{-5} mol·L^{-1} in a beaker (with a capacity of 50 mL), and the suspensions were placed in dark for 30 min before illumination to allow sufficient adsorption of RhB. A 100 W mercury lamp placed 2 cm above the beaker with a wavelength of 365 nm was used as a light source. The concentration of RhB aqueous solution was determined by a UV-visible spectrophotometer (UV-4802H, UNICO). After UV-light irradiation for 30 min, the reaction solution was filtered, and then the absorbance of RhB aqueous solution was measured.

3. Results and Discussion

XRD analysis was adopted to analyze the crystal structure and phase composition of the obtained products. Figures 1(a, b) show the XRD patterns of the products obtained at different position. All the diffraction peaks can be indexed to wurtzite hexagonal ZnO (JCPDS Card file no. 70-2551). No other diffraction peaks are detected, indicating that all the as-prepared products are pure ZnO. Figure 2 shows FESEM images of the products obtained at different positions. As shown in Figure 2(a), the morphology of sample S1 is similar to the propellers, which consists of a set of axial nanorod (50 nm in tip, 80 nm in root and 1 μm in length), surrounded by radial oriented nanoribbons (20–30 nm in thickness and
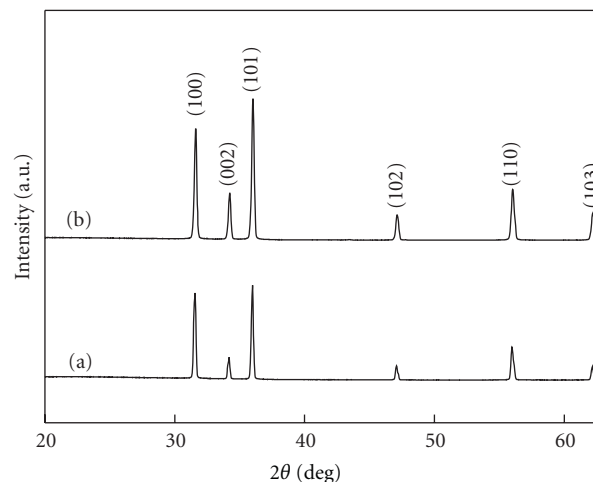

FIGURE 1: XRD patterns of the products obtained at different positions: (a) S1 and (b) S2.

1.5 μm in length). Figure 2(b) shows FESEM image of sample S2. The flower-shaped products are composed of aligned nanorods (30 nm in diameter and 1–1.5 μm in length) in a radial way, and all the nanorods pointed toward a common center. BET surface area measurements of samples indicate that the S$_{BET}$ of propeller-shaped and flower-shaped ZnO nanostructures are 23.5 m^2/g and 25.1 m^2/g, respectively.

TEM, HRTEM, and EDX were also used to characterize the structural properties of ZnO nanostructures. Figure 3(a) shows TEM image of a single nanoribbon in propeller-shaped ZnO nanostructures. The corresponding HRTEM image recorded from an individual nanoribbon (Figure 3(b)) clearly shows the well-resolved interference lattice fringe of about 0.28 nm that corresponds to the (100) crystal plane of ZnO phase. The EDX spectrum of propeller-shaped ZnO nanostructures was presented in Figure 3(c), in which the propeller-shaped products are composed only of Zn and O, and this result is in good accordance with the XRD analysis. The appearance of Si peak in the spectrum attributes to the silicon substrate. Figures 3(d), 3(e), and 3(f) show the TEM image, HRTEM image, and EDX spectrum of flower-shaped ZnO nanostructures, respectively. All character results indicate that the products synthesized in both positions are ZnO.

Figure 4 shows the room-temperature PL spectra recorded from propeller-shaped and flower-shaped ZnO nanostructures. The sharp peak at 378 nm corresponds to the near-band-edge emission (UV emission) of ZnO, which is attributed to the recombination of photogenerated electrons and holes [23]. The peak at 495 nm corresponded to the deep-level emission (visible emission) is associated with defects in ZnO lattice, such as oxygen vacancy and Zn interstitials [23, 24]. The deep-level emission (Figure 4(a), propeller-shaped ZnO) may indicate the existence of oxygen vacancies in the propeller-shaped nanostructures. Figure 4(b) shows a strong, dominated- and high-intensity peak at 378 nm in the UV region and a suppressed and weak band at 495 nm in the visible region. It is known
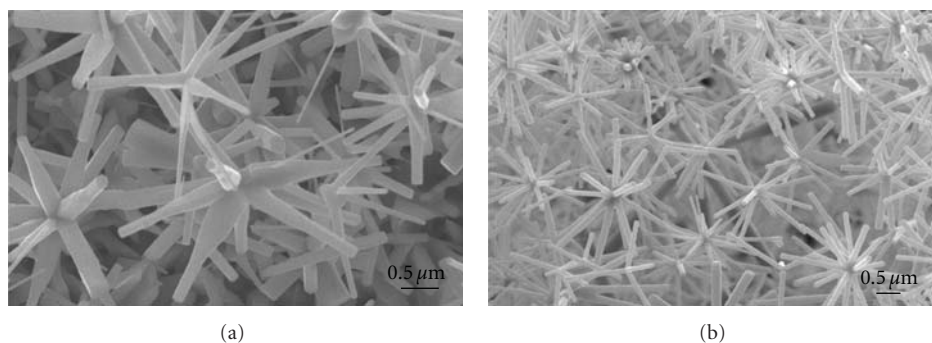
(a)

(b)

FIGURE 2: FESEM images of (a) propeller-shaped and (b) flower-shaped ZnO nanostructures.

(a)

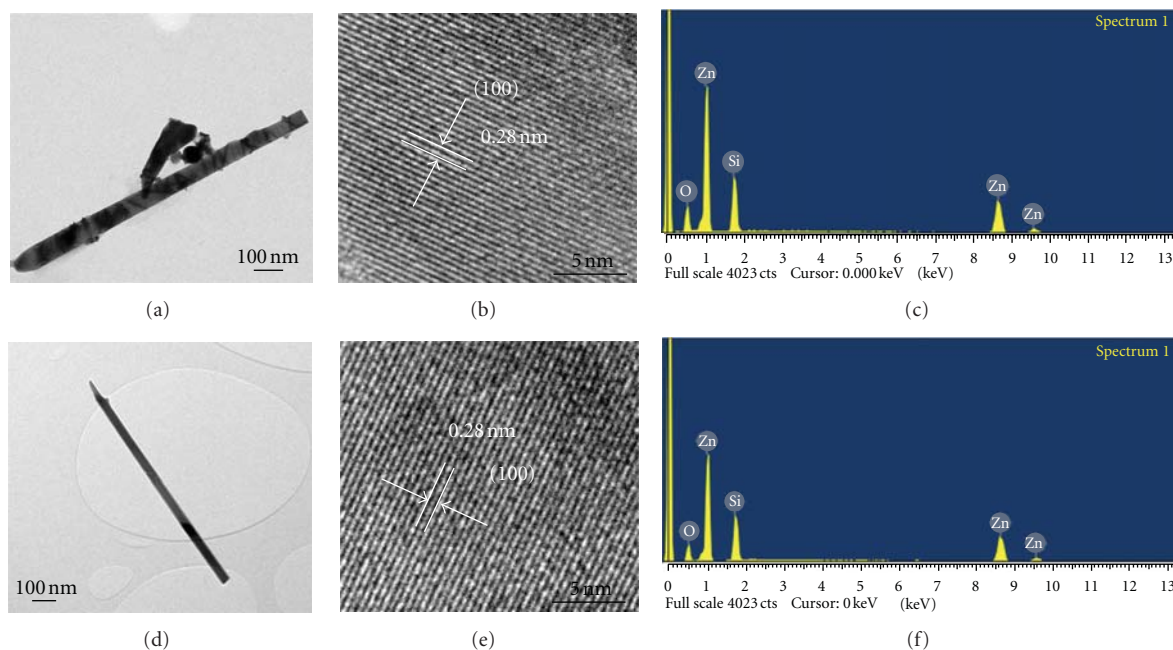(b)

(c)

(d)

(e)

(f)

FIGURE 3: (a, b, and c) TEM image, HRTEM image, and EDX spectrum of the propeller-shaped ZnO nanostructures, respectively; (d, e, and f) TEM image, HRTEM image, and EDX spectrum of the flower-shaped ZnO nanostructures, respectively.

that the improvement in the crystal quality such as low-structural defects, oxygen vacancies, zinc interstitials- and decrease in the impurities may cause the appearance of sharper and stronger UV emission and a suppressed and weakened green emission [25]. Thus, the strong UV emission and weak green emission observed in Figure 4(b) (flower-shaped ZnO) may be ascribed to the good crystal quality with less structural defects of flower-shaped ZnO nanostructures. The significant defect-related emission property of ZnO nanostructures may be beneficial to their photocatalytic property.

Heterogeneous semiconductor (TiO_2 and ZnO) photocatalysis is a promising new alternative method among advanced oxidation processes (AOPs) which generally includes UV/H_2O_2, UV/O_3 or UV/Fenton's reagent for oxidative removal of organic chemicals [26–28]. To demonstrate the photocatalytic of the ZnO nanostructures, the degradation of RhB was examined as a model reaction.

The variety of characteristic absorption of RhB at 554 nm was applied to monitor the photocatalytic degradation process. Figure 5 shows the UV-vis absorption spectrum of an aqueous solution of RhB (initial concentration: 1.0×10^{-5} M, 30 mL) in the presence of propeller-shaped ZnO nanostructures (0.01 g) under UV irradiation. The absorption peaks corresponding to RhB diminished gradually as the exposure time was extended. Figure 6 shows the comparison of photocatalytic activities of propeller-shaped and flower-shaped ZnO nanostructures. Significantly, the concentration of RhB barely changed without any catalyst (Figure 6(a)), whereas that of RhB gradually decreased in the presence of propeller-shaped and flower-shaped ZnO nanostructures under UV-light illumination. Obviously, the photocatalytic ability of propeller-shaped ZnO nanostructures is better than that of flower-shaped ZnO nanostructures (Figure 6(b, c)).

When the heterogeneous semiconductors are illuminated with UV-light, the electron/hole pairs are produced with
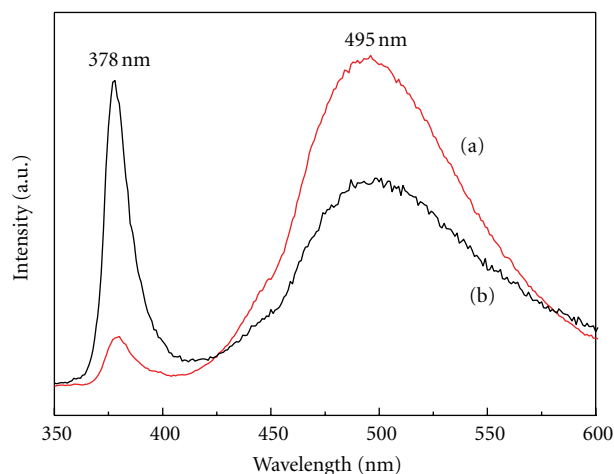
FIGURE 4: Photoluminescence spectra of (a) propeller-shaped and (b) flower-shaped ZnO nanostructures.
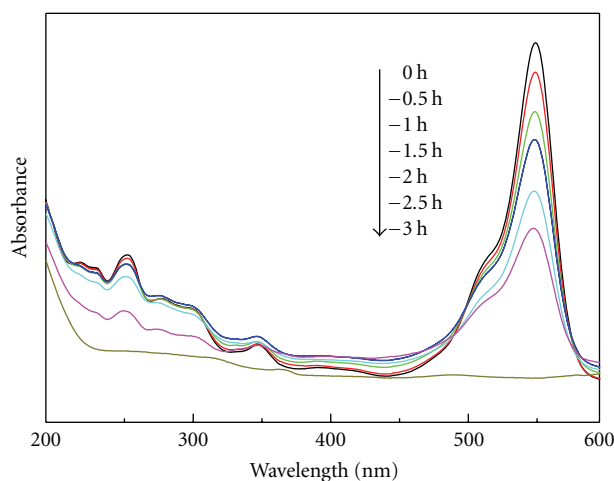

FIGURE 5: Absorption spectrum of the RhB solution in the presence of propeller-shaped ZnO nanostructures.

FIGURE 6: Photodegradation of RhB (1.0×10^{-5} M, 30 mL) under UV-light: (a) no catalyst, (b) flower-shaped ZnO nanostructures, and (c) propeller-shaped ZnO nanostructures. C is the concentration of RhB, and C_0 is the initial concentration.

be presented in both the propeller-shaped and flower-shaped ZnO nanostructures. Considering the S_{BET} of propeller-shaped samples ($23.5\,m^2/g$) is lower than that of the flower-shaped ones ($25.1\,m^2/g$), the higher photocatalytic property of propeller-shaped ZnO nanostructures for the degradation of RhB molecules may be caused by the lower rate of recombination between photogenerated holes and electrons on the surface of propeller-shaped ZnO nanostructures.

4. Conclusions

Propeller-shaped and flower-shaped ZnO nanostructures were prepared on Si substrates by chemical vapor deposition technique. In comparison with the propeller-shaped ZnO, the flower-shaped ZnO nanostructures show sharper and stronger UV emission at 378 nm and broader and weaker green emission at 495 nm, indicating a better crystal quality and fewer structural defects in the flower-shaped ZnO. However, the propeller-shaped ZnO nanostructures exhibited a more effective photocatalytic property for the photocatalytic degradation of Rhodamine B under UV-light illumination than flower-shaped ZnO nanostructures.

Acknowledgments

electrons promoted to the conduction band and leaving the positive holes in the valence band. These electron hole pairs can either recombine or can interact separately with other molecules and induce a complex series of reactions that might result in the complete degradation of the dye pollutants adsorbed on the surface of the semiconductor materials [29–31]. Based on the PL results mentioned above, the peak at 378 nm is due to the recombination of a photogenerated hole with an electron occupying the oxygen vacancies in the ZnO nanostructures, whereas the peak at 495 nm is caused by the recombination of electrons in single-occupied oxygen vacancies [31]. The low PL spectrum intensity at 378 nm (Figure 4(a), propeller-shaped ZnO) indicates that the rate of the recombination between photogenerated holes and electrons might be lower on the surface of propeller-shaped ZnO nanostructures than that of flower-shaped ZnO nanostructures, which is beneficial for the photocatalytic reaction. The PL spectra at 495 nm show that oxygen vacancies might
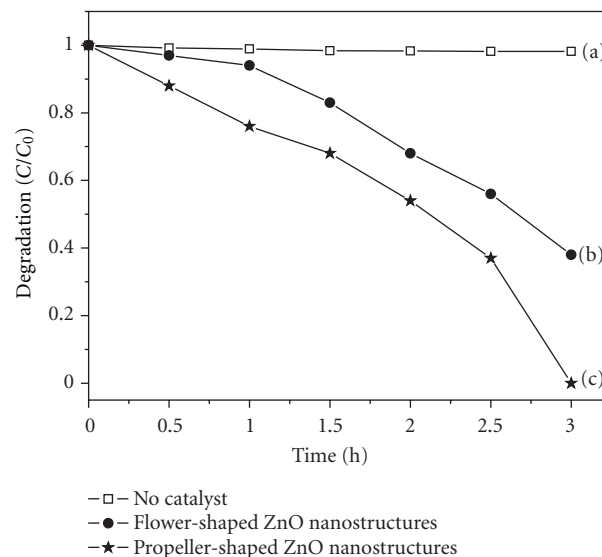
References

[1] T. J. Kuo, C. N. Lin, C. L. Kuo, and M. H. Huang, "Growth of ultralong ZnO nanowires on silicon substrates by vapor transport and their use as recyclable photocatalysts," *Chemistry of Materials*, vol. 19, no. 21, pp. 5143–5147, 2007.

[2] X. Wang, J. Zhou, J. Song, J. Liu, N. Xu, and Z. L. Wang, "Piezoelectric field effect transistor and nanoforce sensor based on a single ZnO nanowire," *Nano Letters*, vol. 6, no. 12, pp. 2768–2772, 2006.

[3] K. Keem, D. Y. Jeong, S. Kim et al., "Fabrication and device characterization of omega-shaped-gate ZnO nanowire field-effect transistors," *Nano Letters*, vol. 6, no. 7, pp. 1454–1458, 2006.

[4] T. P. Chou, Q. Zhang, G. E. Fryxell, and G. Cao, "Hierarchically structured ZnO film for dye-sensitized solar cells with enhanced energy conversion efficiency," *Advanced Materials*, vol. 19, no. 18, pp. 2588–2592, 2007.

[5] L. Y. Yang, S. Y. Dong, J. H. Sun, J. L. Feng, Q. H. Wu, and S. P. Sun, "Microwave-assisted preparation, characterization and photocatalytic properties of a dumbbell-shaped ZnO photocatalyst," *Journal of Hazardous Materials*, vol. 179, no. 1–3, pp. 438–443, 2010.

[6] J. C. Lee, S. Park, H. J. Park, J. H. Lee, H. S. Kim, and Y. J. Chung, "Photocatalytic degradation of TOC from aqueous phenol solution using solution combusted ZnO nanopowders," *Journal of Electroceramics*, vol. 22, no. 1–3, pp. 110–113, 2009.

[7] Y. Zhang, W. Zhang, and H. Zheng, "Fabrication and photoluminescence properties of ZnO:Zn hollow microspheres," *Scripta Materialia*, vol. 57, no. 4, pp. 313–316, 2007.

[8] M. S. Mohajerani, M. Mazloumi, A. Lak, A. Kajbafvala, S. Zanganeh, and S. K. Sadrnezhaad, "Self-assembled zinc oxide nanostructures via a rapid microwave-assisted route," *Journal of Crystal Growth*, vol. 310, no. 15, pp. 3621–3625, 2008.

[9] Y. C. Kong, D. P. Yu, B. Zhang, W. Fang, and S. Q. Feng, "Ultraviolet-emitting ZnO nanowires synthesized by a physical vapor deposition approach," *Applied Physics Letters*, vol. 78, no. 4, pp. 407–409, 2001.

[10] X. Y. Kong, Y. Ding, R. Yang, and Z. L. Wang, "Single-crystal nanorings formed by epitaxial self-coiling of polar nanobelts," *Science*, vol. 303, no. 5662, pp. 1348–1351, 2004.

[11] F. P. Albores, F. P. Delgado, W. A. Flores, P. A. Madrid, E. R. Valdovinos, and M. M. Yoshida, "Microstructural study of ZnO nano structures by rietveld analysis," *Journal of Nanomaterials*, vol. 2011, Article ID 643126, 11 pages, 2011.

[12] C. Ronning, P. X. Gao, Y. Ding, Z. L. Wang, and D. Schwen, "Manganese-doped ZnO nanobelts for spintronics," *Applied Physics Letters*, vol. 84, no. 5, pp. 783–785, 2004.

[13] R. C. Wang, C. P. Liu, J. L. Huang, and S. J. Chen, "ZnO symmetric nanosheets integrated with nanowalls," *Applied Physics Letters*, vol. 87, no. 5, Article ID 053103, 2005.

[14] A. Umar, S. Lee, Y. S. Lee, K. S. Nahm, and Y. B. Hahn, "Star-shaped ZnO nanostructures on silicon by cyclic feeding chemical vapor deposition," *Journal of Crystal Growth*, vol. 277, no. 1–4, pp. 479–484, 2005.

[15] G. Amin, M. H. Asif, A. Zainelabdin, S. Zaman, O. Nur, and M. Willander, "Influence of pH, precursor concentration, growth time, and temperature on the morphology of ZnO nanostructures grown by the hydrothermal method," *Journal of Nanomaterials*, vol. 2011, Article ID 269692, 9 pages, 2011.

[16] L. Poul, S. Ammar, N. Jouini, F. Fiévet, and F. Villain, "Metastable solid solutions in the system ZnO-CoO: synthesis by hydrolysis in polyol medium and study of the morphological characteristics," *Solid State Sciences*, vol. 3, no. 1-2, pp. 31–42, 2001.

[17] X. Sun, J. Liu, and Y. Li, "Use of carbonaceous polysaccharide microspheres as templates for fabricating metal oxide hollow spheres," *Chemistry—A European Journal*, vol. 12, no. 7, pp. 2039–2047, 2006.

[18] Z. Fan, D. Wang, P. C. Chang, W. Y. Tseng, and J. G. Lu, "ZnO nanowire field-effect transistor and oxygen sensing property," *Applied Physics Letters*, vol. 85, no. 24, pp. 5923–5925, 2004.

[19] Y. C. Choi, W. S. Kim, Y. S. Park et al., "Catalytic growth of β-Ga$_2$O$_3$ nanowires by arc discharge," *Advanced Materials*, vol. 12, no. 10, pp. 746–750, 2000.

[20] D. Peng, Y. Huang, K. Yu, L. Li, and Z. Zhu, "Synthesis and field emission properties of hierarchical ZnO nanostructures," *Journal of Nanomaterials*, vol. 2010, Article ID 560409, 5 pages, 2010.

[21] J. Liu, X. Huang, Y. Li, Q. Zhong, and L. Ren, "Preparation and photoluminescence of ZnO complex structures with controlled morphology," *Materials Letters*, vol. 60, no. 11, pp. 1354–1359, 2006.

[22] Z. L. Wang, "Novel nanostructures of ZnO for nanoscale photonics, optoelectronics, piezoelectricity, and sensing," *Applied Physics A*, vol. 88, no. 1, pp. 7–15, 2007.

[23] L. Xu, Y. Guo, Q. Liao, J. Zhang, and D. Xu, "Morphological control of ZnO nanostructures by electrodeposition," *Journal of Physical Chemistry B*, vol. 109, no. 28, pp. 13519–13522, 2005.

[24] C. C. Lin, K. H. Liu, and S. Y. Chen, "Growth and characterization of Zn-ZnO core-shell polygon prismatic nanocrystals on Si," *Journal of Crystal Growth*, vol. 269, no. 2–4, pp. 425–431, 2004.

[25] D. M. Bagnall, Y. F. Chen, Z. Zhu, T. Yao, M. Y. Shen, and T. Goto, "High temperature excitonic stimulated emission from ZnO epitaxial layers," *Applied Physics Letters*, vol. 73, no. 8, pp. 1038–1040, 1998.

[26] P. R. Gogate and A. B. Pandit, "A review of imperative technologies for wastewater treatment I: oxidation technologies at ambient conditions," *Advances in Environmental Research*, vol. 8, no. 3-4, pp. 501–551, 2004.

[27] P. R. Gogate and A. B. Pandit, "A review of imperative technologies for wastewater treatment II: hybrid methods," *Advances in Environmental Research*, vol. 8, no. 3-4, pp. 553–597, 2004.

[28] E. Yassıtepe, H. C. Yatmaz, C. Öztürk, K. Öztürk, and C. Duran, "Photocatalytic efficiency of ZnO plates in degradation of azo dye solutions," *Journal of Photochemistry and Photobiology A*, vol. 198, no. 1, pp. 1–6, 2008.

[29] H. Kyung, J. Lee, and W. Choi, "Simultaneous and synergistic conversion of dyes and heavy metal ions in aqueous TiO$_2$ suspensions under visible-light illumination," *Environmental Science and Technology*, vol. 39, no. 7, pp. 2376–2382, 2005.

[30] B. Pal and M. Sharon, "Enhanced photocatalytic activity of highly porous ZnO thin films prepared by sol-gel process," *Materials Chemistry and Physics*, vol. 76, no. 1, pp. 82–87, 2002.

[31] J. H. Sun, S. Y. Dong, Y. K. Wang, and S. P. Sun, "Preparation and photocatalytic property of a novel dumbbell-shaped ZnO microcrystal photocatalyst," *Journal of Hazardous Materials*, vol. 172, no. 2-3, pp. 1520–1526, 2009.

Research Article

Intense Visible Luminescence in CdSe Quantum Dots by Efficiency Surface Passivation with H_2O Molecules

Hyeoung Woo Park and Do-Hyung Kim

School of Physics and Energy Science, Kyungpook National University, Daegu 702-701, Republic of Korea

Correspondence should be addressed to Do-Hyung Kim, kimdh@knu.ac.kr

We have investigated the effect of water (H_2O) cooling and heat treatment on the luminescence efficiency of core CdSe quantum dots (QDs). The photoluminescence (PL) quantum yield of the CdSe QDs was enhanced up to ~85%, and some periodic bright points were observed in wide color ranges during the heat treatment of QDs mixed with H_2O. The PL enhancement of QDs could be attributed to the recovery of QDs surface traps by unreacted ligands confined within the hydrophilic H_2O molecule containers.

1. Introduction

Colloidal semiconductor nanocrystals, so-called quantum dots (QDs), have generated tremendous interest both for fundamental research and technical applications such as light emitting diodes (LEDs) [1], bioimaging [2], and solar cells [3]. Because of their size-dependent photoluminescence (PL) related to quantum-size effect tunable across the wide visible spectrum, CdSe QDs have become the most extensively investigated QDs [4]. Since core CdSe QDs usually have low luminescence efficiency, much experimental work has been devoted to surface passivation to improve the luminescence efficiency of QDs. Several methods of organic and inorganic surface modification have been developed to mediate the problems by passivation of the surface defects of QDs. The organic passivation methods such as polymer encapsulation, surface grafting, and ligand exchange [5–7] have usually accompanied a decrease in quantum yield (QY) and an undesirable size increase relative to the original QDs and more QDs being included in the polymer encapsulation. It is well know that shelling of inorganic atomic layers with a wider bandgap on the surface of core QDs effectively reduces nonradioactive recombination which results in the enhancement of PL QY [8, 9]. The QY reported values are generally lower than 50% for nonpassivation QDs and the best reported values of QY are approximately ~80%

for inorganic-shelled QDs [9, 10]. For this reason, the effects and methods for shelling on the surface of core QDs have been intensively studied. However, additional inorganic shelling has to be delicately controlled to obtain the desirable atomic layers and can have possible problems such as lattice mismatch (limited materials), FWHM broadening, and size increases. Moreover, the various shelled QDs still have surface state problem such as PL decrease of multishell QDs at ligand exchange process [11]. QDs are commonly prepared by organometallic chemistry using a mixture of trioctylphosphine (TOP) and trioctylphosphine oxide (TOPO) as the prototypical ligand system [10]. These ligands as the capping group provide colloidal stability in organic solvents such as chloroform, hexane, and toluene and serve as agents for reducing the undesirable electronic effects related to dangling bonds or surface states. Although the surfaces of the QDs are passivated by these organic ligands during the synthesis process, the PL QY of the QDs is usually very low. There was a report about the "bright point" of core QDs, in which the QY reached approximately ~80% by adjusting the chemical ratio, synthesis time, and temperature [12]. However, the wavelength showing the "bright point" was limited to orange color range at about ~610 nm. It could also be very effective to enhance the PL QY by reducing some or the entire surface trapping states of the low QY QDs through a simpler posttreatment instead of searching for complex
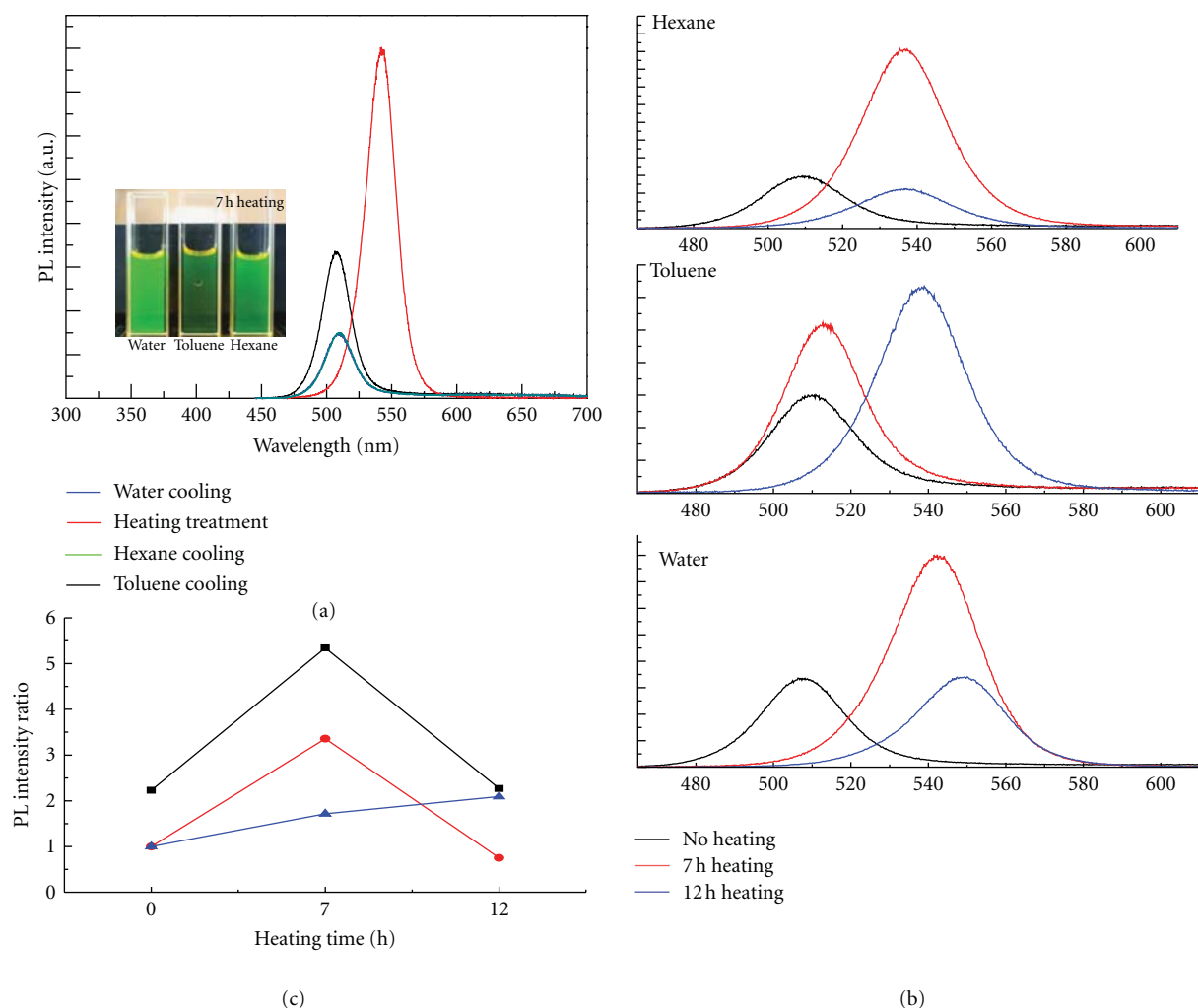
FIGURE 1: (a) The PL spectra of the QDs cooled by different solvents and additional heat treatment, (b) the change in PL spectra after additional heat treatment of the QDs in different solvents, (c) the ratio of PL peak intensity calculated from the experimental date of (b). The inset of (a) is the photograph of core CdSe QDs under room light.

synthesis conditions. Therefore, in this communication, we have designed H_2O containers as a mechanism in order to recovery surface trap states effectively. We have improved dramatically the PL QY of the core CdSe QDs up to ~85% in the green color range which was not in the reported bright point widow of the orange color.

2. Experimental Procedures

A 2 M stock solution of trioctylphosphine selenide (TOP : Se) was prepared by dissolving 15.8 g of Se into 100 mL of TOP. The stock solution was filled in 100 mL three-neck round-bottomed flask and fitted with a thermocouple temperature sensor and condenser, with TOPO (10 g), HDA (10 g) and TOP (2.5 mL), and heat to 170°C under vacuum for 1-2 h and raise the temperature to 340–350°C. In a separate vial, mix Cd(acac)$_2$ (620 mg), HDDO (1 g), and TOP (5 mL) and heat under vacuum to 100°C; the solution should become homogeneous. Cool the mixture to approximately 80°C

and add 5 mL of a 2 M TOP : Se. The solution mixture of cadmium and selenium precursors was rapidly injected into the hot flask containing the coordinating solvent, and then cooled using each solvents. The QDs extracted from same hot batch were divided into different cooling solvents. The QDs with different cooling solvents were heated in vacuum oven under air condition at 120°C.

3. Results and Discussion

Figures 1(a) and 1(c) show a 2-fold increase in the PL intensity obtained by changing the cooling process. The 5-fold enhancement in the PL intensity was finally achieved by additional heat treatment. Diverse solvents such as toluene, hexane, methanol, ethanol, acetone, and H_2O were applied to confirm the effect of the cooling process on the enhancement of the PL intensity of the QDs (Figure 2(a)). Toluene and hexane were most frequently used in the cooling process because the QDs dissolved very well in these solvents.
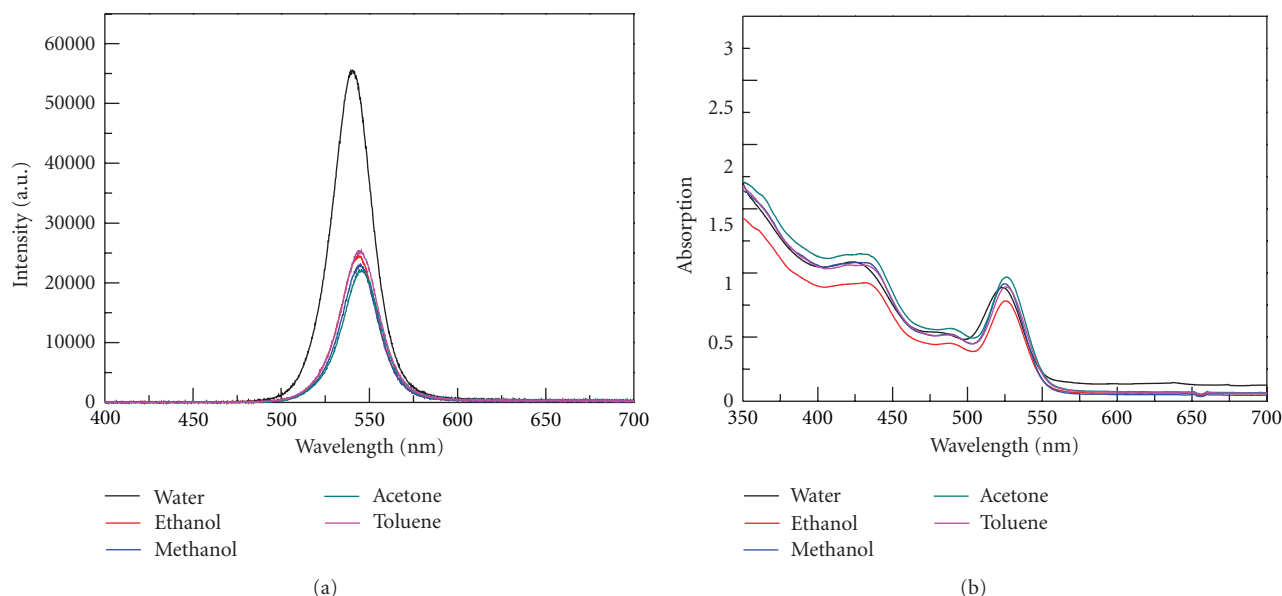
(a)

(b)

FIGURE 2: (a) Absorption and (b) PL spectra of QDs cooled by diverse solvents (toluene, hexane, methanol, ethanol, acetone, and H_2O).
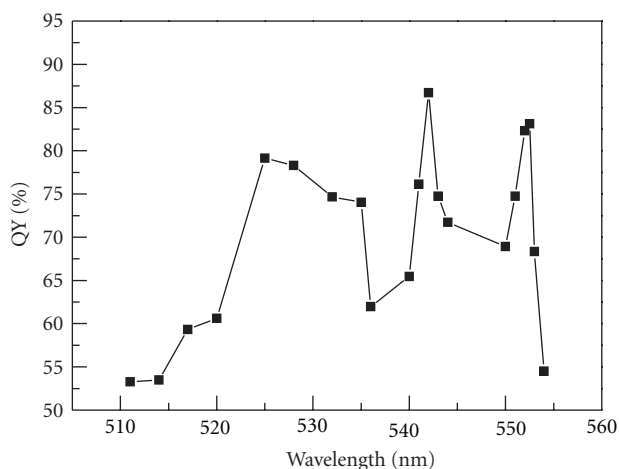

FIGURE 3: The QY and red-shift of CdSe QDs during heat treatment. QYs calculated by comparison of the standard dye Rhodamine 6G.
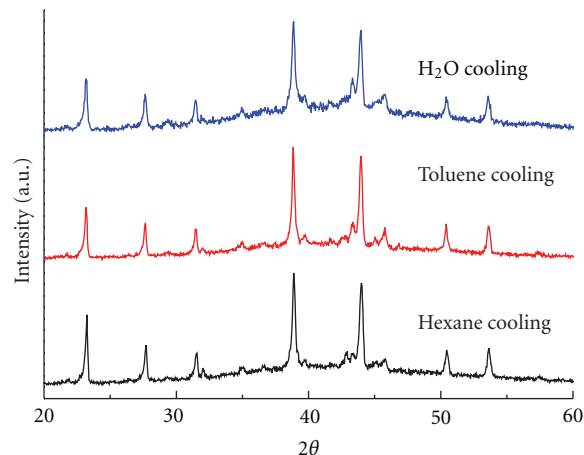

FIGURE 4: XRD patterns of CdSe QDs with different cooling solvents.

It was also confirmed that the extracting orders of the QDs and transferring orders to the solvents did not have a significant effect on the PL properties of the QDs. Therefore, the cooling process was the main parameter for comparing the PL properties of the QDs in these experiments. The supernatant QDs collected after mixing vigorously with H_2O were redispersed in toluene or hexane to measure the PL. The concentration of the QD samples was adjusted by the absorption peak of the QDs previously described elsewhere (Figure 2(b)) [13]. The PL enhancement in H_2O-cooled QDs could be related to the surface states induced during the H_2O cooling process compared to that of the QDs cooled in toluene or hexane (Figures 1(a) and 1(c)). The QD samples remixed with H_2O after cooling first in toluene or hexane did not show any enhanced PL intensity. It is worth mentioning

that no significant enhancement of PL was observed in water-mixed QD samples after the cooling process using organic solvents. It means that PL enhanced mechanism related to H_2O-cooled QDs could be decided during the first cooling process after extracting the QDs from the reaction flask.

The PL intensity of the QDs can be further improved by low heat treatment (Figure 1(b)). The effects of heat treatment on the PL intensity of the QDs were investigated by changing the duration of the heat treatment at 120°C. The QDs solutions were prepared by mixing the QDs and the different cooling solvents in vacuum oven under air conditions heated at 120°C, the concentrations of the heat-treated QD solutions were also adjusted by diluting with toluene or hexane based on their absorption spectra as previously reported. After the heat treatment, the QD
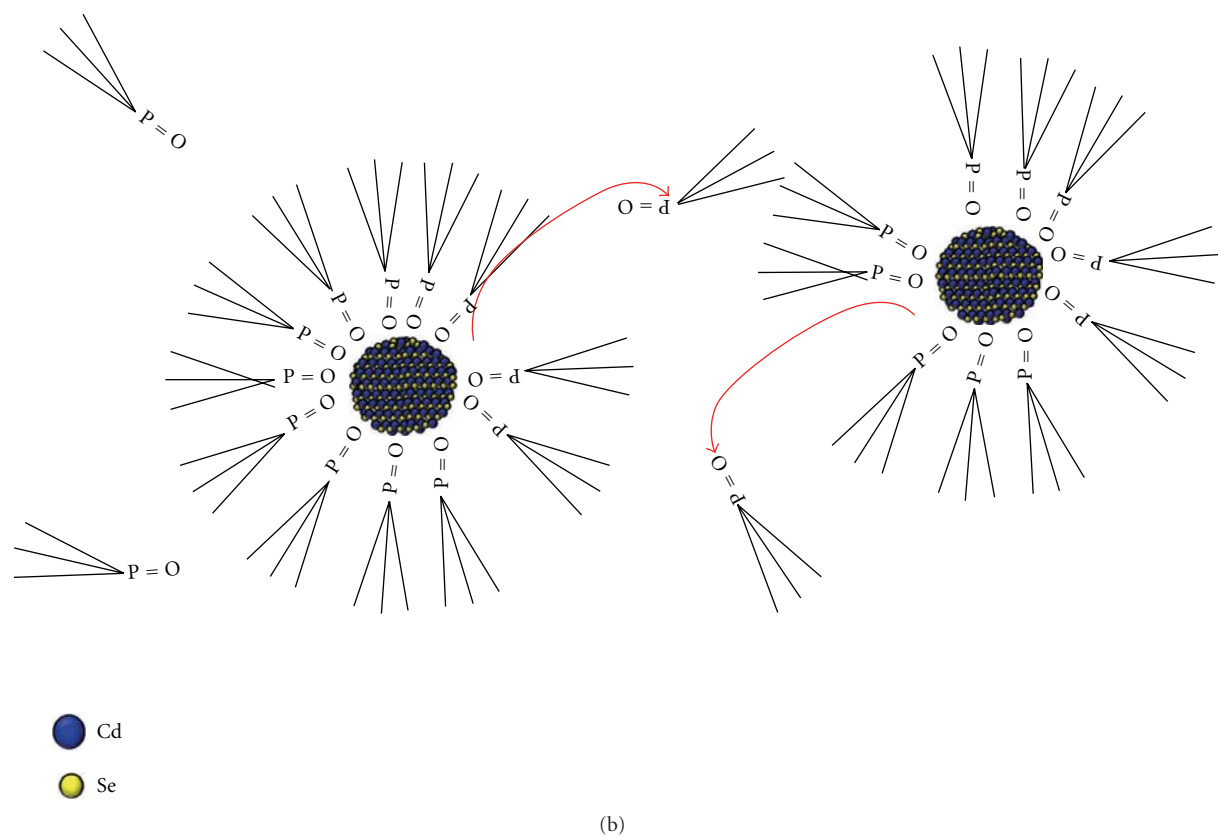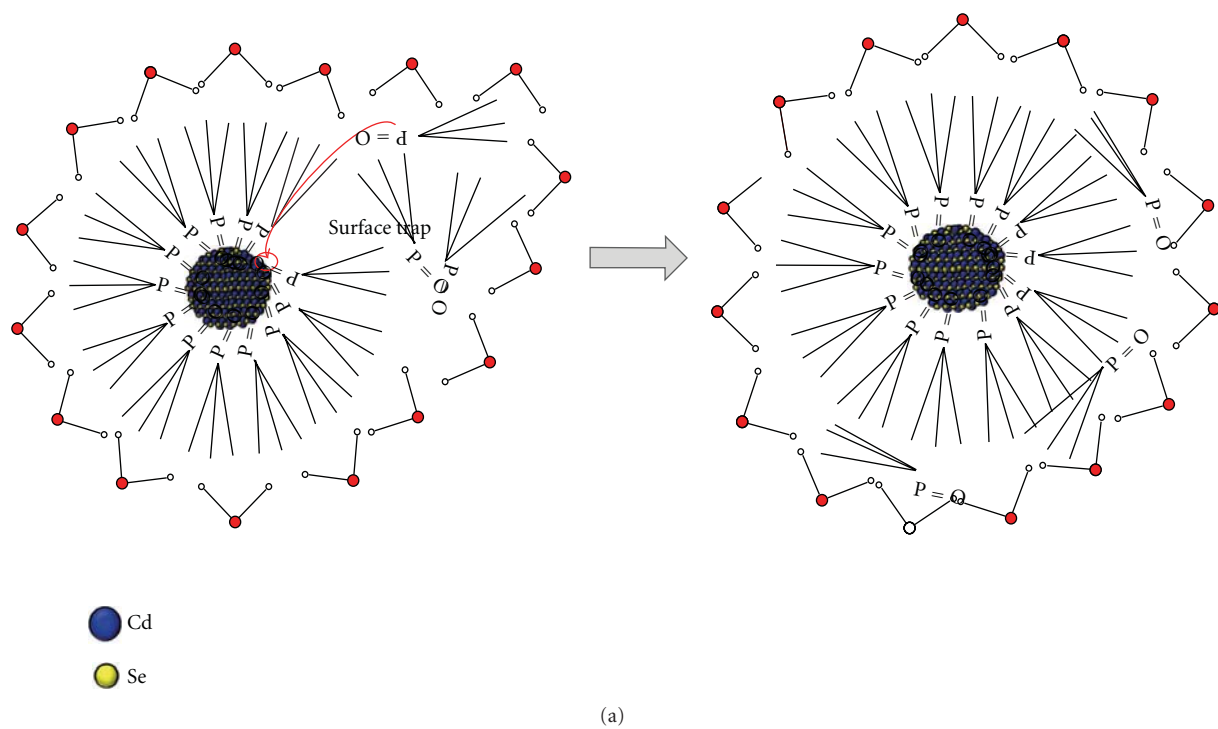
Cd

Se

(a)

Cd

Se

(b)

FIGURE 5: Schematic of (a) the mechanism for the enhanced ligand passivation of QDs within H_2O molecular containers, (b) the states of QDs and ligands within general organic solvents.

solutions showed red shifts in the PL spectra which could be a result of additional growth during the heat treatment. The red-shifted values of each sample were different, which could be due to the difference in the effective heat energy contributing to the QDs growth related to the different vapor temperatures of the toluene and hexane. The high PL intensities of the CdSe QDs were shown to be at around three wavelengths of 525 nm, 542 nm, and 552 nm during the extended heat treatment. Some periodic bright points were shown before the rapid deterioration of PL QY for the QDs (Figure 3).This result demonstrates a possible method to control the emission color of QDs related to bright point using postheat treatment. From the results of the periodic enhancement of PL QY, it is assumed that the optimized states of the QD surfaces showing the high PL QY could have existed during the postheat treatment. The as-synthesized core QDs with low PL QY could be due to the role of seeds with relatively more surface defects which could further increase the size of the seeds (showing the red-shift) accompanied by the effective recovery of surface defects with unreacted source compounds and ligands inside the H_2O molecule containers during the postheat treatment. The reduction in PL QY of the QDs after passing the bright point could be attributed to the occurrence of perturbation in the optimized structure of the QDs at the bright point. The average PL QY at the bright point had values over approximately 80% and FWHM was approximately 22 nm. The bright points with the high PL QY of the core QDs could not be confined to the orange color range but also existed in a wider color ranges during the heat treatment.

Cordero and coworkers demonstrated that PL increase by adsorbed water molecules [14]. Myung and coworkers had also shown PL increase by oxygen passivation of surface states [15]. In both cases, it was suggested that the PL enhancement of QDs is originated by the additional oxide layer formed on the QDs' surface. However, we suggest different mechanism for the PL enhancement because of two reasons. First, no significant differences in XRD data from all samples with different cooling process showed similar XRD patterns (Figure 4). The formation of oxide layer on the surface of water-cooled QDs could generate different XRD patterns/additional peaks related to oxide layer. Second, if the PL enhancement is originated by an oxide shell, a single optimal shell thickness showing the maximum PL intensity could exist. The PL intensity could be continuously decreased beyond the optimal shell thickness, which is generally observed during the shelling process [16]. However, the periodic bright points were shown during extended annealing of QDs within H_2O molecule containers (Figure 3), which is significantly different behavior compared with the shelling process.

Therefore we suggested basic chemical mechanism for the dramatic improvement of QY in the H_2O cooling process, and heat treatment is suggested in Figure 5(a). In the case of the aqueous synthesis, the CdTe QDs showed a very high PL QY at about ~90% QY [17] using the well-known Stöber method [18, 19]. In contrast, general solvent synthesis methods avoid H_2O and air which could induce oxidation and damage of the QDs. However, the luminescence properties of the QDs were not degraded when the as-synthesized QDs were mixed with H_2O. QDs with hydrophobic ligands have no chance for direct contact with H_2O just like water and oil. This phenomenon can be applied to confine QDs within H_2O molecule containers which could have a similar role as a reverse micelle. The distance between the confined QDs and the unreacted ligands/chemical compounds is much closer within the H_2O molecule containers, which results in a decrease in the activation energy required for a chemical reaction. This environment within H_2O molecule containers leads to a larger red-shift of H_2O-cooled QDs compared to solvent-cooled ones in the PL spectra with the same heat-treatment time (Figure 1(b)). The high enhancement of PL QY can only be obtained from the H_2O-cooling process with the high-temperature QDs. Therefore, it is assumed that the confinement environment and temperature are necessary to enhance the PL QY of QDs by the efficient recovery of surface trap states during the H_2O cooling process. In contrast, cooling using organic solvents could not meet both requirements and brought about the loss of surface ligands by generating a well-dispersive state (Figure 5(b)). Qu and Peng demonstrated that the PL bright point of QDs is in the orange color region which was observed in the QDs synthesis process [12]. However, our results show a more "bright point" and existed in more widely optical windows (Figure 2) due to the H_2O cooling and postheat treatment process. These findings will significantly contribute to the development of bright core QDs and have also considerable implications for diverse application by further passivation processes accompanied with water such as silica coating, polymer encapsulation, and biofunctionalism. The suggested method provides an environmentally friendly method compared to cooling processes using organic solvents which generate CO_2.

4. Conclusions

In conclusion, we have reproducibly demonstrated high enhancement of PL QY in the core of QDs and color controllability by finding additional bright points with an H_2O-cooling and postheat treatment process. It was experimentally confirmed that the H_2O molecular containers could effectively passivate the surface defects of core QDs by the reaction of unreacted ligands/source compounds within H_2O molecule containers. These findings can have significant potential implications in refuting the stereotypes that the H_2O conceptually degrades the luminescent properties of QDs and has to be avoided in the synthesis and posttreatment of QDs. This suggested method also provides an environmentally friendly method without using organic solvents.

Acknowledgment

References

[1] P. O. Anikeeva, J. E. Halpert, M. G. Bawendi, and V. Bulović, "Electroluminescence from a mixed red-green-blue colloidal quantum dot monolayer," *Nano Letters*, vol. 7, no. 8, pp. 2196–2200, 2007.

[2] H. Tada, H. Higuchi, T. M. Wanatabe, and N. Ohuchi, "In vivo real-time tracking of single quantum dots conjugated with monoclonal anti-HER2 antibody in tumors of mice," *Cancer Research*, vol. 67, no. 3, pp. 1138–1144, 2007.

[3] B. Farrow and P. V. Kamat, "CdSe quantum dot sensitized solar cells. Shuttling electrons through stacked carbon nanocups," *Journal of the American Chemical Society*, vol. 131, no. 31, pp. 11124–11131, 2009.

[4] M. G. Bawendi, P. J. Carroll, W. L. Wilson, and L. E. Brus, "Luminescence properties of CdSe quantum crystallites: resonance between interior and surface localized states," *The Journal of Chemical Physics*, vol. 96, no. 2, pp. 946–954, 1992.

[5] W. T. Al-Jamal, K. T. Al-Jamal, P. H. Bomans, P. M. Frederik, and K. Kostarelos, "Functionalized-quantum-dot-liposome hybrids as multimodal nanopartides for cancer," *Small*, vol. 4, no. 9, pp. 1406–1415, 2008.

[6] J. K. Kim, S. H. Lim, Y. Lee et al., "Conjugation of DNA to streptavidin-coated quantum dots for the real-time imaging of gene transfer into live cells," in *Proceedings of the NSTI Nanotechnology Conference and Trade Show*, vol. 3, pp. 379–382, March 2004.

[7] X. Ji, J. Zheng, J. Xu et al., "(CdSe)ZnS quantum dots and organophosphorus hydrolase bioconjugate as biosensors for detection of paraoxon," *Journal of Physical Chemistry B*, vol. 109, no. 9, pp. 3793–3799, 2005.

[8] D. V. Talapin, I. Mekis, S. Götzinger, A. Kornowski, O. Benson, and H. Weller, "CdSe/CdS/ZnS and CdSe/ZnSe/ZnS core-shell-shell nanocrystals," *Journal of Physical Chemistry B*, vol. 108, no. 49, pp. 18826–18831, 2004.

[9] D. Pan, Q. Wang, S. Jiang, X. Ji, and L. An, "Synthesis of extremely small CdSe and highly luminescent CdSe/CdS core-shell nanocrystals via a novel two-phase thermal approach," *Advanced Materials*, vol. 17, no. 2, pp. 176–179, 2005.

[10] G. W. Huang, C. Y. Chen, K. C. Wu, M. O. Ahmed, and P. T. Chou, "One-pot synthesis and characterization of high-quality CdSe/ZnX (X = S, Se) nanocrystals via the CdO precursor," *Journal of Crystal Growth*, vol. 265, no. 1-2, pp. 250–259, 2004.

[11] H. Shen, H. Yuan, J. Z. Niu et al., "Phosphine-free synthesis of high-quality reverse type-I ZnSe/CdSe core with CdS/Cd$_x$Zn$_{1-X}$S/ZnS multishell nanocrystals and their application for detection of human hepatitis B surface antigen," *Nanotechnology*, vol. 22, no. 37, Article ID 375602, 2011.

[12] L. Qu and X. Peng, "Control of photoluminescence properties of CdSe nanocrystals in growth," *Journal of the American Chemical Society*, vol. 124, no. 9, pp. 2049–2055, 2002.

[13] W. W. Yu, L. Qu, W. Guo, and X. Peng, "Experimental determination of the extinction coefficient of CdTe, CdSe, and CdS nanocrystals," *Chemistry of Materials*, vol. 15, no. 14, pp. 2854–2860, 2003.

[14] S. R. Cordero, P. J. Carson, R. A. Estabrook, G. F. Strouse, and S. K. Buratto, "Photo-activated luminescence of CdSe quantum dot monolayers," *Journal of Physical Chemistry B*, vol. 104, no. 51, pp. 12137–12142, 2000.

[15] N. Myung, Y. Bae, and A. J. Bard, "Enhancement of the photoluminescence of CdSe nanocrystals dispersed in ChCl$_3$ by oxygen passivation of surface states," *Nano Letters*, vol. 3, no. 6, pp. 747–749, 2003.

[16] X. Zhong, R. Xie, Y. Zhang, T. Basché, and W. Knoll, "High-quality violet- To red-emitting ZnSe/CdSe core/shell nanocrystals," *Chemistry of Materials*, vol. 17, no. 16, pp. 4038–4042, 2005.

[17] E. Ying, D. Li, S. Guo, S. Dong, and J. Wang, "Synthesis and bio-imaging application of highly luminescent mercaptosuccinic acid-coated CdTe nanocrystals," *PLOS One*, vol. 3, Article ID e2222, 2008.

[18] P. Yang, M. Ando, and N. Murase, "Encapsulation of emitting CdTe QDs within silica beads to retain initial photoluminescence efficiency," *Journal of Colloid and Interface Science*, vol. 316, no. 2, pp. 420–427, 2007.

[19] S. T. Selvan, T. T. Tan, and J. Y. Ying, "Robust, non-cytotoxic, silica-coated CdSe quantum dots with efficient photoluminescence," *Advanced Materials*, vol. 17, no. 13, pp. 1620–1625, 2005.